



Horizon 2020  
Programme

**CORTEX**

*Research and Innovation Action (RIA)*

This project has received funding from the European Union's Horizon 2020 research and innovation programme under grant agreement No 754316.

Start date : 2017-09-01 Duration : 48 Months  
<http://cortex-h2020.eu>



---

**Development of advanced signal processing techniques and evaluation results**

---

Authors : Mr. Petr STULIK (UJV), Luis Torres (UPM), Cristina Montalvo (UPM), Agustín García-Berrocal (UPM), César Salazar (UPM), George Alexandridis (ICCS-NTUA), Tatiana Tabouratzis (UoP, ICCS-NTUA), Jindrich Machek (UJV Rez), Laurent Pantera (CEA), Martin Bem (UJV Rez)

CORTEX - Contract Number: 754316

Project officer: Foivos MARIAS

Document title	Development of advanced signal processing techniques and evaluation results
Author(s)	Mr. Petr STULIK, Luis Torres (UPM), Cristina Montalvo (UPM), Agustín García-Berrocal (UPM), César Salazar (UPM), George Alexandridis (ICCS-NTUA), Tatiana Tabouratzis (UoP, ICCS-NTUA), Jindrich Machek (UJV Rez), Laurent Pantera (CEA), Martin Bem (UJV Rez)
Number of pages	106
Document type	Deliverable
Work Package	WP03
Document number	D3.3
Issued by	UJV
Date of completion	2019-09-06 18:24:35
Dissemination level	Public

---

### Summary

This document describes the development of advanced signal processing techniques for analysing real plant in-core and ex-core data and also for analysing simulated neutron noise data coming from modelling. The processed data resulting from these analyses are ready to be fed as inputs to deep neural networks for parameter class prediction and to machine learning algorithms for anomaly classification and localization.

---

### Approval

Date	By
2019-09-06 18:36:47	Pr. Kollias STEFANOS (University of Lincoln)
2019-09-06 21:03:13	Pr. Christophe DEMAZIERE (Chalmers)

## Table of Contents

Index of Tables .....	3
Table of Figures .....	4
Abbreviations .....	7
1 Introduction .....	8
2 Summary of Developments .....	9
2.1 Analysis of Chalmers simulated data .....	9
2.2 Analysis of PSI simulated data .....	9
2.3 Wavelet transformations .....	10
2.4 Singular Spectrum Analysis .....	10
2.5 Plant data processing .....	10
2.6 Reconstructing data .....	11
2.7 Preliminary analysis of plant data .....	11
3 Key Developments .....	12
3.1 Analysis of Chalmers simulated data .....	12
3.1.1 Simulated data .....	12
3.1.2 Amplitude dependence on neutron energy group and frequency .....	13
3.1.3 Phase dependence on neutron energy group and frequency .....	15
3.1.4 Dependence on the location .....	17
3.1.5 Symmetry and linearity of propagation .....	22
3.1.6 Some configurations with multiple perturbations .....	24
3.1.7 Distribution of the PSD amplitude .....	28
3.1.8 Conclusions .....	32
3.2 Analysis of PSI simulated data .....	32
3.2.1 Analyzed Scenarios .....	32
3.2.2 Analysis .....	34
3.2.3 Compilation of the data and discussion .....	47
3.2.4 Conclusions .....	49
3.3 Wavelet transformations .....	51
3.3.1 Discrete Wavelet Transform .....	51
3.3.2 Conclusion .....	58
3.4 Plant data processing .....	59
3.4.1 NPP Dukovany .....	59
3.4.2 NPP Temelin .....	62
3.4.3 Conclusions .....	66
3.5 Single Spectrum Analysis .....	67
3.5.1 Principles of the SSA method .....	67
3.5.2 CABRI experiments and the acoustic noise data-processing .....	68
3.5.3 Conclusions .....	72
4 Reconstructing data .....	73
4.1 Purpose of reconstruction .....	73
4.2 Reconstruction prepositions .....	73
4.3 Reconstruction algorithm .....	73
4.4 Details of the algorithm and examples of its use .....	74
4.4.1 Definition of valid data interval .....	74
4.4.2 Ordering SPNDs according to their distances .....	76
4.4.3 Calculation of reconstruction coefficients .....	76

4.5	Reconstruction results .....	76
4.5.1	Reconstruction of PSI simulated data .....	76
4.5.2	Reconstruction of NPP Gösgen data.....	78
4.5.3	Conclusions.....	79
5	Preliminary processing of real data .....	80
5.1	Swiss 3-loop pre-KONVOI reactor in Gösgen .....	80
5.1.1	Measurement .....	80
5.1.2	Preliminary analysis of the spectral characteristics .....	81
5.2	American 4-loop and 3-loop Westinghouse reactors.....	84
5.2.1	Measurement .....	84
5.2.2	Mother Wavelet Selection.....	85
5.2.3	Joint Time Frequency Domain .....	86
5.3	German 4-loop pre-KONVOI reactor .....	87
5.3.1	Measurement .....	87
5.3.2	Joint Time Frequency Domain .....	88
5.4	Czech 4 loop VVER 1000 reactor in Temelin .....	89
5.4.1	Measurement .....	89
5.4.2	Joint Time Frequency Domain .....	90
6	Conclusions .....	92
7	References .....	93
8	Annexes .....	96
8.1	Annex A1 – JTFS spectrograms of upper L-G02-1 SPND in Goesgen EOC of U1C39 in the frequency ranges up to 100Hz .....	96
8.2	Annex A2 – JTFS spectrograms of lower fission chamber IC-N12-44 in WEC PWR3 in the frequency ranges up to 100Hz.....	97
8.3	Annex A3 – JTFS spectrograms of upper LJ02-1 SPND of German 4-loop pre-KONVOI reactor in EOC U1C30 in the frequency ranges up to 100Hz.....	98
8.4	Annex A4 – JTFS spectrograms of upper N317 SPND in the Czech 4 loop VVER 1000 Temelin of BOC U1C09 in the frequency ranges up to 150Hz.....	99
8.5	Annex A5 – Reconstruction of in-core Gösgen EOC39 results - summary .....	101
8.6	Annex A6 – Reconstruction of ex-core Gösgen EOC39 results – summary .....	102
8.7	Annex A7 – Reconstruction of in-core Gösgen BOC40 results – summary .....	103
8.8	Annex A8 – Reconstruction of ex-core Gösgen BOC40 results – summary .....	104
8.9	Annex A9 – Reconstruction of in-core Gösgen MOC40 results – summary.....	105
8.10	Annex A10 – Reconstruction of ex-core Gösgen MOC40 results – summary.....	106



## Index of Tables

Table 1: Data ranges of amplitude in fast spectrum for 0.1 Hz, 1 Hz and 10Hz respectively .....	13
Table 2: Data ranges of amplitude in thermal spectrum for 0.1 Hz, 1 Hz and 10Hz respectively .....	14
Table 3: Data ranges of phase in fast spectrum for 0.1 Hz, 1 Hz and 10Hz respectively .....	15
Table 4: Data ranges of phase in thermal spectrum for 0.1 Hz, 1 Hz and 10Hz respectively .....	16
Table 5: Data ranges for 0.1 Hz, 1 Hz and 10Hz respectively .....	16
Table 6: Data ranges with perturbation at (16,16,13) in the fast spectrum with 0.1 Hz .....	17
Table 7: Data ranges with perturbation at (1,16,13) in the fast spectrum with 0.1 Hz .....	18
Table 8: Data ranges with perturbation at (5,7,13) in the fast spectrum with 0.1 Hz .....	19
Table 9: Data ranges with perturbation at (5,7,1) in the fast spectrum with 0.1 Hz .....	20
Table 10: Data ranges with perturbation at four locations in the fast spectrum with 0.1 Hz .....	21
Table 11: Data ranges with perturbation at (5,7,13) for the three frequencies .....	21
Table 12: Sample rates for every test .....	71

## Table of Figures

Figure 1: Amplitude in Fast spectrum for 0.1 and 10 Hz respectively .....	13
Figure 2: Amplitude in thermal spectrum for 0.1 and 10 Hz respectively .....	14
Figure 3: Phase in fast spectrum for 0.1 Hz and 10Hz respectively .....	15
Figure 4: phase in thermal spectrum for 0.1 Hz, 10Hz respectively .....	16
Figure 5: Amplitude and Phase with perturbation at (16,16,13) in the fast spectrum with 0.1 Hz .....	17
Figure 6: Amplitude and Phase with perturbation at (1,16,13) in the fast spectrum with 0.1 Hz.....	18
Figure 7: Amplitude and Phase with perturbation at (5,7,13) in the fast spectrum with 0.1 Hz.....	19
Figure 8: Amplitude and Phase with perturbation at (5,7,1) in the fast spectrum with 0.1 Hz.....	20
Figure 9: Symmetry of amplitude propagation with a perturbation in the centre .....	22
Figure 10: Asymmetry of amplitude propagation with a perturbation near to edge .....	22
Figure 11: Symmetry and linearity of phase propagation with a perturbation in the centre .....	23
Figure 12: Symmetry and linearity of phase propagation with a perturbation in edge .....	23
Figure 13: Amplitude propagation and phase when perturbation is located in four central rows .....	24
Figure 14: Amplitude propagation with perturbation in planes Z=1, Z=2, Z=3, one quadrant.....	25
Figure 15: Phase distribution with perturbation in planes Z=1, Z=2, Z=3, one quadrant .....	25
Figure 16: Amplitude and phase with Perturbation in one row in the edge (1,16,:) .....	26
Figure 17: Amplitude and phase with perturbation in one row near to edge (3,16,:) .....	26
Figure 18 :Amplitude and phase with perturbation in four rows near to edge .....	27
Figure 19: PSD amplitude with a punctual perturbation in location (16,16,13) .....	28
Figure 20: PSD amplitude with a punctual perturbation in location (2,16,13) .....	29
Figure 21: PSD amplitude with a perturbation in the four center rows.....	29
Figure 22: Evolution in space of the PSD amplitude with a perturbation in the four centre rows .....	30
Figure 23: Amplitude distribution of the APSD when it is considered all the perturbations in all reactor nodes.....	31
Figure 24: Radial layout of the sensor strings and fuel elements which are vibrating .....	34
Figure 25: Signal and 4 first IMFs of scenario 1.1 .....	36
Figure 26: Hilbert Spectrum, Scenario 4.2, Incore 1 .....	36
Figure 27: Hilbert Spectrum, Scenario 4.2, Incore 3 .....	37
Figure 28: Hilbert Spectrum, Scenario 4.2, Excore 1 .....	37
Figure 29: APSDs of thermal-hydraulic scenarios, flow and temperature oscillations, left and right side respectively. Upper figures correspond to all radial positions at level 5, lower figures correspond to all levels in only one radial position (String 4) Note that Lv 1 and Lv 6 are the lowest and the uppermost level respectively. ....	39
Figure 30: The standard deviation versus the axial level in string J02 and J06. Note that Lv 1 and Lv 6 are the lowest and the uppermost level, respectively. ....	40
Figure 31: Coherence and phase fluctuation between incore sensors of the flow oscillation (left) and temperature oscillation (right) scenarios. Note that Lv 1 and Lv 6 are the lowest and the uppermost level, respectively. ....	40
Figure 32: Scenario 5.6. APSDs of the radial positions at level 5.....	41
Figure 33: Scenario 5.2. from left to right; APSDs of the radial positions at level 5, Coherences and Phases and radial distribution of out-of-phase zones. ....	42

Figure 34: Scenario 5.6. APSDs of the radial positions at level 5.....	42
Figure 35: Scenario 5.6. from left to right; Coherences and Phases at level 1 (string reference 2 and 4 respectively) and radial distribution of out-of-phase zones. ....	43
Figure 36: Scenario 5.4. from left to right; APSDs of the radial positions at level 5, Coherences and Phases and radial distribution of out-of-phase zones. ....	44
Figure 37: Scenario 5.8. from left to right; APSDs of the radial positions at level 5, Coherences and Phases and radial distribution of out-of-phase zones. ....	44
Figure 38: Scenario 4.2 and Scenario 4.4. APSDs of the radial positions at level 5 .....	45
Figure 39: From left to right; Coherences and Phases and radial distribution of phase relationships. The upper figures correspond to the Group 1 random vibrations (Scenario 4.1 and Scenario 4.2), The Lower figures correspond to the Group 2 sinusoidal vibrations (Scenario 4.3 and Scenario 4.4).....	46
Figure 40: Coherences and Phases in a same string, same axial position between incore sensors of the Scenario 4.2 and Scenario 4.4. Note that Lv 1 and Lv 6 are the lowest and the uppermost level respectively. ....	46
Figure 41: The phase relationships between Lv 1 and Lv 6 in-core sensors (lower and upper sensors, respectively) of a same string in a KWU-PWR.....	47
Figure 42: APSDs of the first series of tables .....	48
Figure 43: Coherence and phase relationships of the first series of tables .....	48
Figure 44: Optimal mother wavelet selection based on the cross-correlation criterion.....	52
Figure 45: Optimal mother wavelet selection based on the energy-to-entropy criterion.....	53
Figure 46: Energy distribution of Internal Detectors (Energy-to-entropy criterion).....	54
Figure 47: Energy distribution of Internal Detectors (Cross-correlation criterion) .....	55
Figure 48: Energy distribution of External Detectors (Energy-to-entropy criterion) .....	56
Figure 49: Energy distribution of External Detectors (Cross-correlation criterion) .....	57
Figure 50: Scaleogram of wavelet-decomposed signal .....	58
Figure 51: NPP Dukovany Unit #4 MCP supply current fluctuations .....	60
Figure 52: NPP Dukovany Unit #4 long-term consequences of the fifth cycle.....	60
Figure 53: NPP Dukovany Unit pressure vessel beat frequencies at MCP 1st and 2nd revolution harmonics (24Hz, 48Hz) in U3C18 cycle of the 3 <sup>th</sup> unit.....	61
Figure 54: Absolute displacement sensor OA3V beat signal at MCP 1st and 2nd revolution harmonics (24Hz, 48Hz) in U430 of the 4 <sup>th</sup> unit NPP Dukovany.....	61
Figure 55: Beat effects of the 1st loop hot leg pressure fluctuations (NPP Temelin, U2C09).....	63
Figure 56: Unit #01 reactor head accelerometers and in-core SPND spectrograms and PSD spectra of VV6 (U1C07) and TVSAT (U1C09) .....	64
Figure 57: Beat vibration effects at MCP harmonic frequencies generated by input pressure fluctuations (NPP Temelin, U2C03).....	65
Figure 58: Core power transient and 3He pressure (example of measurements) .....	69
Figure 59: CABRI core and Transient Rods system .....	69
Figure 60: Location of the two piezoelectric sensors in the test device .....	70
Figure 61: Overview of the two microphones (M1 and M2) signals for every test. ....	70
Figure 62: Strategy to choose the window size for the spectral subtraction calculation for different values of the $\alpha$ parameter and the SNR .....	72
Figure 63: Example of SPND failure and reconstruction of its data .....	74
Figure 64: Example of SPND signal level change and corresponding invalid data reconstruction .....	75

### *D3.3 Development of advanced signal processing techniques and evaluation results*

Figure 65: Example of SPND one side deviations and corresponding invalid data reconstruction .....	75
Figure 66: Simulated O5Lv3 random signal and its reconstruction .....	76
Figure 67: Simulated O5Lv3 sinusoidal signal and its reconstruction.....	77
Figure 68: Simulated O5Lv1, O5Lv3 signals in 2019-05-Dataset7-C03-FA1-SIN-1.2Hz-1mm-1 .....	77
Figure 69: Reconstruction on L-J06-2 signal - beginning of valid data part.....	78
Figure 70: Reconstruction on L-J06-2 signal - end of valid data part .....	78
Figure 71: Radial distribution of excore and incore detectors respectively, note that the figure of incore is rotated 180°. .....	80
Figure 72: Axial Positions of Used detectors. ....	81
Figure 73: APSDs of 8 detectors at the level 1 (the uppermost). The right figure shows the APSDs up to 10 Hz. ....	81
Figure 74: Coherences and phases of Incore detectors at level 1 with string J06 as reference. In the left figure we can see the out-of-phase zones. ....	82
Figure 75: Coherence and phase between in-core sensors. Real case of Göesgen and PSI simulation of mixed scenario, respectively .....	82
Figure 76 JTFS spectrogram of upper L-G02-1 SPND in Goesgen EOC of U1C39 in the frequency range 0 – 100Hz .....	83
Figure 77 The radial distribution of the in-core and ex-core neutron detectors of 3-loop Westinghouse reactor .....	84
Figure 78 The radial distribution of the in-core and ex-core neutron detectors of 3-loop Westinghouse reactor .....	85
Figure 79 JTFS spectrogram of lower fission chamber IC-N12-44 in WEC PWR3 in the frequency range 0 – 100Hz .....	86
Figure 80 Radial and axial detector positions in the German 4-loop pre-KONVOI reactor.....	87
Figure 81 JTFS spectrogram of upper LJ02-1 SPND of German 4-loop pre-KONVOI reactor.....	88
Figure 82 Radial and axial detector positions in the Czech 4 loop VVER 1000 in Temelin.....	89
Figure 83 JTFS spectrograms of upper N317 SPND in the Czech 4 loop VVER 1000 Temelin of BOC U1C09 in the frequency range 0 – 150Hz.....	90
Figure 84 Multilevel analysis process .....	91

## Abbreviations

AMS	Analysis and Measurement Services Corporation
APSD	Auto Power Spectral Density
BOC	Beginning of Cycle
CPSD	Cross Power Spectral Densities
DMTS	Distributed Measuring Test System
EOC	End of Cycle
FA	Fuel Assembly
FFT	Fast Fourier Transform
GRS	Gesellschaft für Anlagen- und Reaktorsicherheit (GRS) GmbH
IRI	Incompatible Rod Insertion
ISTec	Institut fuer Sicherheitstechnologie (Institute of Safety Technology)
IT	Information Technology
JTFD	Join Time Frequency Domain
JTFS	Join Time Frequency Spectrogram
KKG	Kernkraftwerk Gösgen (NPP Gösgen)
KWU	Kraftwerk Union AG
MOC	Middle of Cycle
MCP	Main Circulation Pump
NAPSD	Normalized Auto Power Spectral Density
NPP	Nuclear Power Plant
PEL	Preussen Elektra
PSI	Paul Scherrer Institut
PWR	Pressurized Water Reactor
RCP	Reactor Coolant Pump
RCS	Reactor Coolant System
RMS	Root Mean Square
RPV	Reactor Pressure Vessel
RVDT	Reactor Vibration Diagnostic Terminal
RVMS	Reactor Vibration Monitoring System
STFT	Short Time Fourier Transform
SPND	Self-Powered Neutron Detector
SPS	Samples Per Second
TC	Thermocouple
WP	Work package
VVER/ WWER	Vodo-Vodyanoi Energetichesky Reaktor / Water-Water Energetic Reactor

## Summary

This document describes the development of advanced signal processing techniques for analysing real plant in-core and ex-core data and also for analysing simulated neutron noise data coming from modelling. The processed data resulting from these analyses are ready to be fed as inputs to deep neural networks for parameter class prediction and to machine learning algorithms for anomaly classification and localization.

# 1 Introduction

The Horizon 2020 EU project CORTEX involves the development of monitoring techniques (and their experimental validation) using the so-called neutron noise (fluctuations in neutron flux recorded by in-core and ex-core neutron instrumentation). Such techniques allow detecting anomalies in nuclear reactor cores, such as abnormal vibrations of fuel and core internals, flow blockage, coolant inlet perturbations, etc. Noise-based core monitoring is a non-intrusive technique. Signal analysis methods can be utilized to detect anomalous patterns in the recorded neutron noise. Results of consequent advanced signal analysis are used in core diagnostics in order to backtrack the nature and spatial distribution of the anomaly. This approach has nevertheless its own limitations since only a few types of anomalies can be identified. Therefore, the CORTEX project relies on another approach based on the inversion of the reactor transfer function. It must be noted that the inversion of the reactor function is only possible if the induced neutron noise could be measured at every position inside the reactor core ([ 1 ] - [ 2 ]). Since this is not possible, another solution strategy is proposed in CORTEX. It relies on the combination of advanced signal processing techniques and artificial / computational intelligence methodologies ([ 3 ] - [ 15 ]).

In this Deliverable, the following objective was achieved:

“To develop and use advanced signal processing for extracting the relevant and meaningful fluctuations from measured signals. Emphasis is put on how to deal with non-stationary and intermittent signals.”

The aim of advanced signal processing techniques in this Deliverable is to extract features including the respective energy spectra and the frequency content in different bands, resolutions and visualizations, to detect abnormal fluctuations and perturbations in the simulated data, remove noise and intermittences. These techniques include FFT, multiresolution wavelet and Hilbert-Huang transform.

## 2 Summary of Developments

In this chapter a short overview of the performed advanced signal developments is given. More details can be found in Chapter 3.

### 2.1 Analysis of Chalmers simulated data

This development demonstrates the processing and analysis of CORE SIM reactor physics code results from Chalmers University describing neutron flux perturbations in the frequency domain induced by prescribed perturbations.

These perturbations are generated for a so-called absorber of variable strength, which represents the macroscopic cross-sections changes in the reactor at a given position.

The performed analysis includes three basic cases, i.e., the amplitude and phase distribution of the perturbations in the reactor, the dependence on frequency, location and energy group, as well as the symmetry of the data.

The aim when modelling the effect of perturbations onto the neutron flux is to convert physical perturbations (vibration of internal parts and fuel, fluid-structure interactions, etc.) into input data directly usable by core simulators via macroscopic cross-sections.

The extent of individual basic cases of perturbation analysis is as follows:

- amplitude and phase dependences on neutron energy group and frequency
- dependence on the location
- symmetry and linearity of propagation
- selected configurations with multiple perturbations (4 center rows, 3 vertical planes of one core quadrant, 2 horizontal rows at the core edges, 4 vertical lines)

The findings of these analyses create the necessary assumptions for the investigation of more complicated cases being closer to real reactor conditions.

### 2.2 Analysis of PSI simulated data

This development presents results of spectral analysis of ex-core and in-core neutron detector signals in various scenarios modelled by PSI using the transient nodal code S3K in the time domain. Altogether, three scenario categories are investigated, i.e., scenarios with thermohydraulic oscillations, with mechanical vibrations and with mixed oscillations.

More specifically, the scenarios are defined as:

- two scenarios with thermohydraulic oscillations characterized by synchronized inlet coolant fluctuation of flow and temperature in all four loops
- four scenarios with synchronized 1.5 Hz vibrations of the central 5 x 5 fuel assemblies cluster in Y and XY direction combined, respectively, and displacement amplitudes of 0.5 mm / 1 mm respectively
- two scenarios with mixed oscillations given by a combination of synchronized inlet coolant fluctuations of temperature and flow in all four loops.

The in-core and ex-core sensors from the above mentioned scenarios were processed by the following spectral methods

- Hilbert Huang Transform in order to observe its potential contribution to the FFT analysis
- APSD calculation of all available axial levels and radial positions
- Coherence and phase analysis between selected pairs.

The analyses performed are focused mainly on understanding simulated neutron noise and its interconnection with spectral behaviour of real plant data from KWU reactors. Numerous results are then grouped in Tables, consequently allowing to draw conclusions and fulfilling the overall goal to elaborate a map of features for effectively recognizing patterns in signals. This map can also be used by machine learning techniques.



## **2.3 Wavelet transformations**

The wavelet transform can only be applied to signals in the time domain; therefore, it has been used for the respective simulated signals provided by PSI. Prior to performing the transformation, a few pre-processing steps are necessary. Firstly, any existing trend in the signals needs to be removed. This is achieved by linear regression fitting to the time data and removing the linear component from the signal. Subsequently, all signals have been resampled in order to have the same length. Additionally, all simulated signals were stationary, therefore the analysis concerning the optimal time window and the choice between non-overlapping or sliding time windows was not applicable in this case. Finally, the optimal mother wavelet function has been identified, along with its respective hyperparameters. The latter is especially important, because different mother wavelets result in different decompositions.

The optimal mother wavelet is determined using two criteria; one information-theoretical (energy-to-entropy) and one statistical (cross-correlation). The latter aims at measuring the similarity between the mother wavelet and the signal. By maximizing this measure, the mother wavelet is chosen to be the one whose shape best "matches" the data. The energy-to-entropy criterion maximizes the ratio of the decomposed signals' energy to its entropy.

After identifying the best mother wavelet through either of the two criteria, the wavelet decomposition can be carried out. Two forms of analyses have been performed, the first one involves the measurement of the energy of the transformed signal at each level of decomposition, while the second one aims at extracting the signals' "scaleograms" (the equivalent of the spectrogram for the wavelet transform). Scaleograms are essentially 2-dimensional heatmaps that depict the value of each coefficient per time and per decomposition level. In conclusion, both aforementioned analyses extract features from the signals that can be then used by Machine Learning methodologies.

## **2.4 Singular Spectrum Analysis**

In the context of processing Acoustic Emission Signals acquired in the experimental campaigns at the CABRI facility (French nuclear research reactor) [ 24 ] we have first used classical methodologies ([ 25 ] – [ 26 ]) to pre-process the data. These methods proved to be very robust on noisy data, but in order to extract more information from the data, we introduced and used another methodology.

The Singular Spectrum Analysis (SSA) method has received much attention since the early nineties. Unlike most methods for time series analysis, SSA needs no statistical assumption on signal or noise. By using a decomposition of the signal into the sum of a small number of independent and interpretable components, SSA allows to perform various tasks such as extraction of specific components from a complex signal (noise, trend, seasonality ...), detection of structural changes and missing values imputation. We have explored the ability of the SSA to analyse and denoise AE signals [ 27 ].

We have used this approach on neutron noise data. Firstly, we applied the method on simulated data. Then we applied it on actual power plant data in order to highlight how this method can improve the performance of classical approaches.

## **2.5 Plant data processing**

The intention of this part was to show the means of the joint time frequency method in solving dynamic phenomena in core where it is necessary to monitor the development of spectral characteristics over time. This is shown on examples of real noise datasets from two power plants - NPP Dukovany and NPP Temelín. Historical operational experience of NPP Dukovany was demonstrated with its important operational consequences. In the described case vibration beats of pressure vessel and fuel assemblies were associated to pressure and flow fluctuations generated by the main circulation pumps (MCP) with slightly differed revolutions. Beat vibration effects of NPP Temelin and Dukovany were shown to be a common feature of dynamic pressure vessel and core



behaviour. Also, MCP harmonic frequencies were shown common to both plants with a beat character representing a negligible component in overall reactor and core signal behaviour.

Joint time frequency analysis JTFA tools were used for this purpose when Short Time Fourier Transform STFT divides the dataset into time intervals and calculates the power spectral density PSD at each time interval separately. The type of sliding spectral windows, frequency and time resolutions are the parameters of these calculations. The result is then displayed in 2D or 3D spectrograms using a scale in decibels for the PSD value.

Investigating these phenomena, joint time frequency analysis was demonstrated to be a helpful tool for better distinguishing between technological irregularities, anomalies or failures. It provides a quick summary for classifying and localizing possible perturbations before using other advanced signal processing methods.

## **2.6 Reconstructing data**

At the beginning of the project it was known, that reconstruction of in-core neutron flux slow (1-minute sampling period) measurement is possible using linear combination of physically close correlated measurements. During the project it was proved both on experimental Konvoi and 4 loops data and on PSI simulated data, that this methodology (see chapter 4) is applicable to relatively fast neutron noise measurements (with sampling frequency of the order of milliseconds) and not only to in-core measurements, but also to ex-core measurements and that it allows the user to distinguish between correct and incorrect (bad) measurements. Good example of this fact is the Göesgen EOC39 in-core signal L-J06-2, which at the beginning and at the end of measurement interval has an excessive error. These incorrect parts of measurements can be successfully replaced by linear combination of the remaining signals of the string L-J06 (see chapter 4.5.2).

## **2.7 Preliminary analysis of plant data**

In this development the preliminary application of the developed methods on real plant data were investigated. For the validation of these analysing tools, neutron flux plant data were provided by several contributors (KKG & ISTec, PEL & GRS, MTA EK, UJV, AMS) for altogether five different PWR reactor types (3 and 4-loop pre-KONVOI, VVER 440 and 1000, 3 and 4-loop WEC). These data mainly consist of in-core and ex-core neutron signals, whilst including any other type of signals could give some hints on the transport of perturbations.

In the case of some selected reactors (3 and 4-loop pre-KONVOI, VVER 1000, 3-loop WEC), the main core and instrumentation properties were first analysed.

Using the developed tools, which are described in the following chapter 3, the properties of the supplied data in the time, frequency and joint time frequency domains were examined, in order to check if traces of perturbations can be found in these time, frequency and joint time frequency domains.

It turns out that to find a match between simulated and actual waveforms, it will be necessary to select not only the optimal similarity criterion, but also an appropriate way of selecting from a large number of real data from several plants with different operating parameters.

## 3 Key Developments

This chapter is devoted to more detailed description of key developments done in CORTEX WP3 Task 3.2.

### 3.1 Analysis of Chalmers simulated data

This part firstly describes a series of observations made about the data generated with the reactor physics codes CORE SIM (Chalmers University) and SIMULATE-3K (PSI). These early observations aim at analyzing and extracting some conclusions from a typical and well-defined perturbations: an absorber of variable strength. These early observations focus on briefly describing the amplitude and phase distribution of the perturbations throughout the reactor, the dependence on frequency, location and energy group, as well as describing the symmetry of the data. Secondly, it describes some configurations of perturbations with some similar phenomenological aspects of the neutron noise observed in KWU reactors.

The case that concerns us corresponds to a typical and well-defined perturbations: **absorber of variable strength** in the frequency domain.

#### 3.1.1 Simulated data

##### 3.1.1.1 Introduction

The modelling of the effect of perturbations onto the neutron flux often requires the use of models aiming at converting physical perturbations (such as vibration of components, perturbations of physical processes, etc.) into input data directly usable by core simulators. This data consists of macroscopic cross-sections, together with some geometrical description of the reactor core. These models provide some physical understanding of the driving physical perturbation and of its effect onto cross-sections.

##### 3.1.1.2 Format and configuration

In the scenario of an absorber of variable strength, the neutron noise induced by a point neutron source in a typical Pressurized Water Reactor (PWR) is analyzed. The noise source is defined as the perturbation of the thermal macroscopic absorption cross-section. Three sets of calculations are performed, each one for all possible positions of the noise source. In each set a different frequency is used; the used frequencies are 0.1 Hz, 1 Hz and 10 Hz.

For these calculations a spatial mesh (i,j,k) with dimensions 32x32x26 was utilized. A node size of  $\Delta x=10.75$  cm,  $\Delta y=10.75$  cm and  $\Delta z=15.24$  cm was used.

The results are presented in files type .mat, since CORE SIM saves the results in such a format; these files are called RESULTS\_”i”\_”j”\_”k”.mat where i,j,k stand for the location of the noise source. Each file contains the arrays dFLX1 and dFLX2. The array dFLX1 includes the distribution of the induced neutron noise in the fast neutron group and the array dFLX2 contains the distribution of the induced neutron noise in the thermal neutron group. Since the calculations are performed in the frequency domain, both arrays contain complex numbers.

The output files are accessible in the central repository in the path:

/home/Chalmers/WP3/T3.1.1/AbsorberOfVariableStrength/0.1Hz or 1Hz or 10Hz/. Each of the three directories contains 19552 files.

The details of the output variables, their meaning and the units used for those can be found in the CORE SIM user’s manual (Demazière, 2011b), which is accessible on the central repository at:

/home/Chalmers/WP3/T3.1.1/2011-Demaziere-CTH-NT-243.pdf

The amount of the data and its distribution in space made us consider the option of looking for a software more efficient and faster than Matlab for 3D visualizations. For these reasons ParaView was found more adequate to use to prepare the visualizations with the objective of making the analysis more efficient. The rationale behind was related to ParaView possibilities and options for data representation and visualization, besides being a tool for data analysis.

### 3.1.2 Amplitude dependence on neutron energy group and frequency

The following images in this section represent the reactor with a cut to a quarter; they show how the perturbation amplitude throughout the reactor changes when the perturbation is located in the node (16,16,13) in both groups of energy and frequencies 0.1 and 10 Hz. The scale of the colorbar is logarithmic.

#### 3.1.2.1 Fast group

As seen in Figure 1 the maximum amplitude is around 2.5 and it does not change substantially between 0.1 Hz and 10 Hz (see Table 1). It is important to note the rapid attenuation of the amplitude.

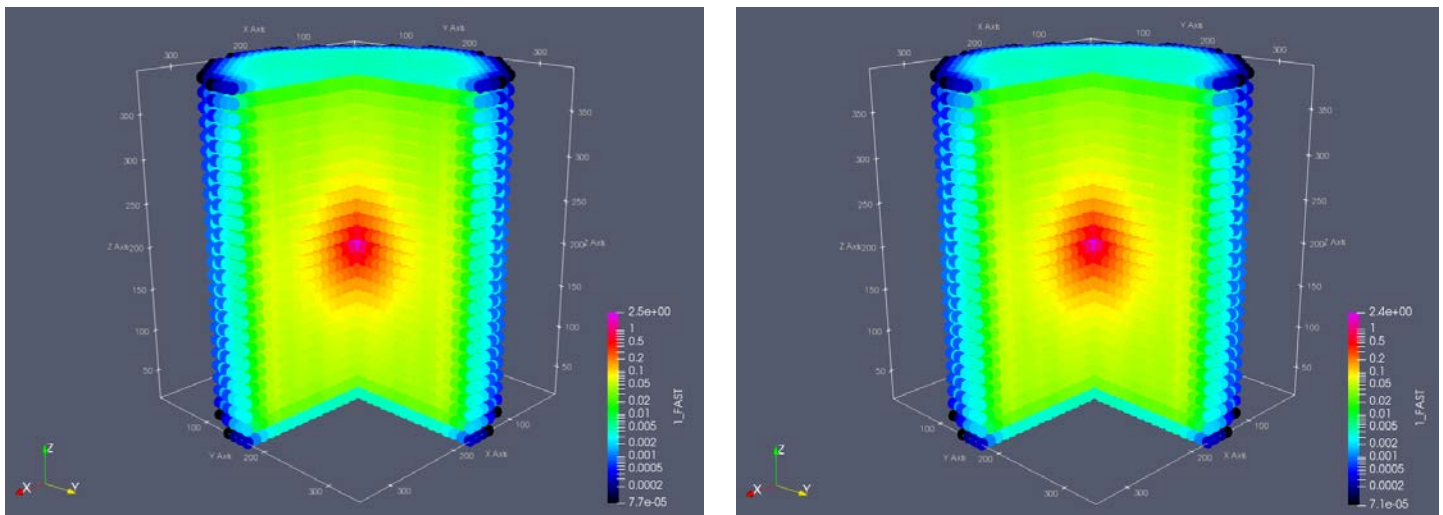


**Figure 1: Amplitude in Fast spectrum for 0.1 and 10 Hz respectively**

As we see in Table 1 the order of the amplitude does not change with different frequencies; in fact, the values are very similar.

	Data Ranges		
Magnitude	0.1 Hz	1 Hz	10 Hz
Amplitude Fast S.	[7.65E-5, 2.45]	[7.53E-5, 2.45]	[7.29E-5, 2.44]

**Table 1: Data ranges of amplitude in fast spectrum for 0.1 Hz, 1 Hz and 10Hz respectively**

#### 3.1.2.2 Thermal group

In this case, Figure 2 shows that the maximum amplitude is around 1.1 and, again, does not change substantially between 0.1 Hz and 10 Hz. It is important to note once more the rapid attenuation of the amplitude; in this case the attenuation is greater than in the fast spectrum.

### D3.3 Development of advanced signal processing techniques and evaluation results

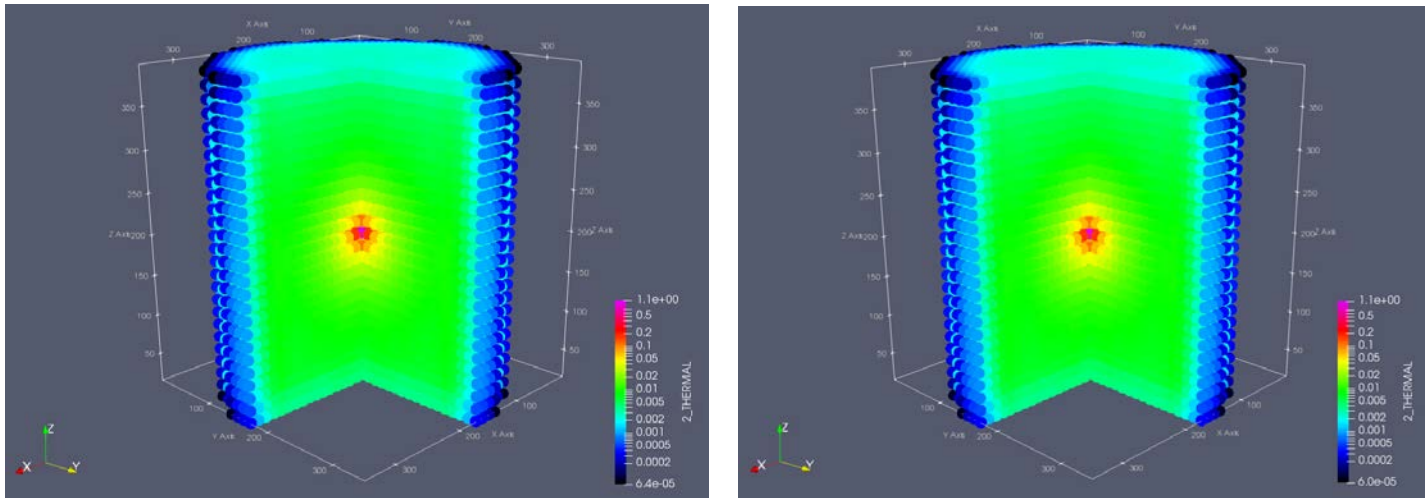


**Figure 2: Amplitude in thermal spectrum for 0.1 and 10 Hz respectively**

As we see in Table 2 the order of the amplitude does not change with different frequencies; in fact, the values are very similar.

	Data Ranges		
Magnitude	0.1 Hz	1 Hz	10 Hz
Amplitude Thermal S.	[6.44E-5, 1.12]	[6.34E-5, 1.12097]	[6.16E-5, 1.12]

**Table 2: Data ranges of amplitude in thermal spectrum for 0.1 Hz, 1 Hz and 10Hz respectively**

### 3.1.3 Phase dependence on neutron energy group and frequency

The following images in this section represent the reactor with a cut to a quarter and show the value of the phase throughout the reactor when the perturbation is located in the node (16,16,13) in both groups of energy and frequencies 0.1 and 10 Hz. In the Figures where phase is represented, the colorbar scale is linear. This central node was selected for being a representative case so as to observe symmetry and linearity without the influence of boundary conditions.

#### 3.1.3.1 Fast group

As seen in Figure 3 the phase value ranges are around [170-180] degrees for 0.1 Hz and [160-180] degrees for 10 Hz. It is important to note that the phase scale is linear for both frequencies.

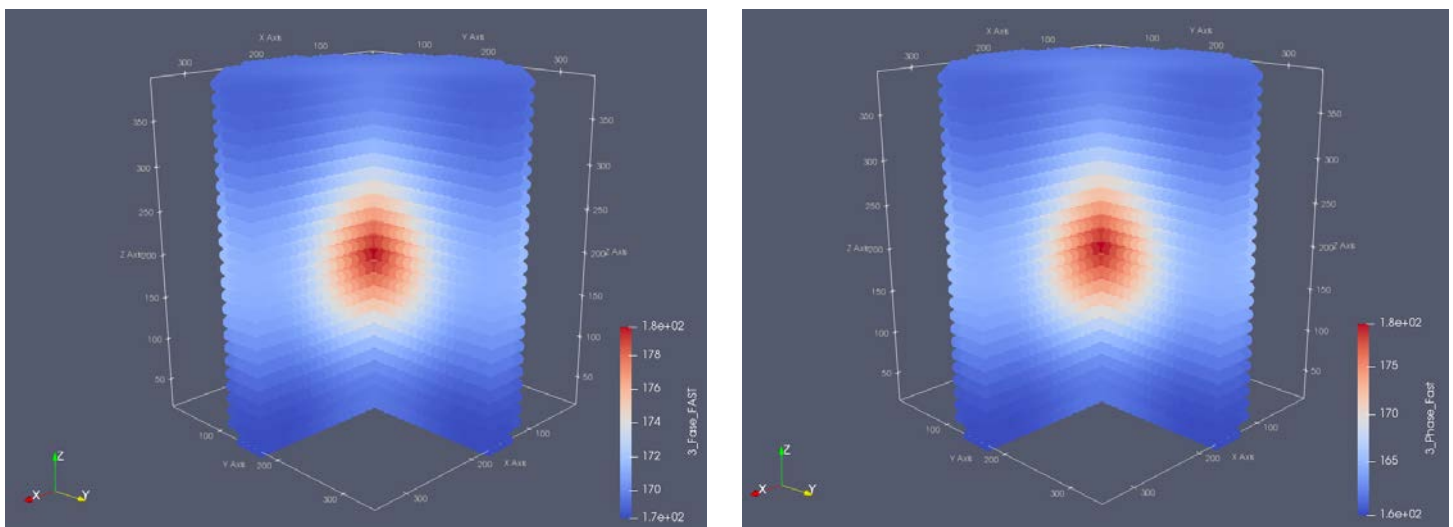


**Figure 3: Phase in fast spectrum for 0.1 Hz and 10Hz respectively**

As shown in Table 3, the phase range is 11.38, 3.15, 20.10 degrees for 0.1 Hz, 1 Hz and 10Hz respectively. The maximum difference of the phase occurs at 10 Hz frequency.

	Data Ranges		
Magnitude	0.1 Hz	1 Hz	10 Hz
Phase Fast S.	[168.3, 179.7]	[176.7, 179.9]	[159.4, 179.5]

**Table 3: Data ranges of phase in fast spectrum for 0.1 Hz, 1 Hz and 10Hz respectively**



### 3.1.3.2 Thermal group

As shown in Figure 4, the phase value ranges are around [170-180] degrees for 0.1 Hz and [160-180] degrees for 10 Hz. There is a similarity to the case of fast spectrum and the phase scale is also linear in both frequencies.

As can be observed in Figures 4 and 5, this case is very similar to the case of fast spectrum and the linear phase scale is shown for both frequencies.

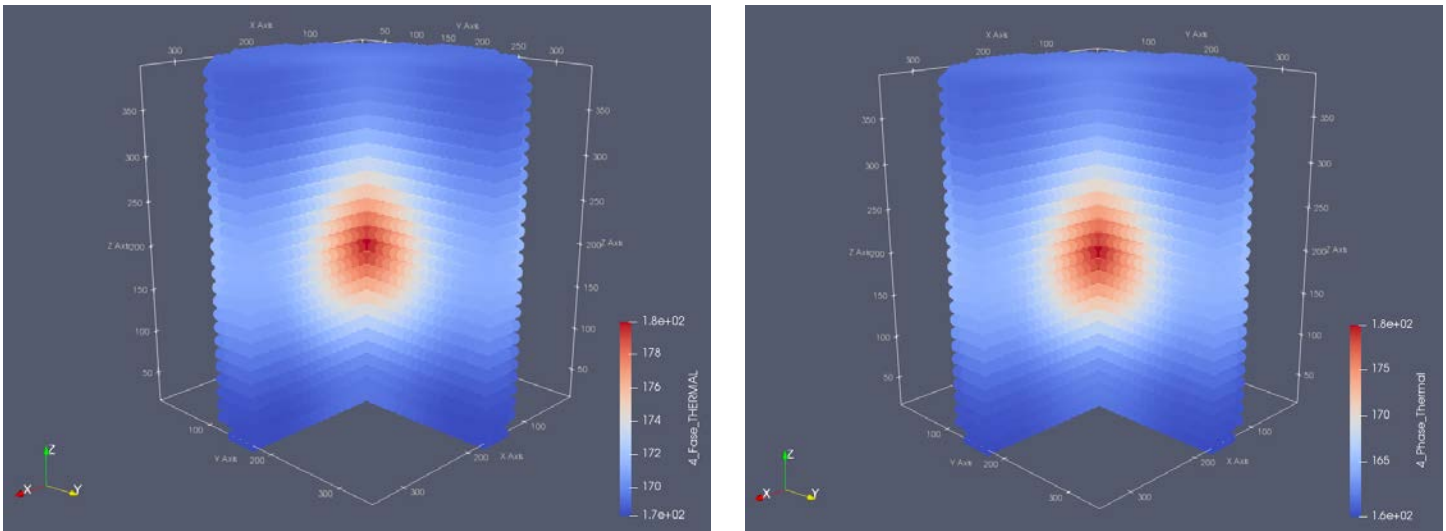


**Figure 4: phase in thermal spectrum for 0.1 Hz, 10Hz respectively**

As shown in the Table 4, the phase range is 11.59, 3.23, 20.68 degrees for 0.1 Hz, 1 Hz and 10Hz respectively. The maximum difference of the phase occurs at 10 Hz frequency.

	Data Ranges		
Magnitude	0.1 Hz	1 Hz	10 Hz
Phase Thermal S.	[168.3, 179.9]	[176.7, 179.9]	[159.1, 179.7]

**Table 4: Data ranges of phase in thermal spectrum for 0.1 Hz, 1 Hz and 10Hz respectively**

Table 5 compiles all the data ranges for the case described in sections 6 and 7, for a point-like perturbation located in the node (16, 16, 13). Based on this, we can conclude:

- The amplitude in the fast spectrum is more than two times that in the thermal spectrum.
- There is no appreciable change in the amplitude for different frequencies.
- Otherwise, the phase variation are appreciable for each of the different frequencies.

	Data Ranges		
Magnitude	0.1 Hz	1 Hz	10 Hz
Amplitude Fast S.	[7.65E-5, 2.45]	[7.53E-5, 2.45]	[7.29E-5, 2.45]
Amplitude Thermal S.	[6.44E-5, 1.12]	[6.34E-5, 1.12]	[6.16E-5, 1.12]
Phase Fast S.	[168.31, 179.69]	[176.76, 179.91]	[159.36, 179.47]
Phase Thermal S.	[168.31, 179.90]	[176.73, 179.97]	[159.064, 179.75]

**Table 5: Data ranges for 0.1 Hz, 1 Hz and 10Hz respectively**

### 3.1.4 Dependence on the location

This section analyses the amplitude and phase dependence on the perturbation location. To this aim four perturbation locations were selected in the following nodes; (16,16,13) (1,16,13) (5,7,13) (5,7,1). The reactor is represented with vertical and horizontal cross sections at central height. In the following three subsections, the two upper figures correspond to amplitude, whilst the one below corresponds to phase. The energy group represented is the fast one at the 0.1 Hz frequency in the three subsections.

#### 3.1.4.1 Location (16,16,13)

This case is part of the case presented in section 3.1.2; nevertheless it is presented again because it is interesting to compare it with the other configurations (1,16,13) (5,7,13) (5,7,1).

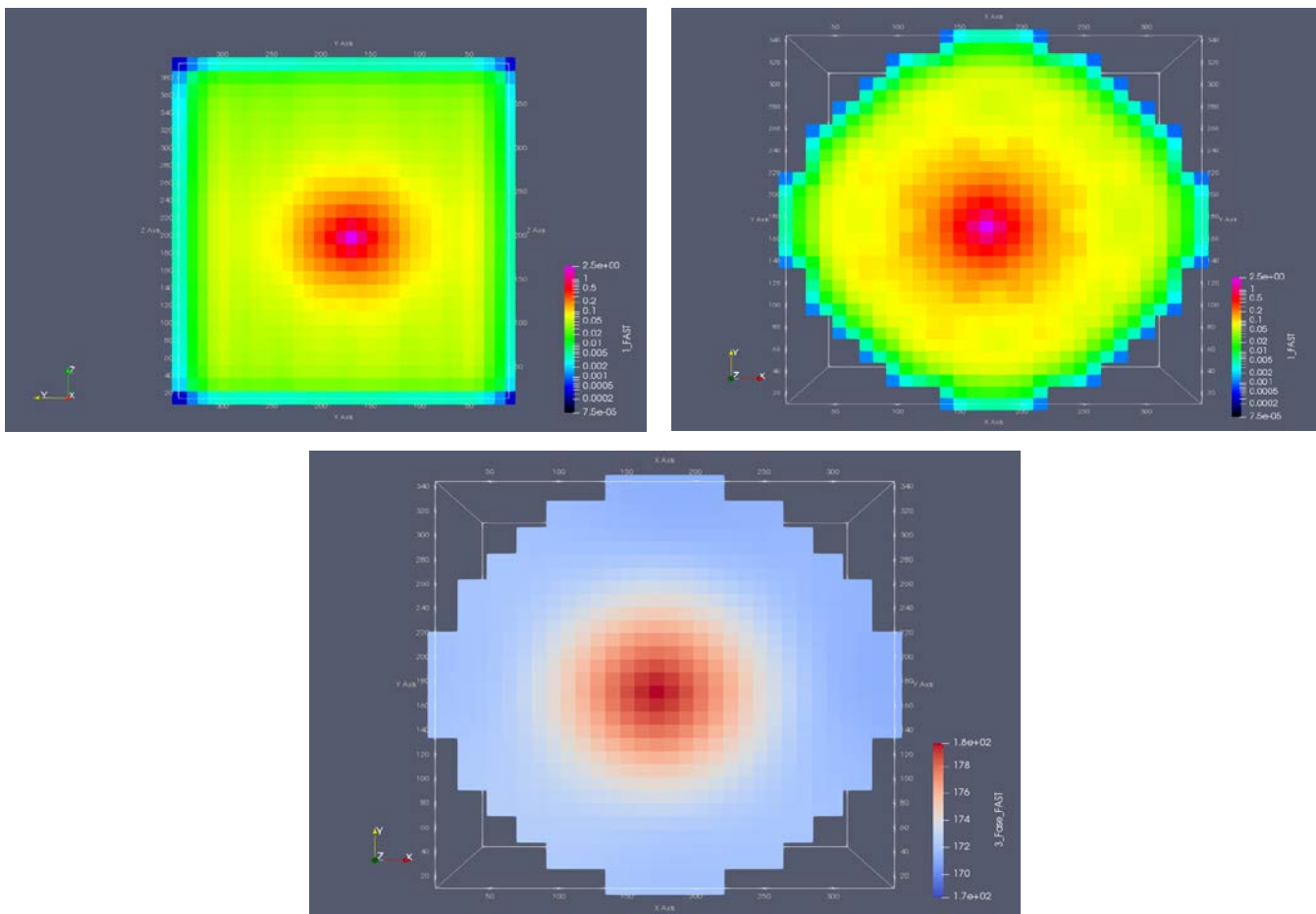


Figure 5: Amplitude (top) and Phase (bottom) with perturbation at (16,16,13) in the fast spectrum with 0.1 Hz

	Data Ranges
Magnitude	0.1 Hz
Amplitude Fast S.	[7.50E-5, 2.45]
Amplitude Thermal S.	[6.31E-5, 1.12]
Phase Fast S.	[168.31, 179.68]
Phase Thermal S.	[168.31, 179.89]

Table 6: Data ranges with perturbation at (16,16,13) in the fast spectrum with 0.1 Hz

### 3.1.4.2 Location in edge (1,16,13)

In the following cases with the perturbation at (1,16,13) (5,7,13) (5,7,1), it is important to point out that the highest observed amplitude does not coincide with the current location of the perturbation. This fact occurs in those cases where the perturbations are near the edge of the reactor.

In this case, the amplitude of the induced neutron noise is significantly asymmetrical as compared to the perturbation node (Figure 6). In Table 7 we can observe that the thermal amplitude is one order greater than the fast one.

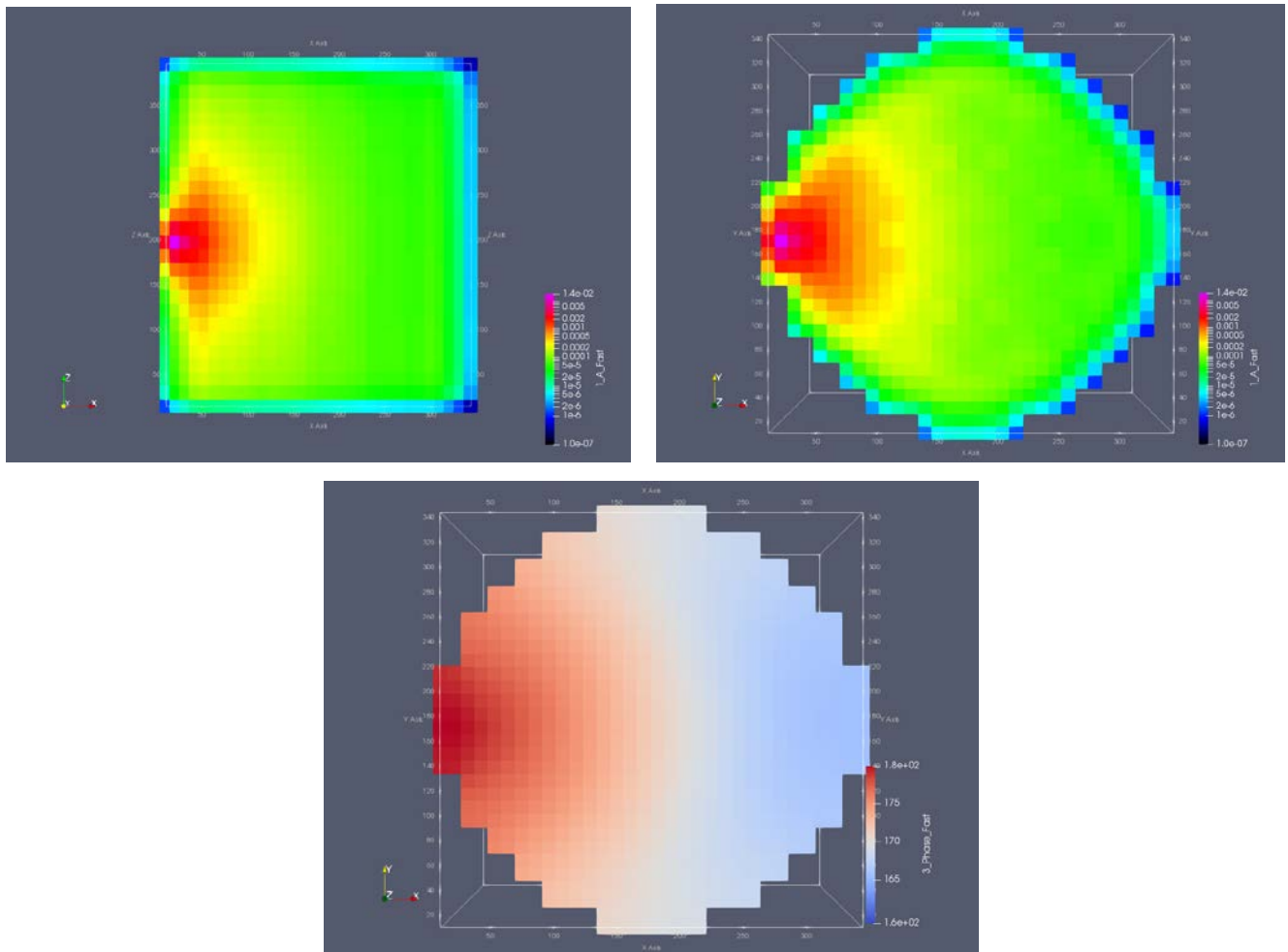


Figure 6: Amplitude (top) and Phase (bottom) with perturbation at (1,16,13) in the fast spectrum with 0.1 Hz

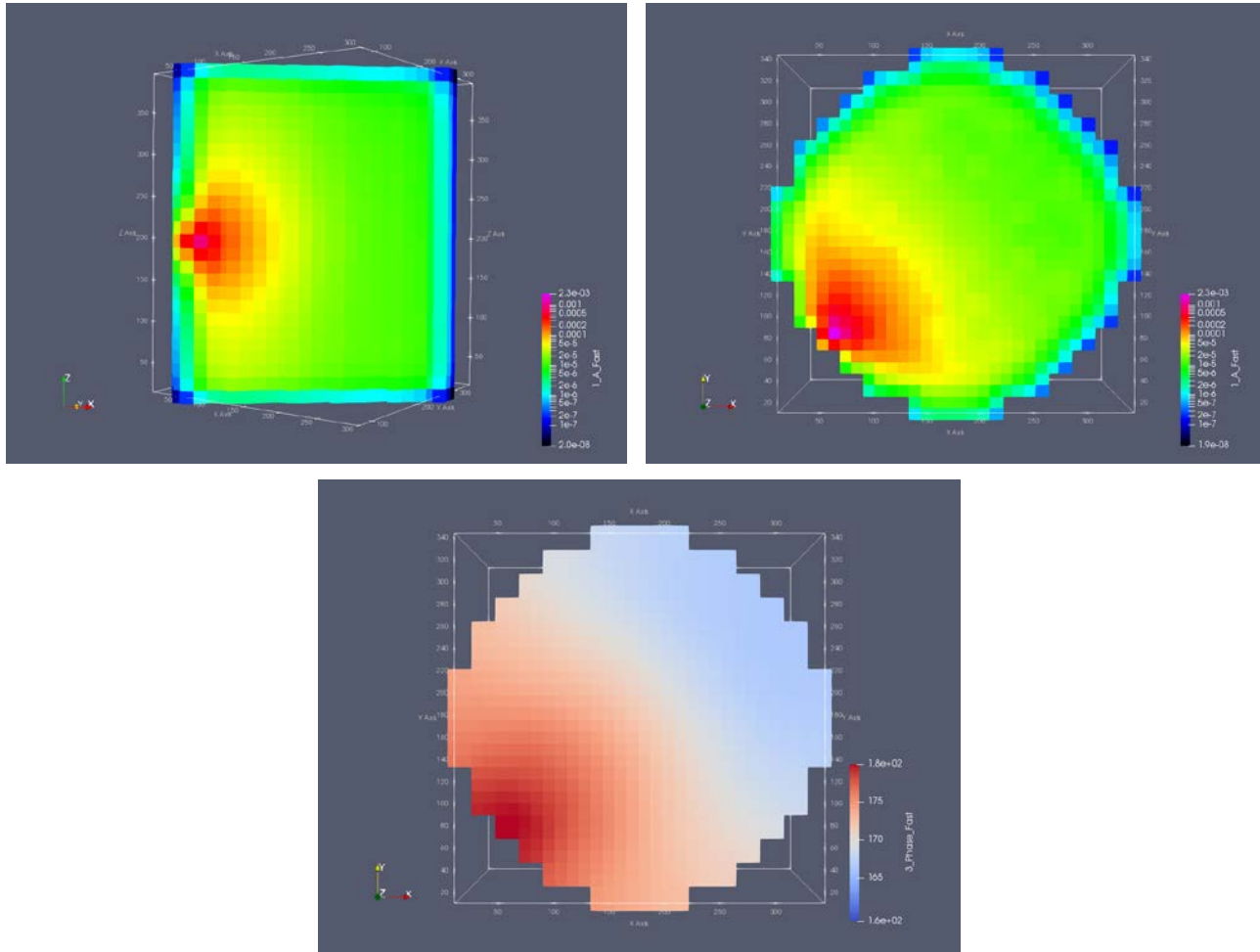
	Data Ranges
Magnitude	0.1 Hz
Amplitude Fast S.	[1.011E-7, 0.013]
Amplitude Thermal S.	[8.526E-8, 0.212]
Phase Fast S.	[164.63, 179.88]
Phase Thermal S.	[164.63, 179.99]

Table 7: Data ranges with perturbation at (1,16,13) in the fast spectrum with 0.1 Hz



### 3.1.4.3 Location in edge (5,7,13)

When the perturbation is located in (5,7,13), the results show the same trend, but to a greater extent: as shown in Table 8, the amplitude in the thermal spectrum is greater than that in the fast one and, furthermore, the thermal amplitude is two orders greater than the fast one.



**Figure 7: Amplitude and Phase with perturbation at (5,7,13) in the fast spectrum with 0.1 Hz**

When the perturbation is located in this particular node, the thermal amplitude is two orders of magnitude higher than the fast one. In absolute terms, the amplitude of both groups is lower than in the previous case where the perturbation was in the centre of the core. Nevertheless, in the cases where perturbations are at the edge of the core, the thermal amplitude is higher than the fast one; this is shown in Table 6 and Table 8.

	Data Ranges
Magnitude	0.1 Hz
Amplitude Fast S.	[1.927E-8, 0.0023]
Amplitude Thermal S.	[1.657E-8, 0.325]
Phase Fast S.	[164.11, 179.88]
Phase Thermal S.	[164.12, 179.99]

**Table 8: Data ranges with perturbation at (5,7,13) in the fast spectrum with 0.1 Hz**

#### 3.1.4.4 Location in bottom (5,7,1)

When the perturbation is just in the bottom ( $Z=1$ ), the amplitude takes relative values below  $10^{-2}$  and  $10^{-5}$  in the thermal and fast spectrum respectively, as can be seen in Figure 8 and in Table 9.

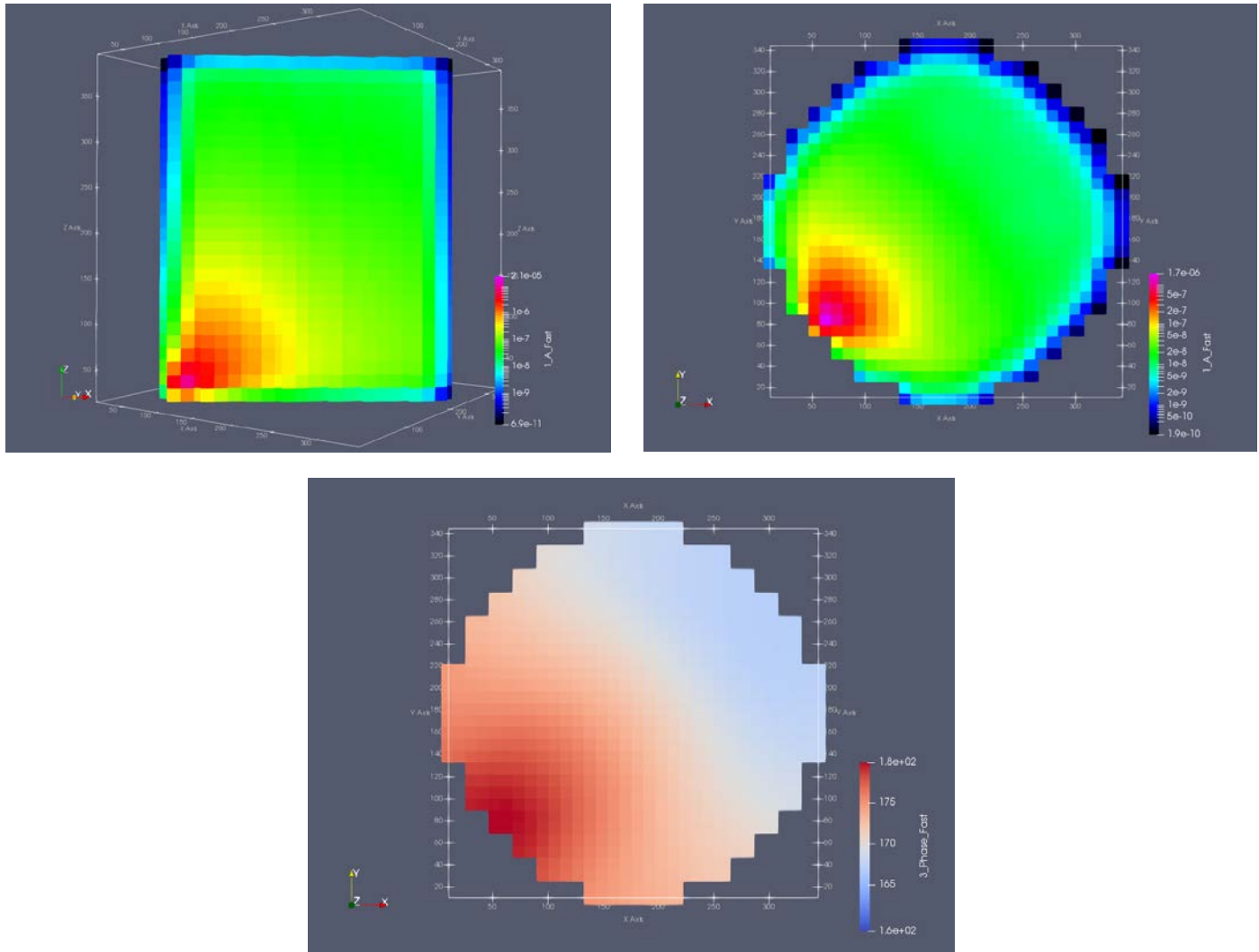


Figure 8: Amplitude (top) and Phase (bottom) with perturbation at (5,7,1) in the fast spectrum with 0.1 Hz

	Data Ranges
Magnitude	0.1 Hz
Amplitude Fast S.	[6.88E-11, 3.24E-6]
Amplitude Thermal S.	[5.01E-11, 0.00208]
Phase Fast S.	[146.82, 179.03]
Phase Thermal S.	[164.59, 179.53]

Table 9: Data ranges with perturbation at (5,7,1) in the fast spectrum with 0.1 Hz

### D3.3 Development of advanced signal processing techniques and evaluation results

It is observed that the neutron noise amplitude in both spectra, i.e., thermal and fast, decreases as the perturbation approaches the edges. Furthermore, the amplitude of the fast spectrum decreases one or two orders more than that of the thermal spectrum and becomes lower than the thermal. Table 10 compiles all the data ranges for the four previous cases.

	(16,16,13)	(1,16,13)	(5,7,13)	(5,7,1)
Magnitude	0.1 Hz	0.1 Hz	0.1 Hz	0.1 Hz
Amplitude Fast S.	[7.504E-5, 2.4511]	[1.011E-7, 0.014]	[1.927E-8, 0.0023]	[6.879E-11, 3.240E-6]
Amplitude Thermal S.	[6.3086E-5, 1.121]	[8.526E-8, 0.212]	[1.657E-8, 0.325]	[5.027E-11, 0.0021]
Phase Fast S.	[168.31, 179.78]	[164.63, 179.88]	[164.11, 179.88]	[146.82, 179.03]
Phase Thermal S.	[168.3, 179.99]	[164.63, 179.99]	[164.11, 179.99]	[164.58, 179.53]

**Table 10: Data ranges with perturbation at four locations in the fast spectrum with 0.1 Hz**

#### 3.1.4.5 Location in edge (5,7,13) and different frequencies

Table 11 shows the data ranges for the case of Section 5.3, when the perturbation is in edge (5,7,13), for the three frequencies. The Table shows that the amplitude range does not change, however the phase ranges increase for the 10 Hz case.

	Data Ranges	Data Ranges	Data Ranges
Magnitude	0.1 Hz	1 Hz	10 Hz
Amplitude Fast S.	[1.927E-8, 0.0023]	[1.88E-8, 0.0023]	[1.818E-8, 0.0023]
Amplitude Thermal S.	[2.168E-8, 0.325]	[2.12E-8, 0.325]	[2.045E-8, 0.325]
Phase Fast S.	[165.11, 179.88]	[175.82, 179.92]	[153.01, 179.31]
Phase Thermal S.	[168.12, 179.99]	[175.79, 179.98]	[152.77, 179.77]

**Table 11: Data ranges with perturbation at (5,7,13) for the three frequencies**

### 3.1.5 Symmetry and linearity in the spatial response with respect to the applied perturbation

This section intends to characterize the symmetry grade and linearity in the spatial response with respect to the applied perturbation of both amplitude and phase of the results. Perturbation locations (16,16,13) and (1,16,13) are used in this section.

#### 3.1.5.1 Neutron noise amplitude

As was already mentioned, the amplitude does not decrease linearly in space; it is the logarithmic scale that must be noted in these cases. Nevertheless, a high grade of symmetry in the spatial response can be noted in Figure 9, as long as the perturbation location remains in a central node.

The small asymmetry shown in Figure 9 is due to the mesh configuration utilized; the reactor simulated actually has four central locations, not one.

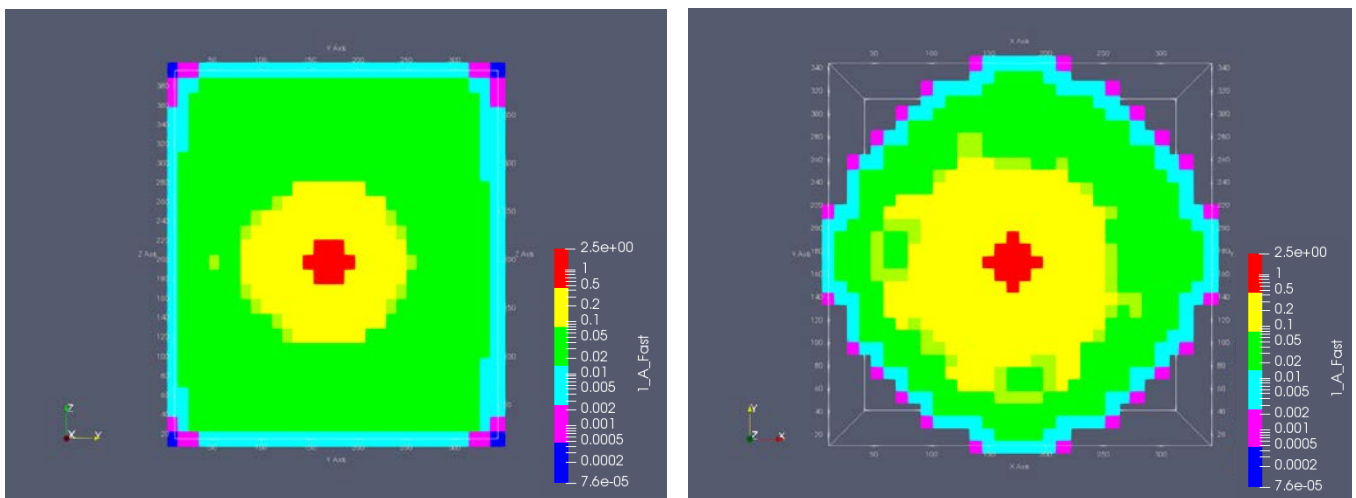


**Figure 9: Symmetry of spatial dependence of the amplitude with a perturbation in the centre**

In the case where the perturbation is near the edge, as shown Figure 10, an asymmetry in the spatial response amplitude can be noticed around the perturbation node.

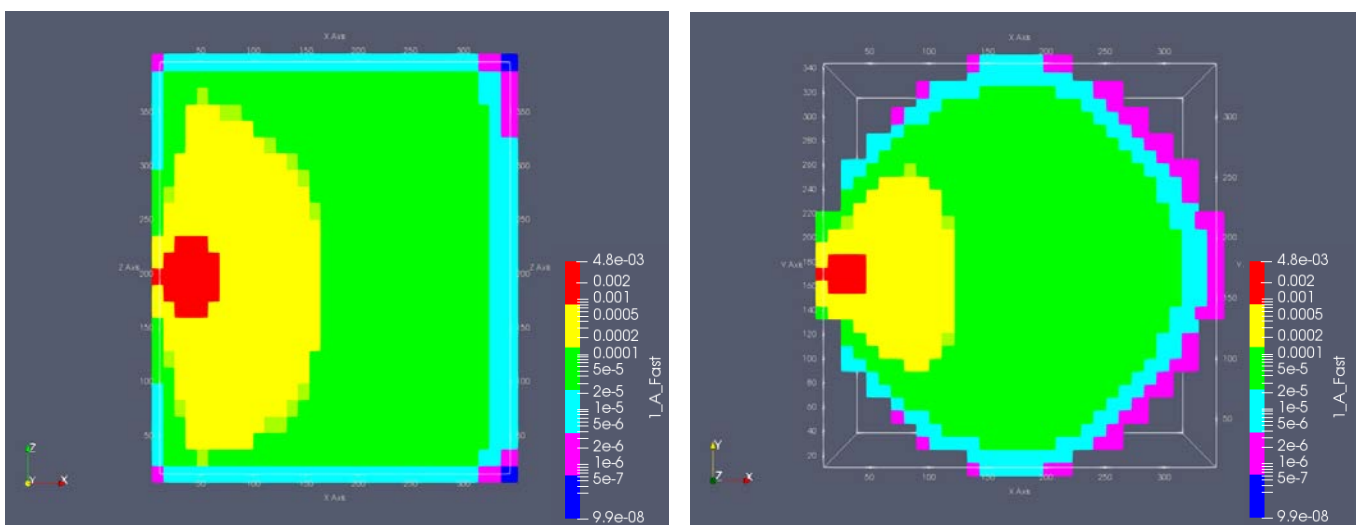


**Figure 10: Asymmetry of the spatial response of the amplitude with a perturbation near the edge**

### 3.1.5.2 Phase

For the phase, a greater symmetry can be appreciated in both cases, in spite of the small asymmetry due to the mesh configuration mentioned before, even when the perturbation is located close to the edges; this can be seen in Figure 11 and Figure 12.

These Figures have a linear scale. A linear spatial response can be clearly noted in the phase; the gradients show a constant variation in space.

It is important to mention that when the perturbation is located in the edges, the core is divided in two parts, if we look at phase. As it is observed in Figure 12, two detectors located at opposite positions around the core would present different phases. This would not be the case in Figure 11 where opposite detectors would have the same phase.

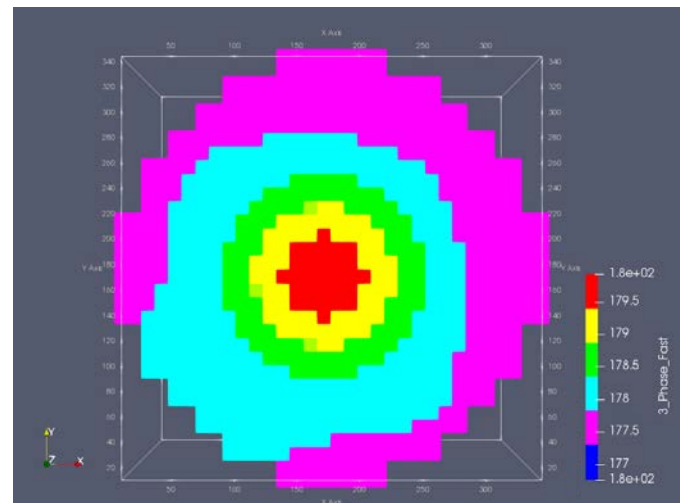
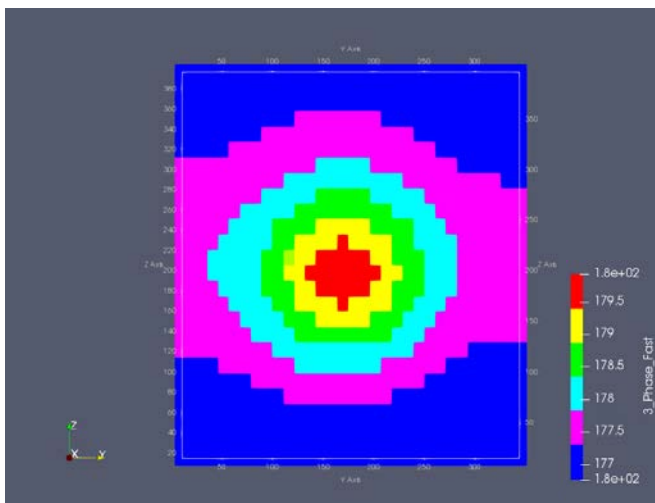


**Figure 11: Symmetry and linearity of the spatial dependence of the phase response with a perturbation in the centre**

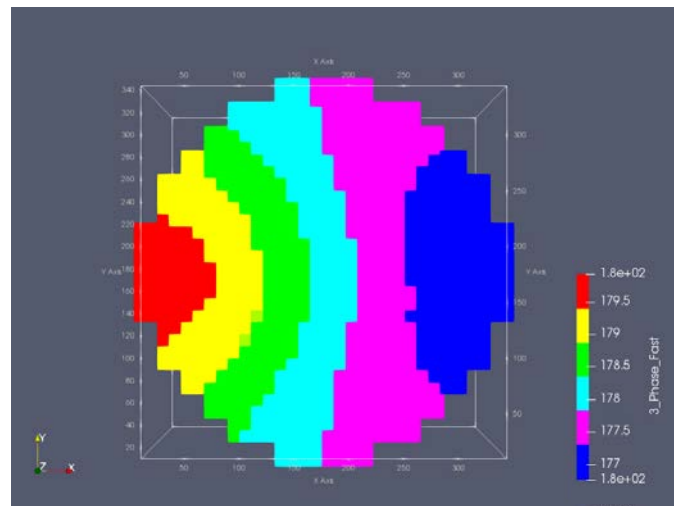
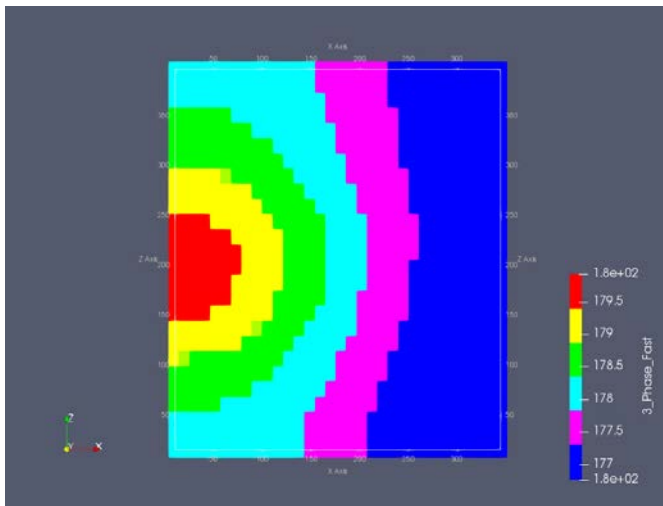


**Figure 12: Symmetry and linearity of the spatial dependence of the phase response for a perturbation at the edge**



### 3.1.6 Some configurations with multiple perturbations

This section compiles several configurations with multiple perturbations that illustrate more characteristics of the simulations and explore the possibility to reproduce some phenomena of the neutron noise observed in KWU reactors.

In these cases several point-like perturbations are summed up to create a large perturbation in the reactor, since it is assumed that the system is linear or at least we can make that assumption for small perturbations. Note that a linear scale is used for the representations of the amplitude and phase.

#### 3.1.6.1 Perturbation in the four central rows (16,16,:) (17,16,:) (16,17,:) (17,17,:)

This is the first, symmetrically axial, case. Furthermore, it is seen in Figure 13 that the highest amplitude is located in the lower half of the rows; this clearly shows a vertical asymmetry of the response.

The variation of the phase throughout the system reduces approximately by 50 % from almost 20 degrees in some previous cases, to 10 degrees in this case, as can be seen in the lower part of Figure 13.

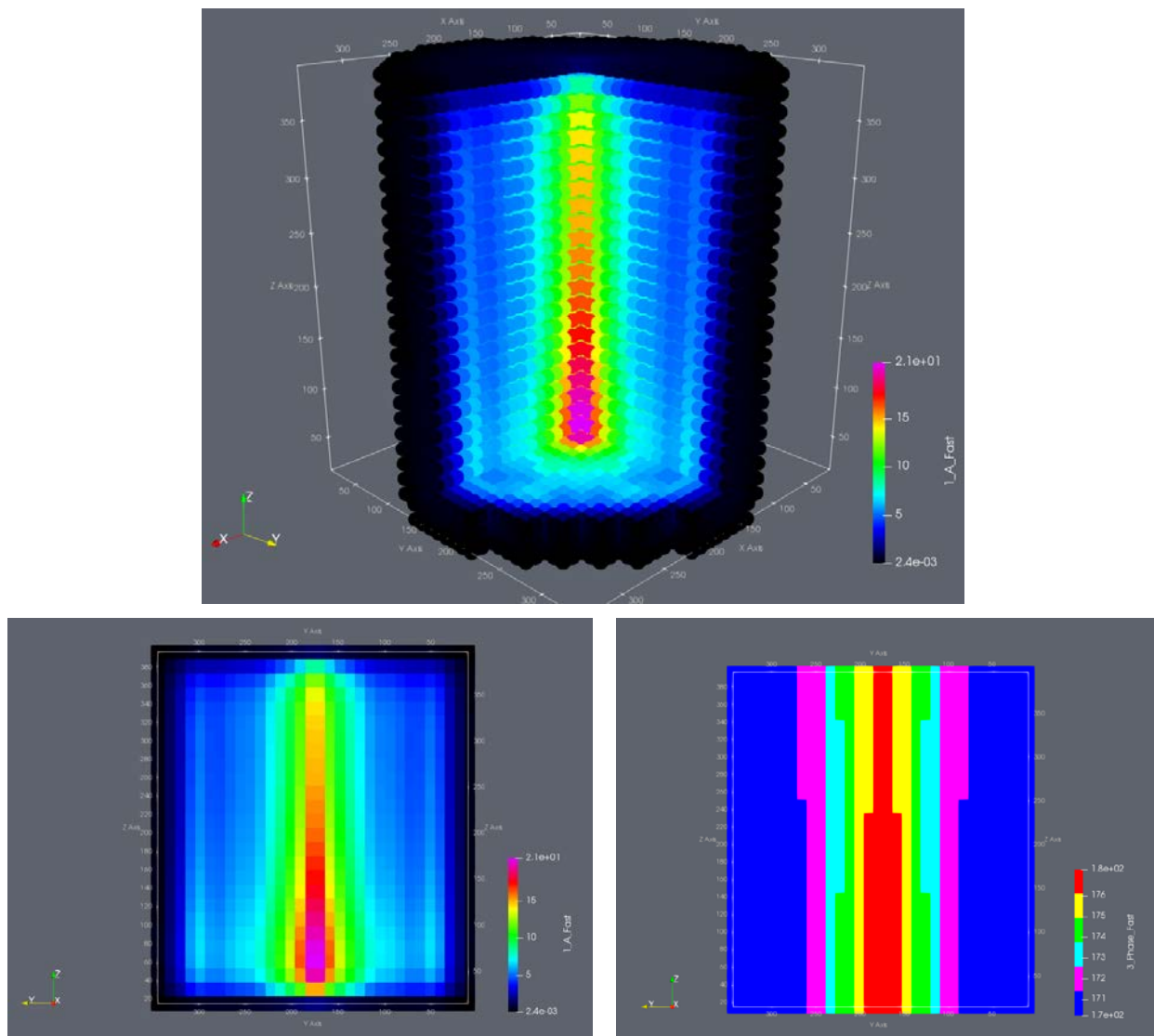


**Figure 13: Variation of amplitude (top and bottom left) and phase (bottom right) when the perturbation is located in four central rows**

### 3.1.6.2 Perturbations in planes $Z=1$ , $Z=2$ and $Z=3$ , one quadrant

This case presents the core with perturbations located in all nodes in the planes  $Z=1$ ,  $Z=2$ ,  $Z=3$ , but only in one quadrant. We can see the corresponding amplitude in Figure 14 and the phase in Figure 15. Note that the figures give both the axial and radial distributions, respectively.

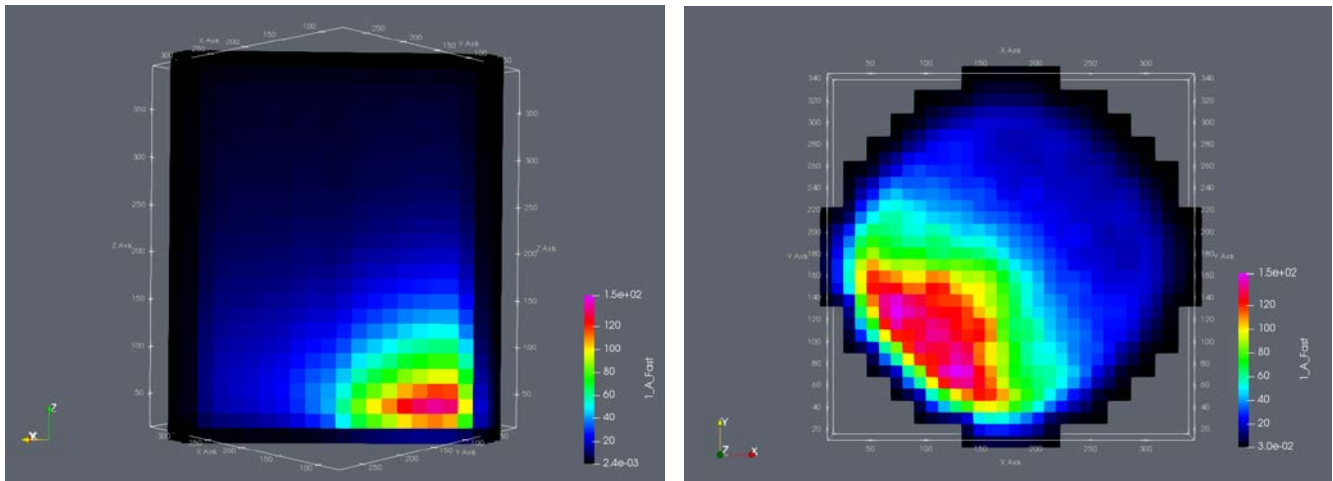


Figure 14: Spatial variation of the amplitude for perturbation in planes  $Z=1$ ,  $Z=2$ ,  $Z=3$ , one quadrant

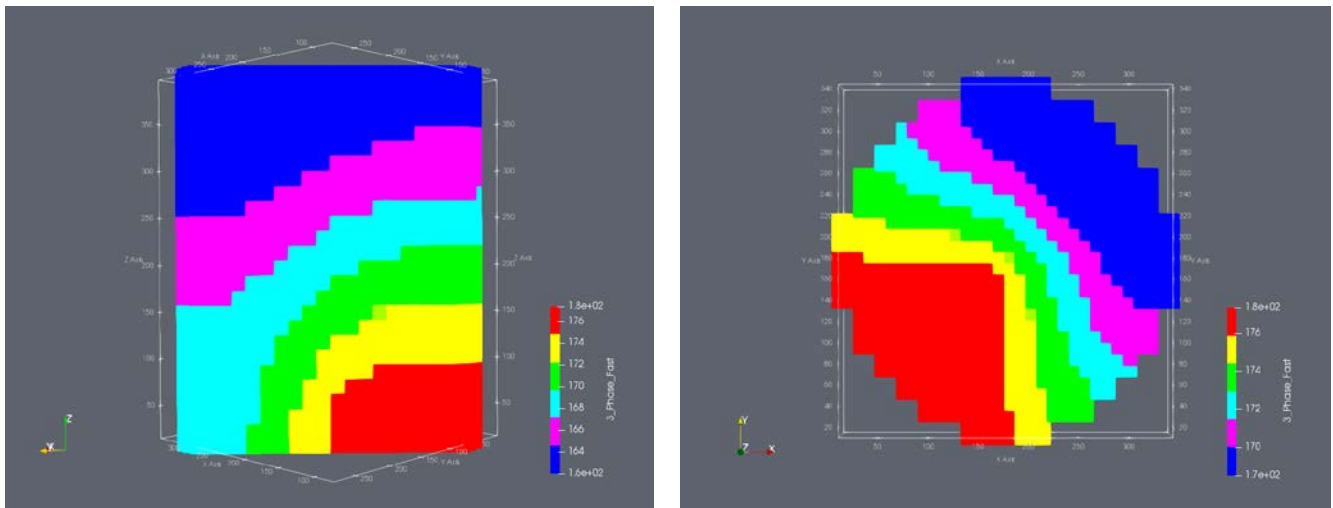


Figure 15: Spatial variation of the phase for perturbation in planes  $Z=1$ ,  $Z=2$ ,  $Z=3$ , one quadrant

### 3.1.6.3 Perturbation in one row in (1,16,:) and (3,16,:)

In this subsection the amplitude and phases are summed up to consider the effect of a perturbation located in a whole row in the edge of the core. In such cases, the rapid spatial attenuation of the induced neutron noise is clearly seen, both just at the edge (Figure 16) or close to it (Figure 17).

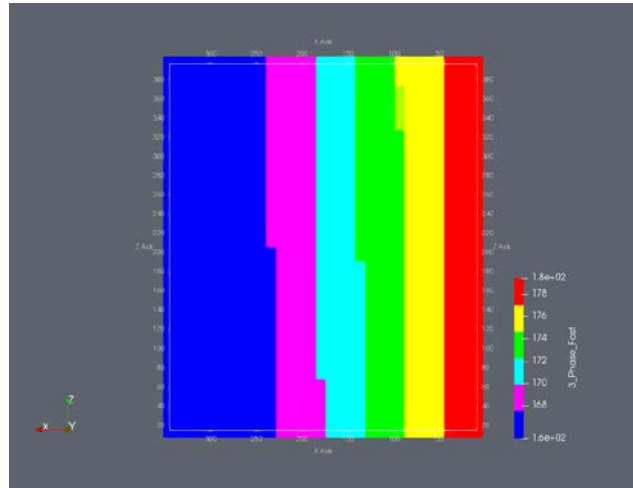
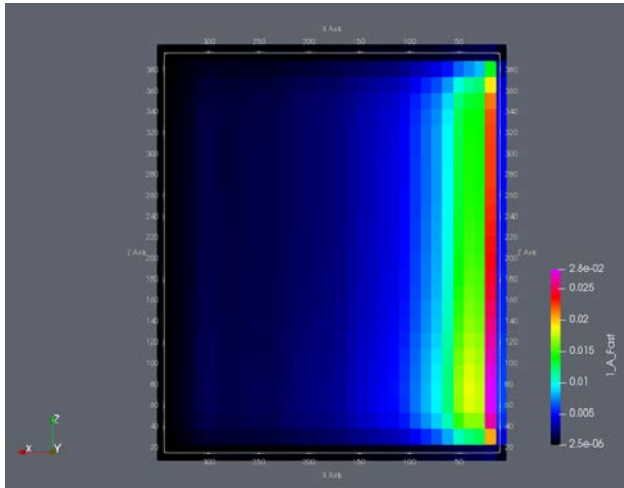


Figure 16: Amplitude and phase with Perturbation in one row in the edge (1,16,:)

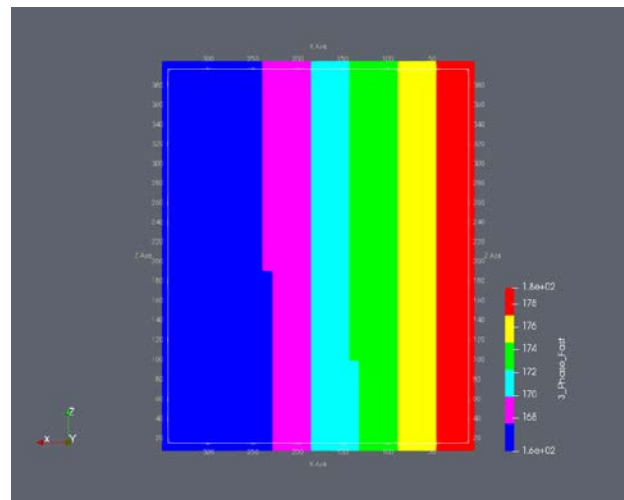
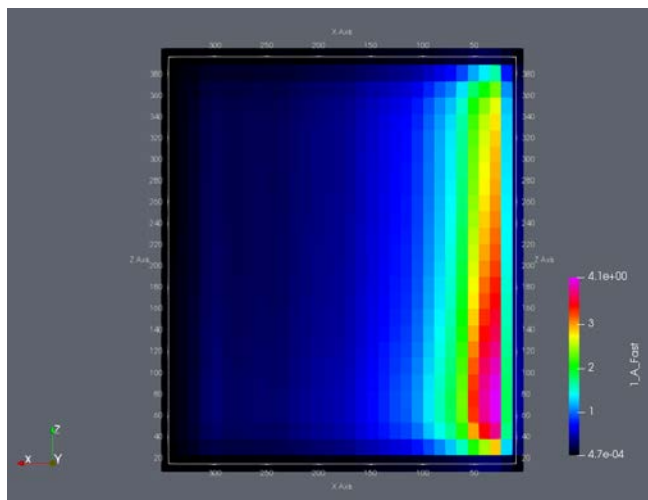


Figure 17: Amplitude and phase with perturbation in one row near to edge (3,16,:)



#### 3.1.6.4 Perturbation in four lines in (5,11,:) (7,9,:) (9,7,:) (11,5,:)

In this subsection four rows (5,11,:) (7,9,:) (9,7,:) (11,5,:) were summed up to create the perturbation; the effect is similar to the previous subsection. Note the spatial attenuation away from the applied perturbation in both the amplitude and phase in Figure 18. We can see that if two detectors were located at opposite positions around the core, they would present slightly different phases. This case experiences a maximum difference of 20 degrees in phase.

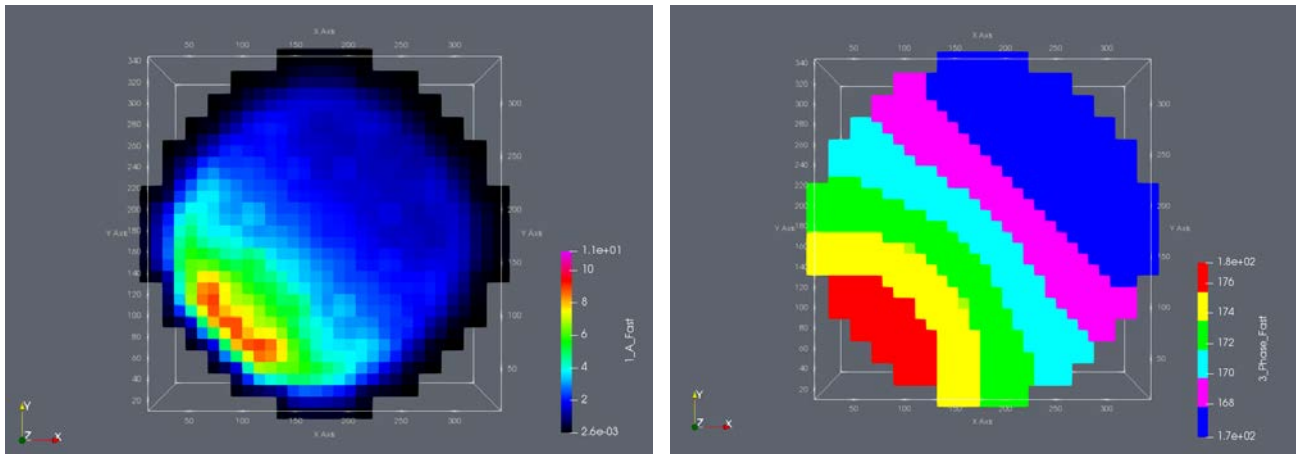


Figure 18 :Amplitude (left) and phase (right) with perturbation in four rows near to edge

### 3.1.7 Distribution of the PSD amplitude

This section analyses the PSD amplitude dependence on the perturbation location. The PSD was computed by multiplying the induced neutron noise with its complex conjugate.

Four distributions of perturbations were selected in this framework:

- Two point-like perturbations in the nodes; (16,16,13) and (2,16,13).
- Perturbations in the four center rows.
- All the nodes of the reactor, i.e., 19552 perturbation cases, were summed up.

The reactor is represented with vertical and horizontal cross sections at central height. In the following two subsections, the energy group is the fast one at 0.1 Hz frequency in the four subsections.

#### 3.1.7.1 Location (16,16,13)

As observed in Figure 19, the PSD amplitude decreases in a very short distance; the image on the left shows that in these cases, with a point-like perturbation far from the edge, we experience a radial attenuation of one order of magnitude in approximately 32 cm and two orders in 75 cm.

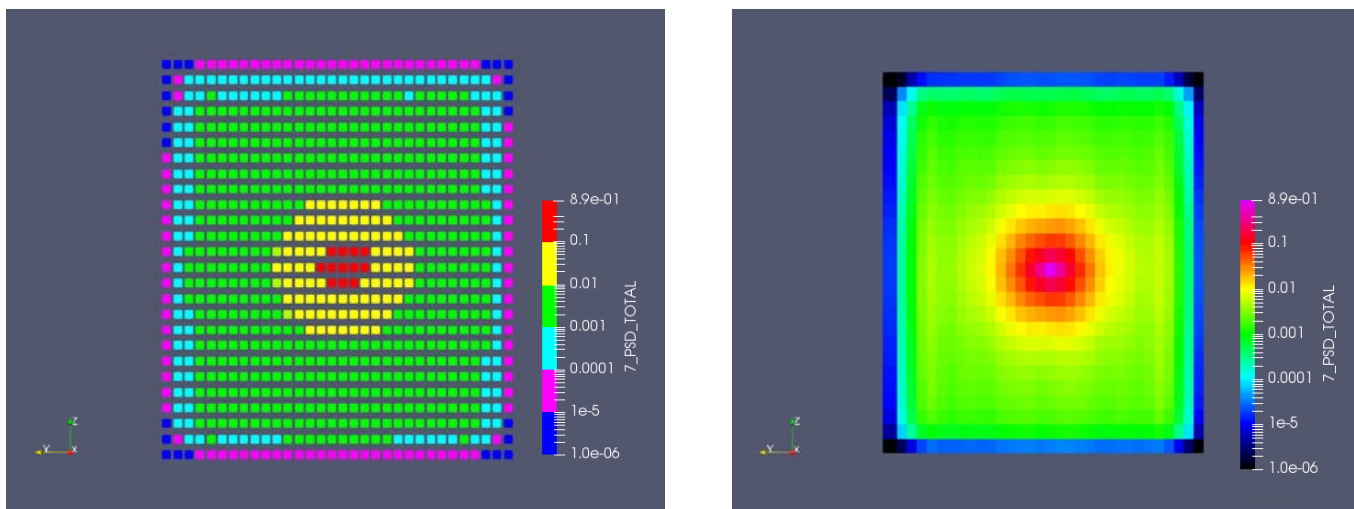


Figure 19: PSD amplitude for a point-like perturbation in location (16,16,13)

### 3.1.7.2 Location (2,16,13)

As observed in Figure 20, the PSD amplitude is attenuated as the perturbation approaches the edge; we can see a greater attenuation in these zones. Besides, the image of the left shows that in these cases the attenuation experiences a clear asymmetry, since, at this position, the PSD amplitude decreases one order of magnitude in 10 cm approximately toward the exterior.

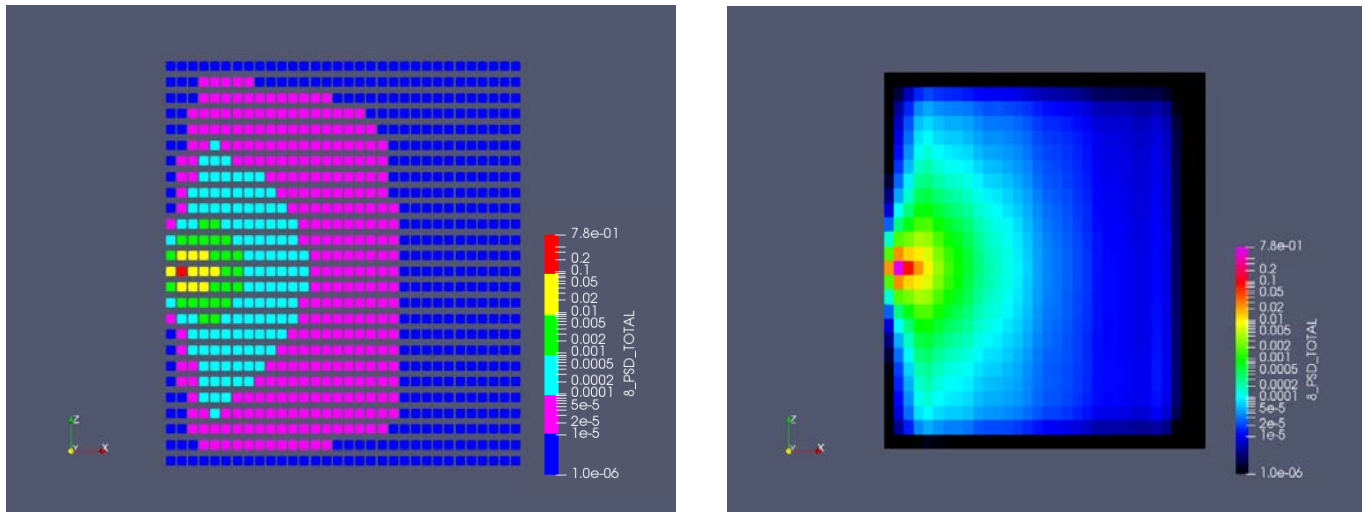


Figure 20: PSD amplitude for a point-like perturbation in location (2,16,13)

### 3.1.7.3 Perturbation in the four center rows (16,16,:) (17,16,:) (16,17,:) (17,17,:)

It is interesting to observe that the PSD amplitude distribution is similar to the amplitude distribution presented before, but in this case the attenuation is greater. We can see that in the lower part, where the PSD has its greater values, the values decrease by 50 % approximately in 10 cm.

In Figure 21 and Figure 22 we can see the distribution of the amplitude with respect to space.

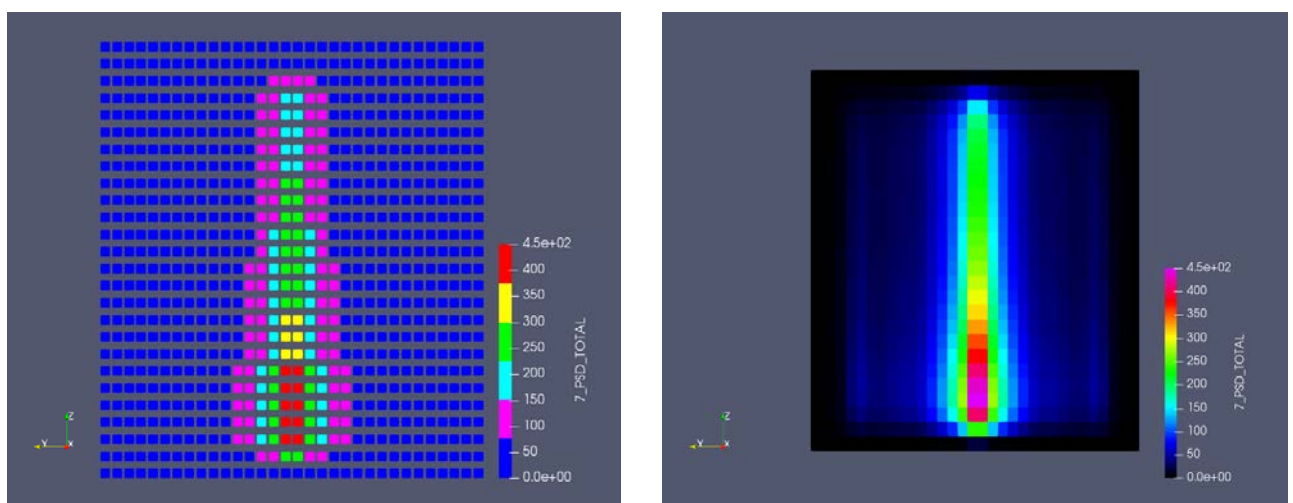


Figure 21: PSD amplitude for a perturbation in the four center rows

D3.3 Development of advanced signal processing techniques and evaluation results

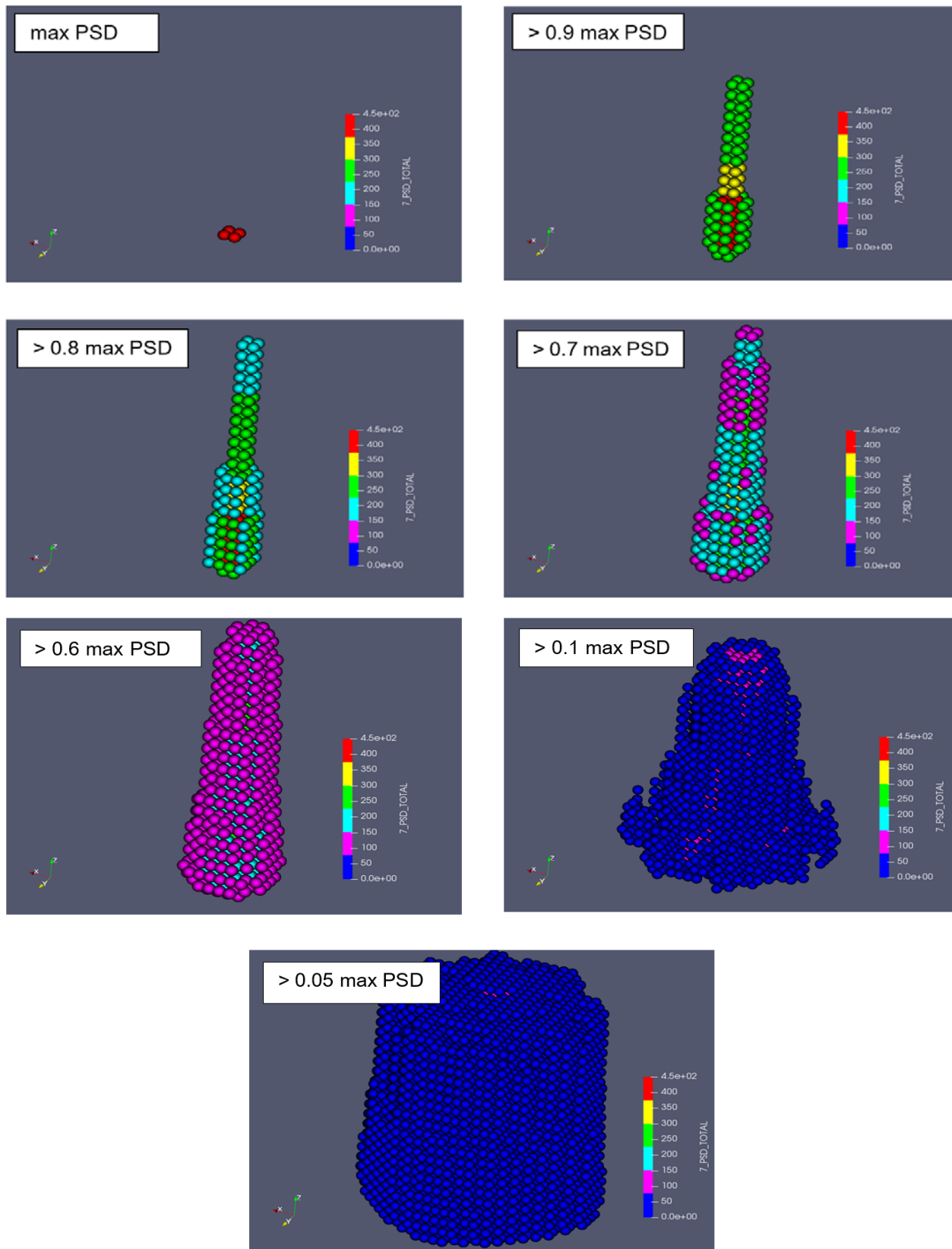


Figure 22: Evolution in space of the PSD amplitude for a perturbation in the four centre rows

#### 3.1.7.4 Perturbations in all nodes in the reactor

When we sum up the perturbations in all reactor nodes, we obtain the distribution shown in Figure 23. As we can see, we have the hottest zones at the bottom on the reactor.

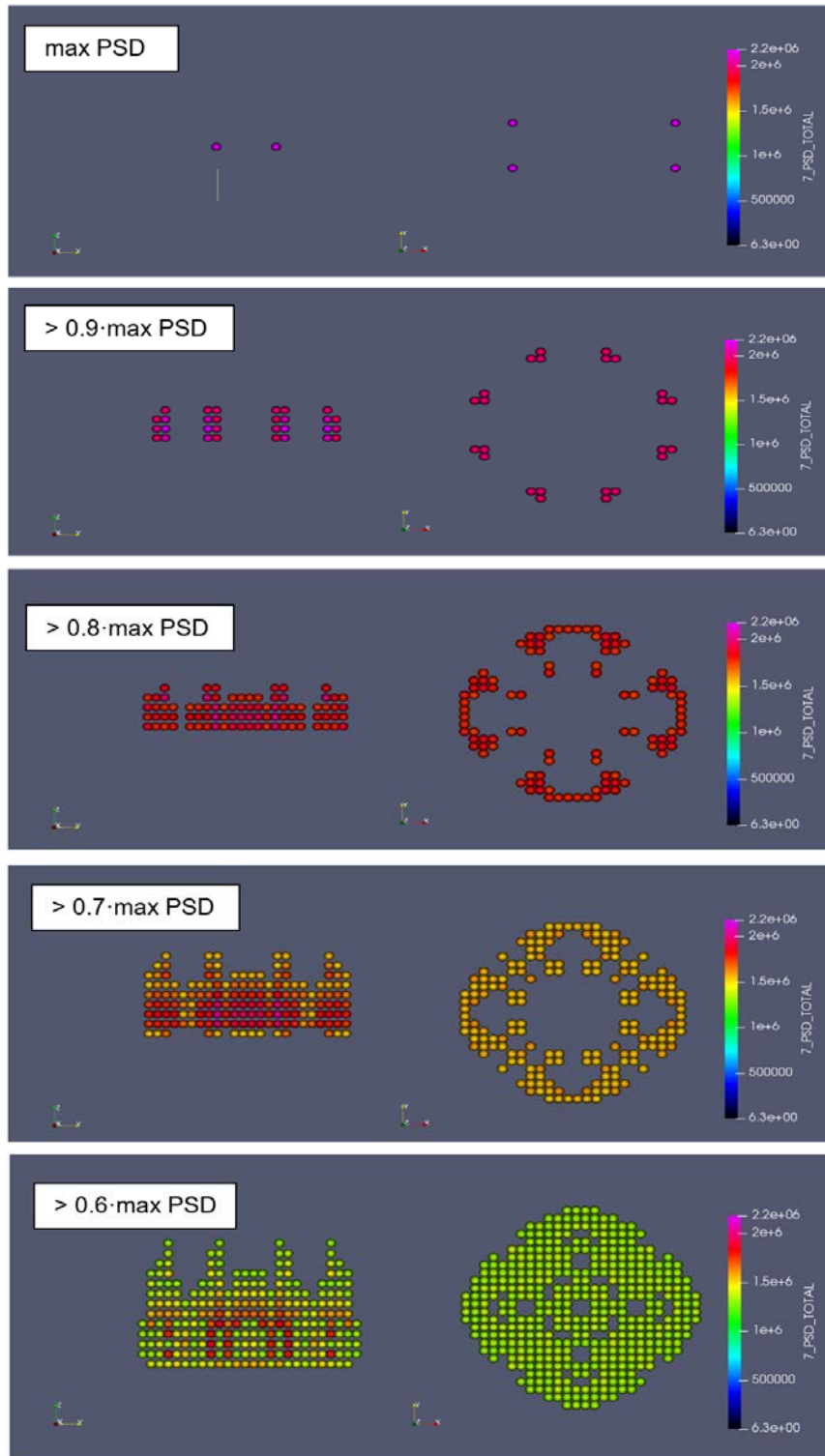


Figure 23: Amplitude distribution of the APSD when perturbations in all reactor nodes are considered.



### 3.1.8 Conclusions

Some conclusions of the presented analyses are summarized hereafter:

- The amplitudes observed in the three considered frequencies are similar to each other.
- The phase difference changes with frequency in both spectra (thermal and fast).
- The thermal amplitude is lower than the fast one when perturbations are away from the edge of the reactor.
- Otherwise, the thermal amplitude is higher than the fast one, when the perturbation is close to the edge.
- When the perturbation is in the center or close to it, a well-defined symmetry is observed.
- When the perturbation is close to the edge, the spatial decay of the response of the system is more pronounced, leading to two well differentiated parts for the response in phase and amplitude.

## 3.2 Analysis of PSI simulated data

In this section, several simulation results based on the transient nodal code S3K are analyzed from the point of view of spectral characteristics of the neutron detector signals. The analysis and observations described in this section are meant at understanding the neutron noise simulated by PSI, as well as some spectral features of the neutron noise observed in KWU reactors. The simulated neutron detectors responses are analyzed with noise analysis techniques and then compiled in tables that present the results in a suitable way to observe the corresponding features for each scenario.

The Tables which show the results that were elaborated to obtain conclusions are the following: On the one hand, the first type of Tables compile the APSDs calculated for all the scenarios considered, On the other hand, the second type of Tables compile the coherence and phase relationships calculated between pairs of signals.

The considered scenarios are analyzed using the Hilbert Huang Transform (HHT) to determine more information than using the traditional Fourier analysis. Due to the stationary character of the signals no new information is expected to emerge; however, the approach can be useful in the future analysis of real data.

### 3.2.1 Analyzed Scenarios

This section describes data of the various analyzed scenarios. The data consist of the responses from in-core and ex-core neutron detectors. Every output of the scenarios includes 8 signals from the ex-core detectors placed at 4 different radial locations and at 2 axial levels, and 48 signals from in-core detectors placed at 8 different radial positions and at 6 axial levels.

Figure 24 shows the core layout with the locations of both the in-core (i.e. O5, N12, J2, J6, G10, G14, C4 and B11) and the ex-core detectors (i.e. S1, S2, S3 and S4). The axial levels are listed from the lower to the higher part, i.e., from axial level 1 (Lv 1) to axial level 6 (Lv 6). The scenarios are divided in three categories: scenarios in which thermohydraulic oscillations are analyzed, scenarios in which mechanical vibrations are simulated, and scenarios simulated with mixed oscillations.

### **3.2.1.1 Thermal-hydraulic oscillations scenarios**

- **Scenario 2.6:** Synchronized fluctuations of inlet coolant flow in all the four coolant loops. The inlet coolant flow is randomly fluctuating with amplitude of  $\pm 1\%$  over the relative flow (100%).
- **Scenario 2.5:** Synchronized fluctuations of inlet coolant temperature between all the four coolant loops. The inlet coolant temperature is randomly fluctuating with amplitude of  $\pm 1$  °C over the mean value of 286.7 °C.

### **3.2.1.2 The mechanical vibrations scenarios**

- **Scenario 5.1 and Scenario 5.2:** Synchronized vibrations of the central cluster of 5 x 5 fuel assemblies only in the **Y-direction** following a white noise signal (i.e. random displacement) with a maximum displacement amplitude of 0.5 mm and 1 mm respectively.
- **Scenario 5.5 and Scenario 5.6:** Synchronized vibrations of the central cluster of 5 x 5 fuel assemblies only in the **XY-direction** following a white noise signal (i.e. random displacement) with a maximum displacement amplitude of 0.5 mm and 1 mm respectively.
- **Scenario 5.3 and Scenario 5.4:** Synchronized vibrations of the central cluster of 5 x 5 fuel assemblies only in the **Y-direction** following a sinusoid signal of 1.5 Hz with a displacement amplitude of 0.5 mm and 1 mm respectively.
- **Scenario 5.7 and Scenario 5.8:** Synchronized vibrations of the central cluster of 5 x 5 fuel assemblies only in the **XY-direction** following a sinusoid signal of 1.5 Hz with a displacement amplitude of 0.5 mm and 1 mm respectively.

### **3.2.1.3 The mixed scenarios**

- **Scenario 4.1 and Scenario 4.2:** Combination of synchronized fluctuations of inlet coolant temperature in all the four loops and synchronized fluctuations of inlet coolant flow in all the four loops synchronized and vibrations of the central cluster of 5 x 5 fuel assemblies, only in the **X-direction**, following a white noise signal (random displacement) with displacement amplitude of 0.5 mm and 1 mm respectively.
- **Scenario 4.3 and Scenario 4.4:** Combination of synchronized fluctuations of inlet coolant temperature in all the four loops and synchronized fluctuations of inlet coolant flow in all the four loops synchronized and vibrations of the central cluster of 5 x 5 fuel assemblies, only in the **X-direction**, following a sinusoid signal of 1.5 Hz with displacement amplitude of 0.5 mm and 1 mm respectively.

In the thermalhydraulic fluctuations, the inlet coolant temperature is randomly fluctuating with amplitude of  $\pm 1^\circ\text{C}$  over the mean value of  $286.7^\circ\text{C}$ . Also, the inlet coolant flow is randomly fluctuating with amplitude of 1% over the relative flow (100%).

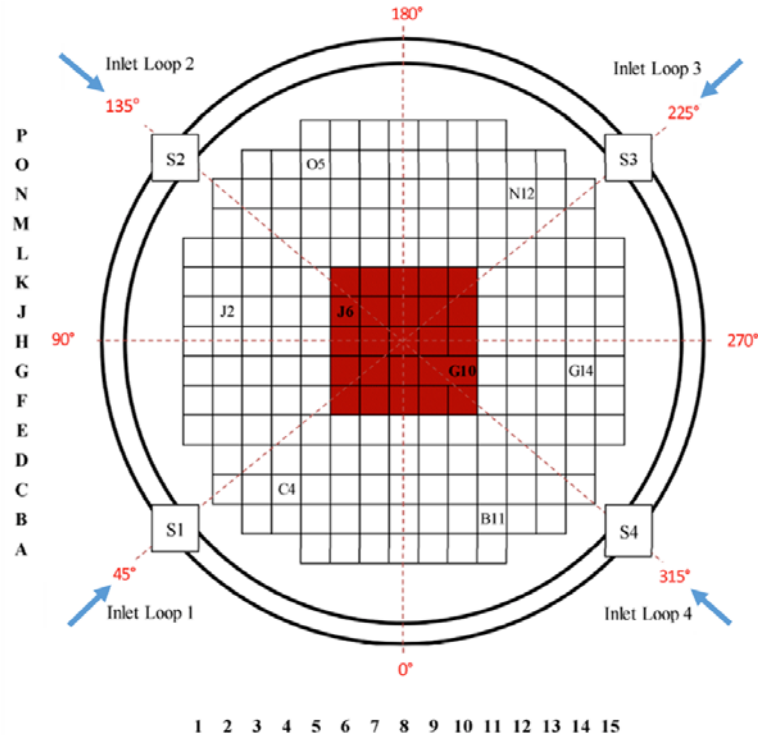


**Figure 24: Radial layout of the sensor strings and fuel elements which are vibrating**

### 3.2.2 Analysis

The analysis made on the scenarios focused on the following:

- Hilbert Huang Transform was applied to the signals to observe possible extra contribution to traditional Fourier analysis.
- Calculation of the APSDs in all the levels and radial positions, in-core and ex-core.
- Coherence and phase analysis between pairs of sensors, in-core and ex-core.
- The above mentioned analyses (APSD, Coherences and Phases) were compiled in Tables to define the spectral features of each scenario.

The goal is to elaborate a map of features so as to recognize specific patterns. This map can also be useful for analysis by machine learning techniques.

#### 3.2.2.1 Hilbert Huang Transform

The Hilbert-Huang Transform is a methodology for signal processing which has been used in many applications. It is an adaptive tool for dealing with non-stationary and non-linear signals. In this sense, its applicability is very similar to Wavelet transform, but the approach is different.

The methodology consists of two parts; the empirical Mode decomposition and the Hilbert transform. The empirical mode decomposition is an iterative algorithm which extracts from the original signal a series of Intrinsic Mode Functions (IMF). By applying it, the original signal  $x(t)$  can be expressed as the sum of a number  $n$  of IMF plus a residual  $r(t)$ . The residual is normally the mean or the trend of the original signal.



$$x(t) = \sum_{i=1}^n IMF_i + r(t) \quad (1)$$

The characteristics of each IMF are the following:

- They are centered in a narrow frequency band
- They have the same number of data points as the original signal
- The zero crossings are equal to the number of relative extrema
- They have symmetrical amplitudes.

In Figure 25 we can see an example of the Intrinsic Mode Functions of a signal corresponding to the scenario.

Once the original signal is divided into these IMFs, the Hilbert transform can be applied to all of them. As compared to traditional Fourier analysis, Hilbert approach is local, and it is defined as follows:

$$H[h(t)] = \frac{1}{\pi} P \int_{-\infty}^{\infty} \frac{h(\tau)}{t - \tau} d\tau \quad (2)$$

where P is the Cauchy principal value and h(t) is a certain IMF. The kernel  $\frac{1}{t - \tau}$  confers to the transform a local character as opposed to the Fourier analysis. Practical applications come from the analytical signal g(t) defined as the complex function:

$$g(t) = h(t) + iH[h(t)] \quad (3)$$

The instantaneous amplitude and phase are:

$$\begin{aligned} a(t) &= \sqrt{h^2 + H^2[h]} \\ \phi(t) &= \tan^{-1} \left( \frac{H[h]}{h} \right) \end{aligned} \quad (4)$$

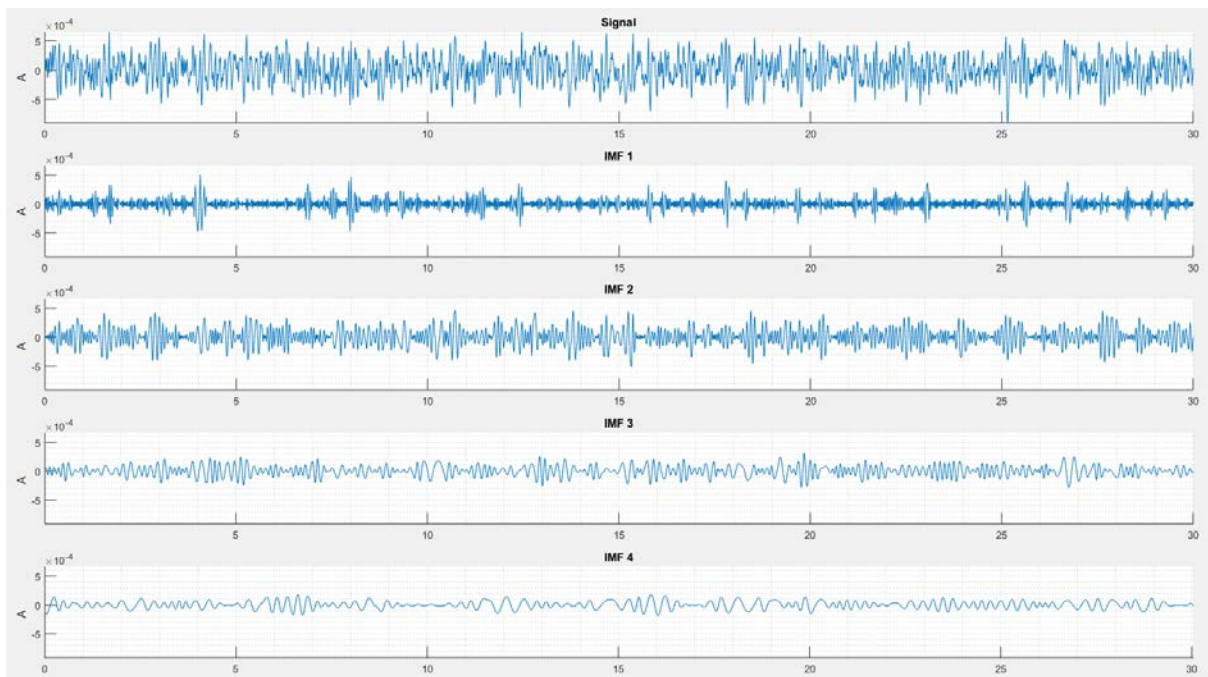
so that the instantaneous frequency is the time derivative of the phase divided by  $2\pi$ :

$$f = \frac{1}{2\pi} \frac{d\phi}{dt} \quad (5)$$

Instantaneous frequency, instantaneous amplitude and time can be plotted in a 3D colour map in order to see both the frequency content and the energy of the signal along the time span considered.

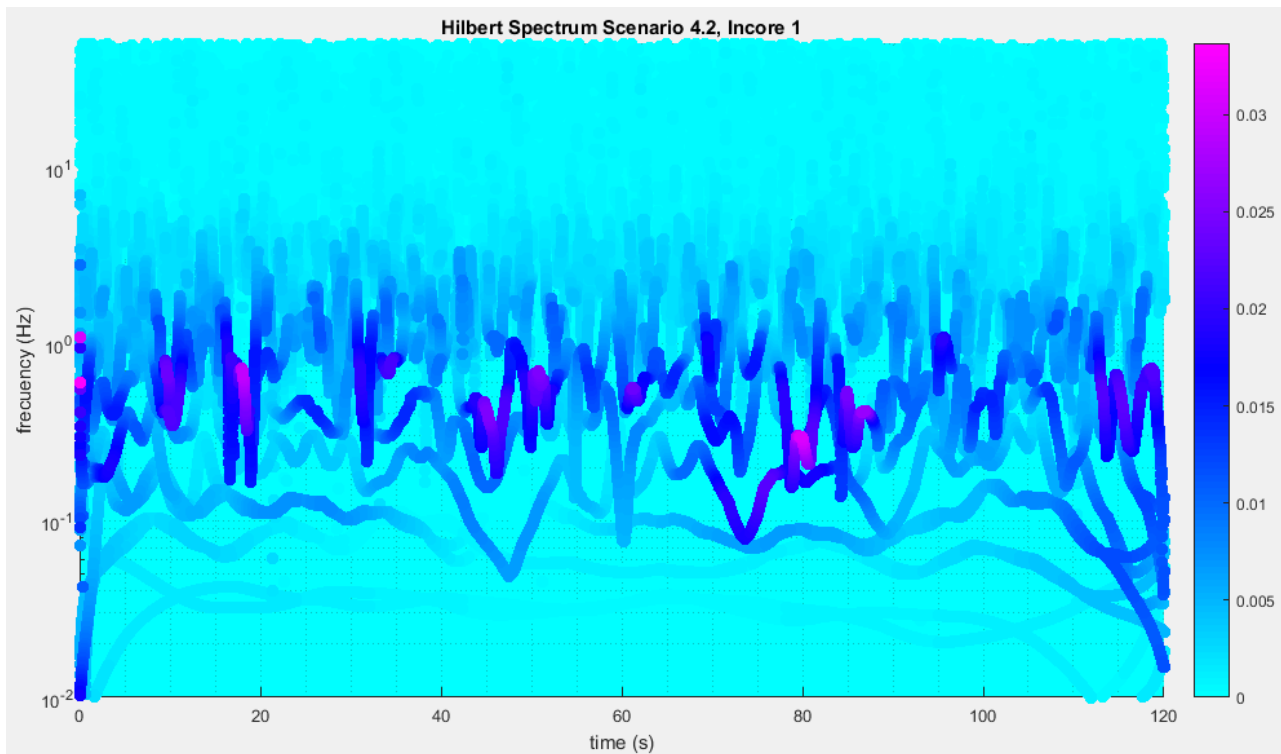
For Nuclear Power Plant applications, the HHT can be used for detrending, denoising, filtering, detecting anomalies in non-stationary data, etc. In many cases, the plant data used for noise analysis is stationary, so a traditional Fourier analysis could be enough to extract features from the signals. Nevertheless, HHT gives more information about frequency and energy content of the signal than traditional Fourier analysis. Besides, all this info coming from the application of HHT could be used as an input to machine learning algorithms.

### D3.3 Development of advanced signal processing techniques and evaluation results



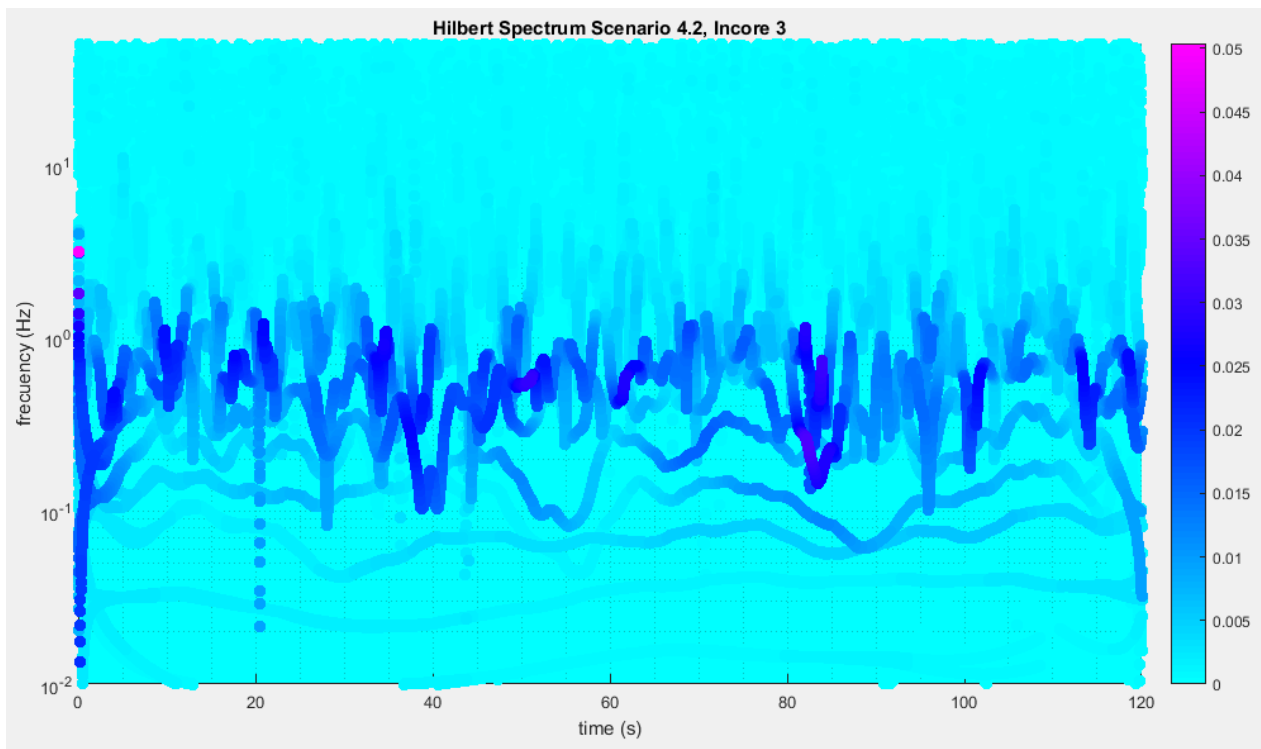
**Figure 25: Signal and 4 first IMFs of scenario 1.1**

Figure 26, Figure 27 and Figure 28 correspond to spectrograms calculated using HHT. The data used correspond to the mixed scenarios, specifically **Scenario 4.2**: Combination of synchronized fluctuations of inlet coolant temperature in all the four loops and synchronized fluctuations of inlet coolant flow in all the four loops synchronized and vibration of the central cluster of 5 x 5 fuel assemblies, only in the **X-direction**, following a white noise signal (random displacement) with displacement amplitude 1 mm.



**Figure 26: Hilbert Spectrum, Scenario 4.2, Incore 1**

*D3.3 Development of advanced signal processing techniques and evaluation results*



**Figure 27: Hilbert Spectrum, Scenario 4.2, Incore 3**

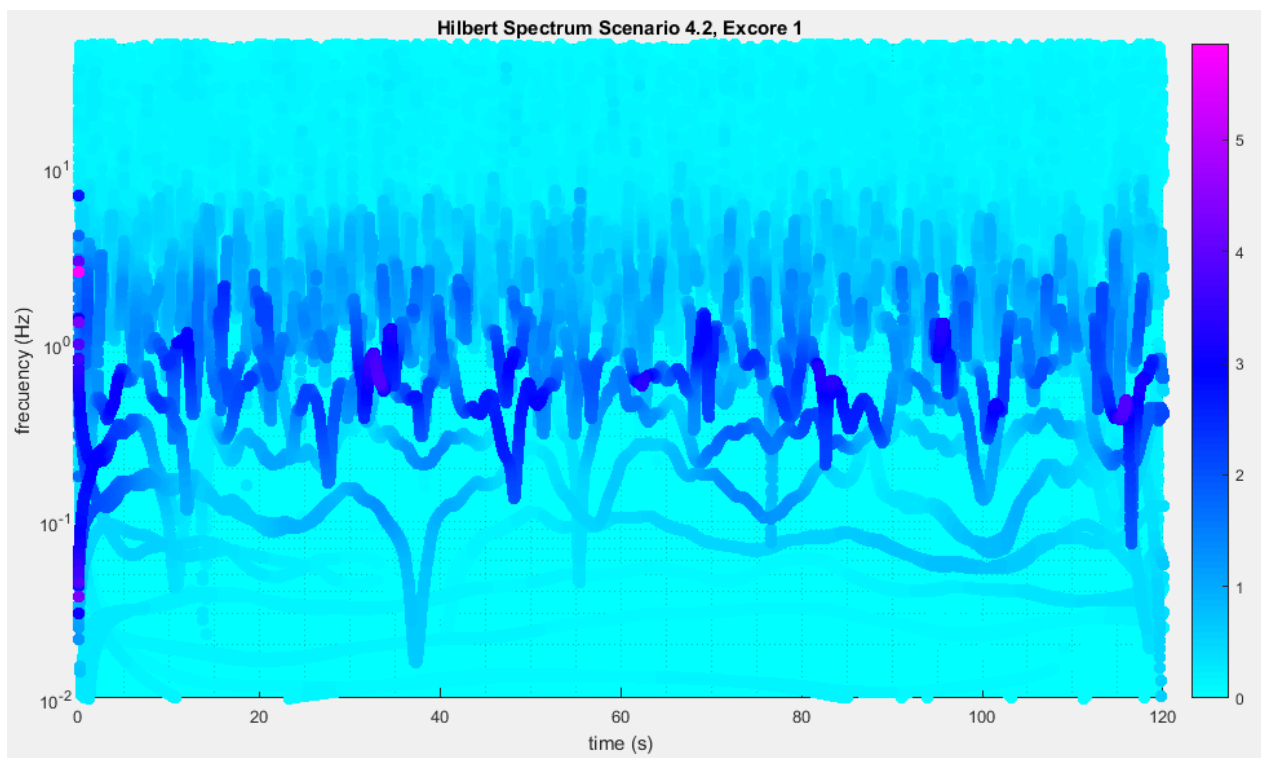


**Figure 28: Hilbert Spectrum, Scenario 4.2, Excore 1**

As can be seen in Figure 26, the content of the signal is very constant in time, and most of the content is located below 1 Hz, this is why the scale in the axes is logarithmic.

HHT is a very useful technique for non-stationary data and for creating time-frequency-amplitudes plots. Nevertheless, the signals we have analyzed from the simulators (S3K) in the time domain are stationary. For this reason, it is much more convenient to apply a traditional Fourier analysis in order to identify the features of the noise in the different scenarios.

### **3.2.2.2 Observations on thermohydraulic scenarios**

- **Scenario 2.6:** Synchronized fluctuations of inlet coolant flow in all the four coolant loops. The inlet coolant flow is randomly fluctuating with amplitude of  $\pm 1\%$  over the relative flow (100%).
- **Scenario 2.5:** Synchronized fluctuations of inlet coolant temperature between all the four coolant loops. The inlet coolant temperature is randomly fluctuating with amplitude of  $\pm 1$  °C over the mean value of 286.7 °C.

#### **Regarding the APSDs:**

Figure 29 shows a comparison between the APSDs of the thermohydraulic oscillations scenarios **Scenario 2.6** and **Scenario 2.5** (flow and temperature fluctuations, respectively). It has to be mentioned that the APSDs presented in this report have been normalized in order to ensure that the area below the curve is equal to the signal's variance. So, we can see that the variance is much bigger in the temperature fluctuation scenarios. In addition, we can appreciate that most content of the signal is located below 1 Hz.

### D3.3 Development of advanced signal processing techniques and evaluation results

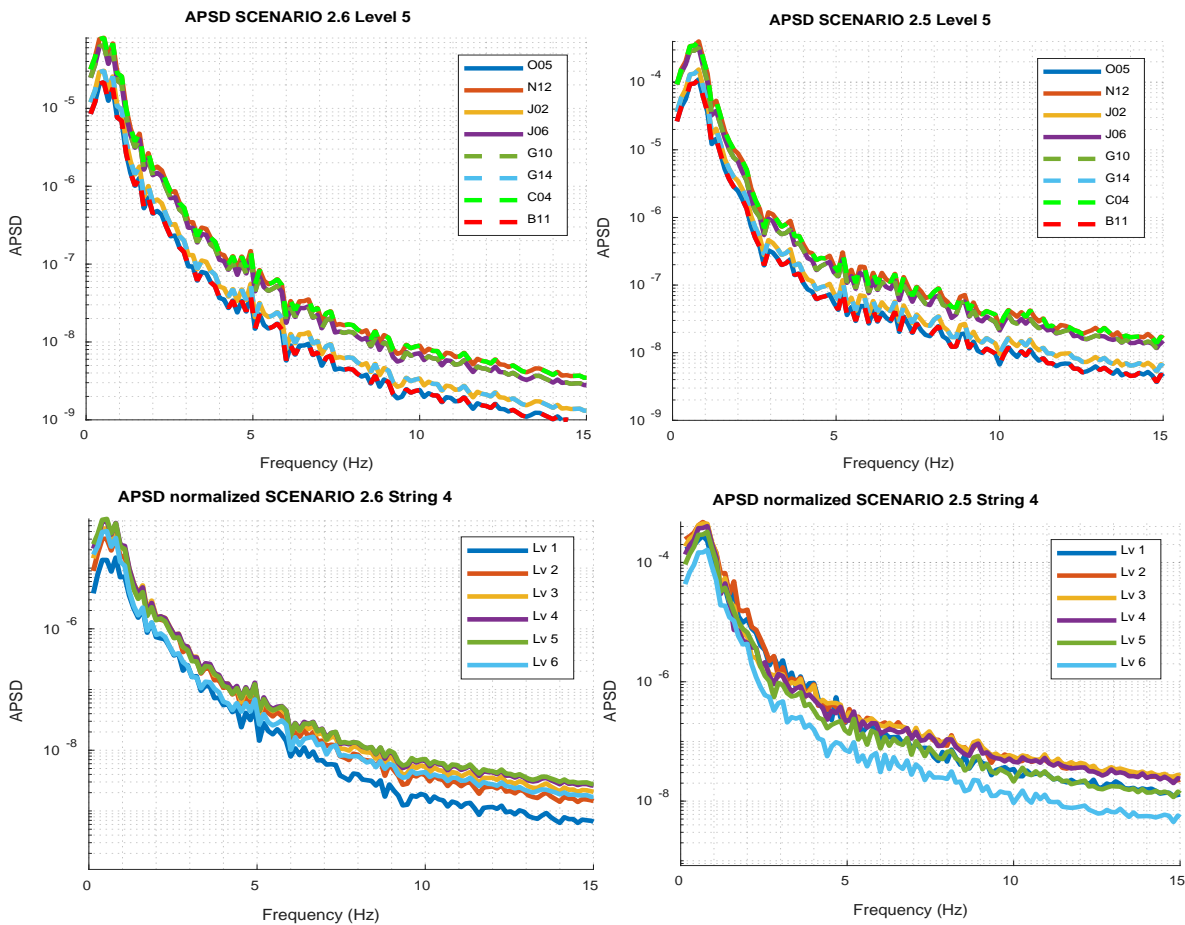


**Figure 29: APSDs of thermal-hydraulic scenarios, flow and temperature oscillations, left and right side respectively. Upper figures correspond to all radial positions at level 5, lower figures correspond to all levels in only one radial position (String 4). Note that Lv 1 and Lv 6 are the lowest and the uppermost levels respectively.**

The standard deviations of neutron noise for neutron detector strings J02 and J06 are presented in Figure 30. It is observed in both cases that the standard deviation due to the temperature oscillations is the highest of the three cases, followed by the flow fluctuations scenario, and lastly by the one due to vibrations of the fuel elements. These axial profiles coincide to a large extent with the profiles observed in reality.

### D3.3 Development of advanced signal processing techniques and evaluation results

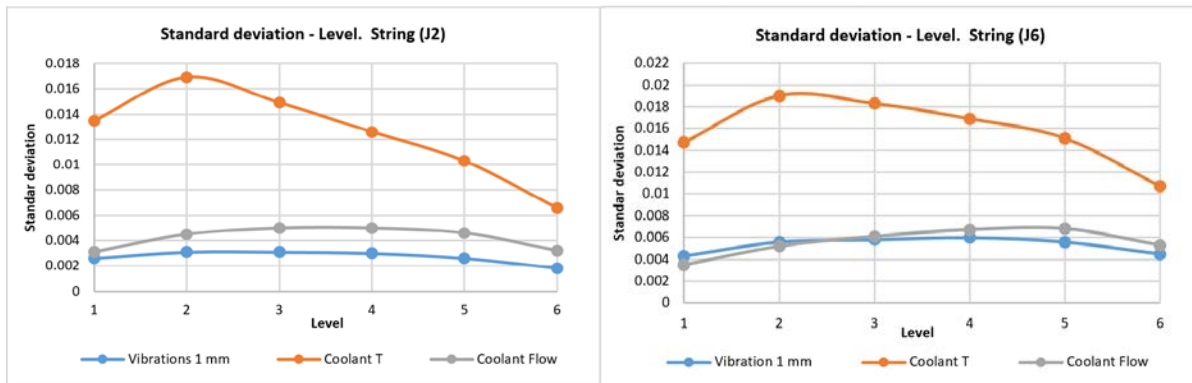


**Figure 30: Standard deviation versus axial level in string J02 and J06. Note that Lv 1 and Lv 6 are the lowest and the uppermost levels, respectively.**

#### Regarding the Coherences and phases:

As can be observed in Figure 31, for both scenarios, the coherence decreases as the distance from the reference sensor increases and, additionally, all the sensors are in phase above 5 Hz.

In this type of scenarios, it is possible to identify, at low frequencies, the characteristic linear phase that indicates the presence of a transport phenomenon. This is not observed in the scenarios of fuel elements vibration.

The slope of the linear phase difference is proportional to the transit time. This means that the higher the slope, the higher the transit time and therefore, the phenomenon of transportation is very slow. Temperature phenomena are characterized as slow processes (from the point of view of dynamics), indicating their big inertia. In this sense, we can see in Figure 31 (right hand side) that the slope of the linear phase in the low frequency range is much higher than the one in Figure 31 (left hand side). This indicates that the flow phenomena are transported much faster than the temperature phenomena. In fact, the phase difference between in-core detectors at different axial positions in real plant data show a linear phase with a very low slope. Keeping in mind this, the flow perturbations scenarios show more similarities with real plant data than the ones with temperature perturbations.

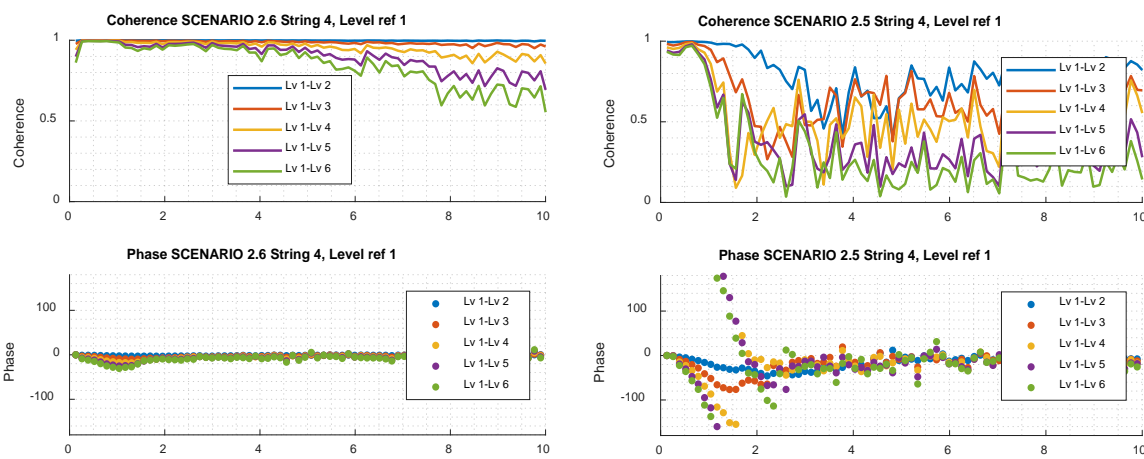


**Figure 31: Coherence and phase fluctuation between incore sensors of the flow oscillation (left) and temperature oscillation (right) scenarios. Note that Lv 1 and Lv 6 are the lowest and the uppermost level, respectively.**



### 3.2.2.3 Observations on mechanical vibrations scenarios

- **Scenario 5.1 and Scenario 5.2:** Synchronized vibrations of the central cluster of 5 x 5 fuel assemblies only in the **Y-direction** following a white noise signal (i.e. random displacement) with a maximum displacement amplitude of 0.5 mm and 1 mm respectively.

#### Regarding the APSDs:

In these scenarios the detectors are located at different azimuthal distances from the vibrating fuel elements cluster. It can be observed in Figure 32 that the variance decreases with the distance and that the APSDs from detectors at the same distance overlap. The highest amplitudes of the response are located in the frequency range 0–15 Hz. The lower part of the spectra (i.e. at higher frequencies) does not show high noise amplitude.

It is interesting to note that the pair of sensors with the highest amplitude are N12-C04, and the lowest amplitude is in J02-G14, transversal to the vibration direction.

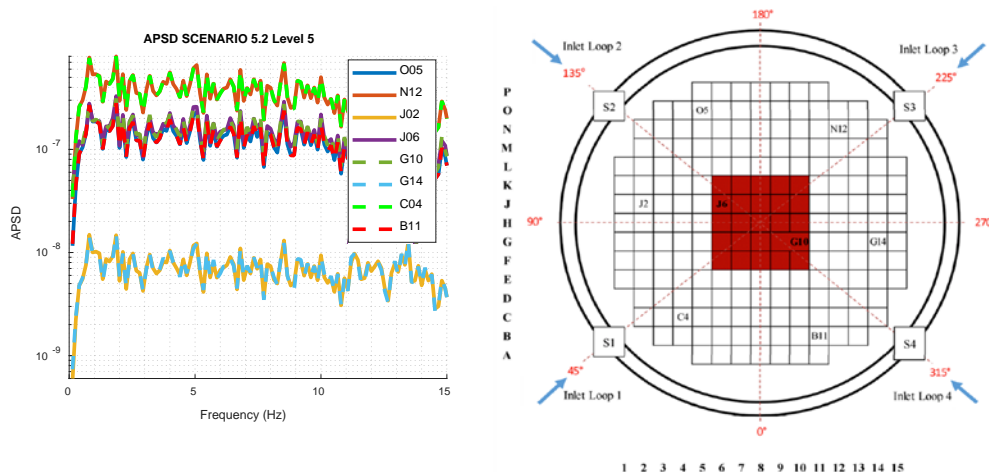


**Figure 32: Scenario 5.2. APSDs of the radial positions at level 5.**

#### Regarding the Coherences and phases:

The coherence is equal to one or almost one in all the pairs plotted. Regarding the radial phase relationship, we have a transverse distribution of phase that divides the reactor into two halves clearly differentiated by  $\pm 180^\circ$ ; the strings (O5, N12, J2, J6) on the upper part, and the strings (G10, G14, C4, B11) to the lower part. We must highlight the fact that this out-of-phase relationship takes place in the whole frequency range. In addition, the phase relationship is zero between detectors located at the same string (i.e. same azimuthal location).

### D3.3 Development of advanced signal processing techniques and evaluation results

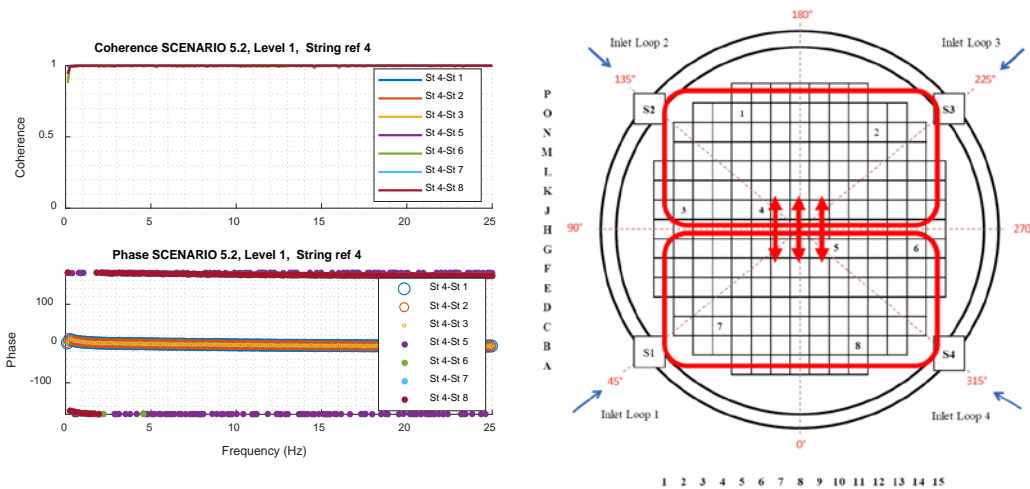


**Figure 33: Scenario 5.2. from left to right; APSDs of the radial positions at level 5, Coherences and Phases and radial distribution of out-of-phase zones.**

- **Scenario 5.5 and Scenario 5.6:** Synchronized vibrations of the central cluster of 5 x 5 fuel assemblies only in the **XY-direction** following a white noise signal (i.e. random displacement) with a maximum displacement amplitude of 0.5 mm and 1 mm respectively.

#### Regarding the APSDs:

In these scenarios the variance is more related to the distance, the pair of sensors with the biggest amplitude is J06-G10, which is the closest to the vibration, but in this case this pair is oriented almost perpendicular to the vibration.

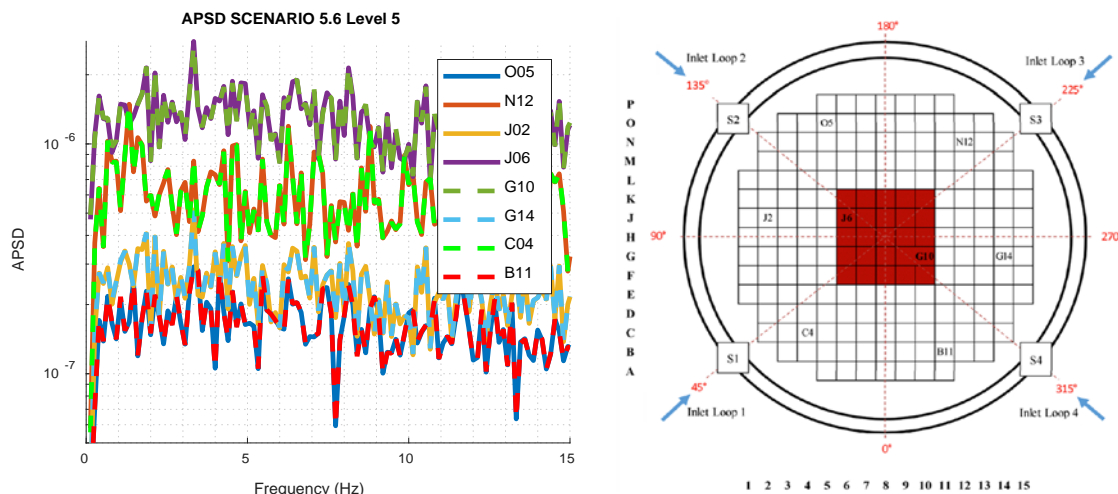


**Figure 34: Scenario 5.6. APSDs of the radial positions at level 5.**

#### Regarding the Coherences and phases:

When the direction of the vibrations is diagonal (direction XY), we can observe a greater coherence in those couples of sensors whose direction is close to that of the vibration. It can also be observed that the out-of-phase relationship is clear between pairs of sensors in different halves, but the angle of the phase relationship is somewhat intermediate (among 0° to ±180°) between pairs of sensors located transversally to the vibration.

### D3.3 Development of advanced signal processing techniques and evaluation results

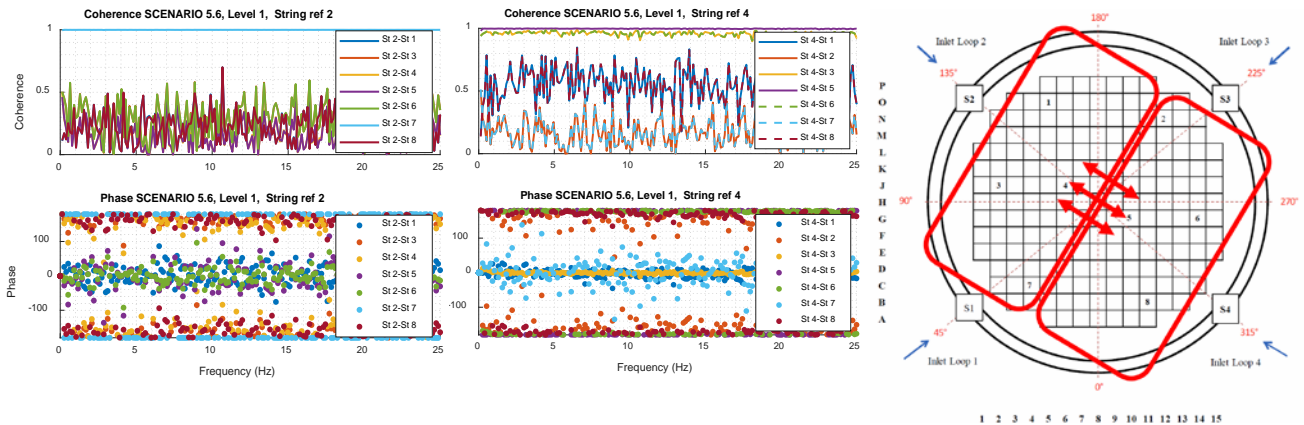


**Figure 35: Scenario 5.6. from left to right; Coherences and Phases at level 1 (string reference 2 and 4 respectively) and radial distribution of out-of-phase zones.**

- **Scenario 5.3 and Scenario 5.4:** Synchronized vibrations of the central cluster of 5 x 5 fuel assemblies only in the **Y-direction** following a sinusoid signal of 1.5 Hz with a displacement amplitude of 0.5 mm and 1 mm respectively.

#### Regarding the APSDs:

In these scenarios the different detectors are located at different azimuthal distances from the vibrating fuel elements cluster. For these sinusoidal vibrations, we can see from Figure 36 a clear peak at 1.5 Hz and some smaller peaks in the multiples of 1.5 Hz. The variance decreases with the distance and the APSDs from detectors at the same distance overlap. The highest amplitudes of the response are located in the frequency range 0–15 Hz. The lower part of the spectra (i.e. at higher frequencies) does not show high noise amplitude.

It is interesting to note that the pair of sensors with the highest amplitude are N12-C04, and the lowest amplitude is in J02-G14, transversal to the vibration direction; this is similar to **Scenario 5.1** and **Scenario 5.2**:

#### Regarding the Coherences and phases:

The coherence is equal to one or almost one in all the pairs plotted, but now we can see some peaks at multiples of 1.5 Hz. Regarding the radial phase relationship, we have a transverse distribution of phase that divides the reactor into two halves clearly differentiated by  $\pm 180^\circ$ ; the strings (O5, N12, J2, J6) on the upper part, and the strings (G10, G14, C4, B11) to the lower part. We must highlight the fact that this out-of-phase relationship takes place in the whole frequency range. In addition, the phase relationship is zero between detectors located at the same string (i.e. same azimuthal location).

### D3.3 Development of advanced signal processing techniques and evaluation results

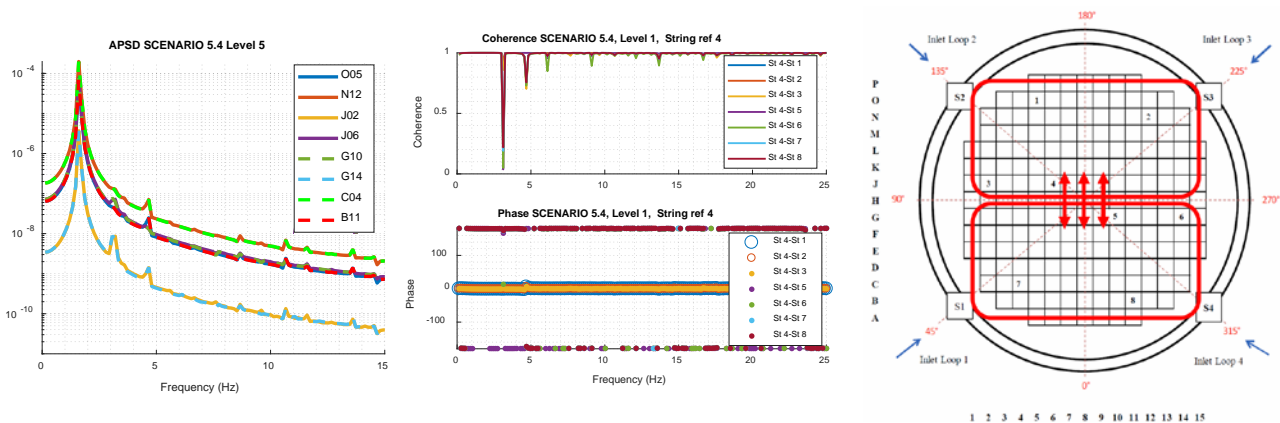


**Figure 36: Scenario 5.4. from left to right; APSDs of the radial positions at level 5, Coherences and Phases and radial distribution of out-of-phase zones.**

- **Scenario 5.7 and Scenario 5.8:** Synchronized vibrations of the central cluster of 5 x 5 fuel assemblies only in the **XY-direction** following a sinusoid signal of 1.5 Hz with a displacement amplitude of 0.5 mm and 1 mm respectively.

#### Regarding the APSDs:

In these scenarios the variance is more correlated to the distance as can be seen in Figure 37, the pair of sensors with the biggest amplitude is J06-G10, which is the closest to the vibration, but in this case this pair is oriented almost perpendicular to the vibration.

#### Regarding the Coherences and phases:

In this scenario there are sinusoidal vibrations, different from the random vibrations we have in **Scenario 5.5** and **Scenario 5.6**. We can observe some differences:

- The Coherences in all cases are equal to one or almost one in all the pairs plotted, but now we can see some peaks at multiples of 1.5 Hz. This coherence does not depend on either the distance to the fuel assembly vibrations, or the distance between the pair of sensors.
- The phase relationship shows a slight rotation. This time, the strings 4 and 2 (J06 and N12) are in phase. This is different from what is seen in **Scenario 5.5** and **Scenario 5.6**. with random vibrations. This can be compared with Figure 35.

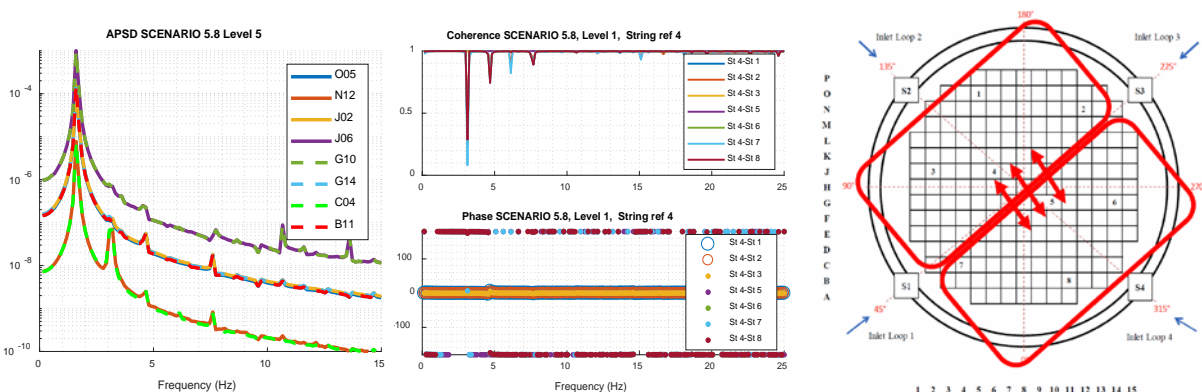


**Figure 37: Scenario 5.8. from left to right; APSDs of the radial positions at level 5, Coherences and Phases and radial distribution of out-of-phase zones.**

### 3.2.2.4 Observations on the mixed scenarios

In this subsection two groups of mixed scenarios are compared; these two groups only differ in the type of vibrations: in **Group 1** the vibrations are random, whilst in **Group 2** they are sinusoidal.

- **Scenario 4.1 and Scenario 4.2:** Combination of synchronized fluctuations of inlet coolant temperature in all the four loops and synchronized fluctuations of inlet coolant flow in all the four loops synchronized and vibrations of the central cluster of 5 x 5 fuel assemblies, only in the **X-direction**, following a white noise signal (random displacement) with displacement amplitude of 0.5 mm and 1 mm respectively.

- **Scenario 4.3 and Scenario 4.4:** Combination of synchronized fluctuations of inlet coolant temperature in all the four loops and synchronized fluctuations of inlet coolant flow in all the four loops synchronized and vibrations of the central cluster of 5 x 5 fuel assemblies, only in the **X-direction**, following a sinusoid signal of 1.5 Hz with displacement amplitude of 0.5 mm and 1 mm respectively.

#### Regarding the APSDs:

Note the following aspects in the APSDs from Figure 38:

- The variance is similar in both cases and is directly related to the distance to the vibrating fuel assemblies.
- The decrease is bigger in Group 2 (sinusoidal vibrations).
- There is a resonance peak at 1.5 Hz in Group 2.

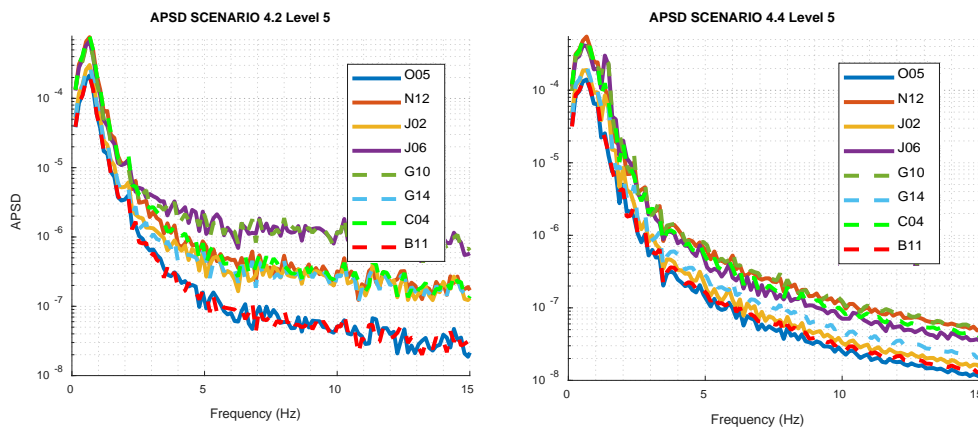


**Figure 38: Scenario 4.2 and Scenario 4.4. APSDs of the radial positions at level 5**

#### Regarding the Coherences and phases:

As can be seen in Figure 39, the first aspect to mention is that in Group 2 (sinusoidal vibrations) we cannot observe two zones with out-of-phase relationship. This aspect is interesting, because when we have only sinusoidal vibrations, the reactor is divided in two zones, but the thermal-hydraulic oscillations seem to cancel this distribution and produce only one zone in phase for all the frequency range. Also note that there is only out-of-phase relationship in Group 1 from 5 Hz, and the bigger the amplitude is, the earlier the out-of-phase relationship starts.



### D3.3 Development of advanced signal processing techniques and evaluation results

We can see in Figure 39 that the bigger the amplitude is, the bigger the coherence is.

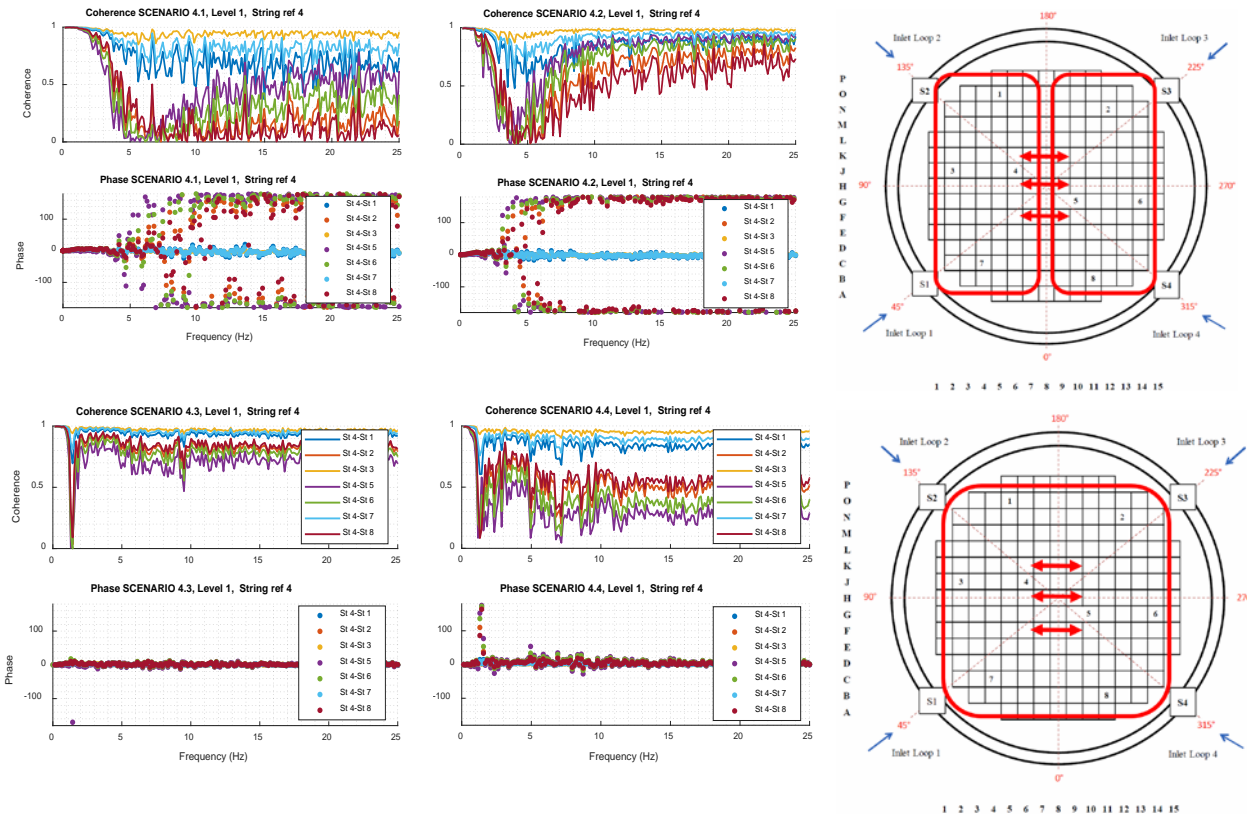


**Figure 39: From left to right; Coherences and Phases and radial distribution of phase relationships. The upper figures correspond to the Group 1 random vibrations (Scenario 4.1 and Scenario 4.2), The Lower figures correspond to the Group 2 sinusoidal vibrations (Scenario 4.3 and Scenario 4.4)**

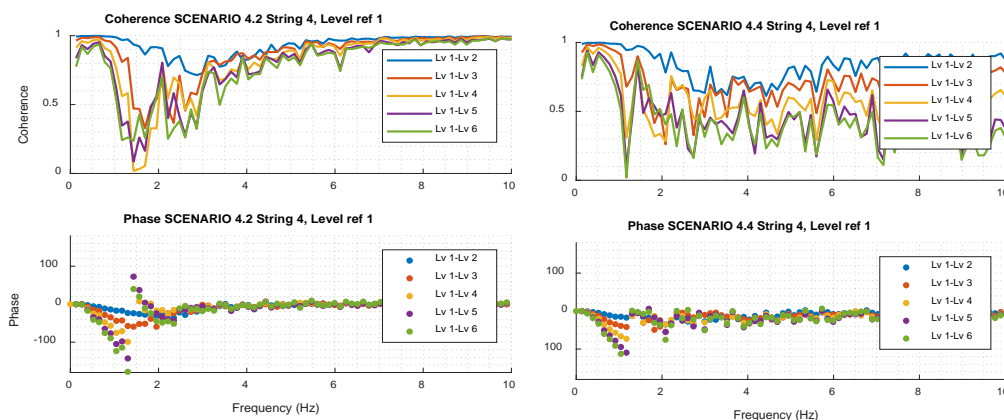


**Figure 40: Coherences and Phases in a same string, same axial position between incore sensors of the Scenario 4.2 and Scenario 4.4. Note that Lv 1 and Lv 6 are the lowest and the uppermost levels, respectively.**

In the longitudinal coherences and phases (see Figure 40), a high slope is seen in the linear phase that indicates a low speed of the transportation phenomenon. This differs considerably from real cases, where we can observe a low slope (see Figure 41), that indicates a high speed of the transport phenomenon. This may suggest that the amplitude of the temperature oscillations are much bigger than the flow oscillations, since the predominant linear phase belongs to the phenomenon with higher amplitude.



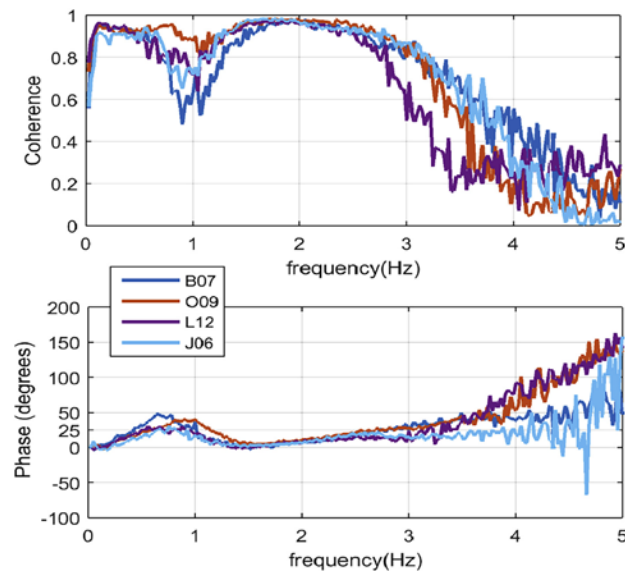


**Figure 41: The phase relationships between Lv 1 and Lv 6 in-core sensors (lower and upper sensors, respectively) of a same string in a KWU-PWR.**

### 3.2.3 Compilation of the data and discussion

As mentioned above, the results are compiled in two types of Tables. Tables of type A compile representative APSDs for all the scenarios which are considered, whilst Tables of type B compile representative coherences and phases between representative pairs of signals for all the scenarios considered. Both types of Tables have the same structure and are referring to the same scenarios.

#### 3.2.3.1 General Structure of the tables

Both types of Tables have the same structure:

From left to right (in columns) we can see the graphics corresponding to flow fluctuation, temperature fluctuation, vibrations of the fuel assemblies (grouped in four columns, two for random vibrations and two for sinusoidal vibrations) and finally the mixed scenarios with all the three types of oscillations (two columns, the upper part for random vibrations and the lower part for sinusoidal vibrations).

From top to bottom, the Table shows the graphs corresponding to the in-core simulated signals (the first two rows), and the graphs corresponding to the ex-core ones (the last two rows).

The first series of Tables compile APSDs, coherences and phases between pairs of signals, (pairs considered representative) for all the above-mentioned scenarios:

The scenarios of thermal-hydraulic oscillations:

- **Scenario 2.6**
- **Scenario 2.5**

The scenarios of mechanical vibrations:

- **Scenario 5.1 and Scenario 5.2**
- **Scenario 5.5 and Scenario 5.6**
- **Scenario 5.3 and Scenario 5.4**
- **Scenario 5.7 and Scenario 5.8**

The mixed scenarios:

- **Scenario 4.1 and Scenario 4.2**
- **Scenario 4.3 and Scenario 4.4**

We can see the Table of type A and the Table of type B in Figure 42 and Figure 43 respectively.

### D3.3 Development of advanced signal processing techniques and evaluation results

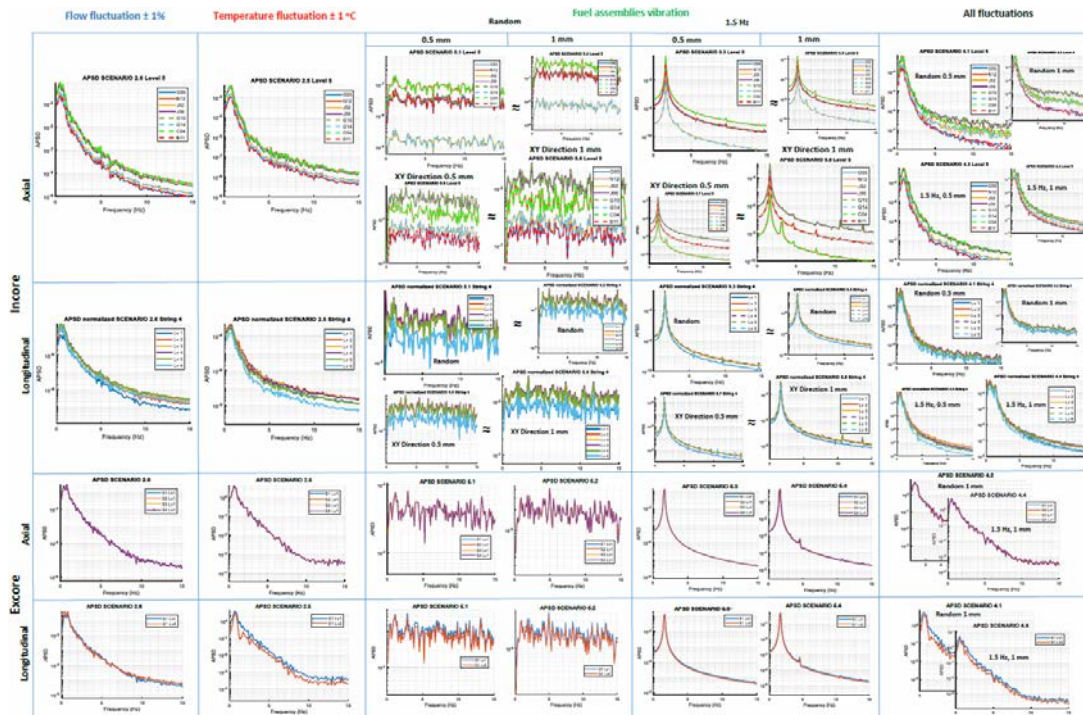


Figure 42: APSDs of the first series of tables

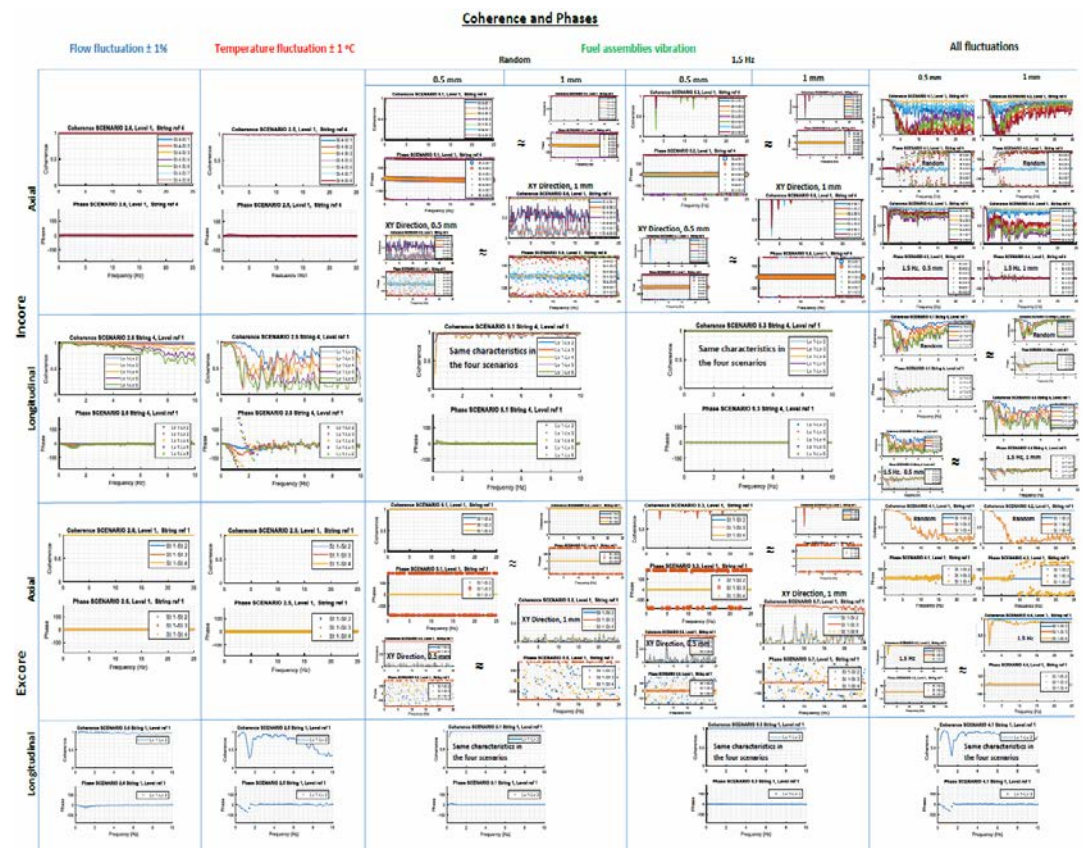


Figure 43: Coherence and phase relationships of the first series of tables

### **3.2.3.2 Discussion**

The simulated thermal-hydraulic and mechanical oscillation scenarios seem to produce separately several spectral characteristics as observed in real neutron noise phenomenology. Three main characteristics observed in the phenomenology of neutron noise and the possible phenomena associated to their causes are discussed in the next subsections.

#### **High transit speed of the transport phenomenon**

In real data from KWU plants, the phase difference relationships between in-core sensors of a same string show a very low slope, pointing out the existence of a transport phenomenon with a quite high transit speed, as shown in Figure 41. The real case is similar to what is observed in the coolant flow oscillation simulated scenarios. Therefore, this characteristic seems to be linked to flow perturbations at the inlet, which, unlike the temperature oscillations scenarios, transport along the core almost instantly.

#### **Response amplitude at low frequencies**

Neutron noise below 1 Hz has its highest spectral amplitude around 1 Hz. This characteristic seems to be related to the thermal-hydraulic oscillations that are produced in the core and whose response range is located around 1 Hz, as can be seen in Figure 38. Temperature and flow oscillations are not directly comparable in a quantitative way. Nevertheless, in this amplitude range, it can be said that the main component of the amplitude seems to be due to temperature oscillations; since this perturbation produces a neutron noise response amplitude four times higher than the flow oscillations and the fuel assembly perturbations scenario, as can also be seen in Figure 30. Besides, the amplitude of neutron noise depends on the amplitude of the imposed perturbation. For example, if more fuel assemblies are simultaneously vibrating, or their vibration displacement is larger, then the noise amplitude due to this mechanism will be enhanced. That can be easily observed, by comparing the noise amplitude in the frequency domain between **Scenario 5.1** and **Scenario 5.2**.

#### **Out-of-phase relationship between opposite detectors**

The thermal-hydraulic oscillation simulations are able to justify and reproduce a big part of the spectral characteristics of the neutron noise. However, these scenarios are not enough to explain the out-of-phase relationship observed between opposite ex-core sensors in KWU reactors. For this reason, the mechanical vibration scenarios are particularly interesting, specifically, the scenario, where a cluster of fuel assemblies is vibrating. These scenarios lead to an out-of-phase relationship over a wide frequency range, including the 0–15 Hz band as it is observed in real KWU-PWR data. This fact could suggest that, clusters of fuel assemblies are vibrating in a specific way and causing the characteristic of an out-of-phase relationship in real plants.

### **3.2.4 Conclusions**

Regarding the scenarios with thermal-hydraulic perturbations:

- A linear phase difference is observed between upper and lower in-core detectors located at the same azimuthal location; this was found to correspond to a transport phenomenon. The transit times calculated from both scenarios show that the flow perturbations are transported much faster than the temperature ones.
- Regarding the amplitude of the neutron noise, the temperature oscillations cause the highest response values. Therefore, in real data, the low transit time observed between upper and lower detectors from the same string can be explained if flow perturbations occur at the core inlet.

### *D3.3 Development of advanced signal processing techniques and evaluation results*

Nevertheless, the high amplitude of the neutron noise below 1 Hz seems to be the result of a temperature perturbation.

Regarding the scenarios with mechanical vibrations:

- In the graph of coherences and phases we can see that in-core and ex-core opposite pairs of detectors show an out-of-phase relationship in the entire frequency range when there are random and sinusoidal vibrations in the fuel assemblies.

- The coherence and the out-of-phase relationship are bigger when the amplitude of the vibrations increases.

- In the cases where the direction of the random vibrations is diagonal (direction XY), we can observe a greater coherence in those couples of sensors whose direction is close to that of the vibration. It can also be observed, that the out-of-phase relationship is clearly seen between pairs of sensors in different halves, but the out-of-phase relationship is somewhat chaotic, with pairs of sensors located transversally to the vibration.

Regarding the scenarios with mixed oscillations:

- When there are sinusoidal vibrations with thermal-hydraulic fluctuations, the reactor is not divided into two out-of-phase halves. But if there are only mechanical vibrations, sinusoidal and random vibrations, the coherence and phase relationships are similar.

- In the APSDs it can be seen that the amplitude of the neutron noise decreases rapidly as the distance from the source of perturbation increases.

- As seen in the simulations, the spectral characteristics cannot be explained by one single phenomenon. It seems that the amplitude of the neutron noise is due to thermal-hydraulic oscillations and that the characteristic out-of-phase relationship in CPSD between opposite detectors is a consequence of fuel assembly vibrations.

The nature of the spectral characteristics observed in the analysis of the neutron noise illustrates the complexity to define the phenomenon and to identify their possible causes, as well as to quantify the relation of each possible cause with the phenomenon itself.



### 3.3 Wavelet transformations

The wavelet transform is a parametric technique that decomposes time-domain signals in time-and-frequency domain features, suitable for further analysis by machine learning methodologies. In the sections that follow, the specifics of the transformation are discussed, along with the selection of the appropriate parameters and hyper-parameters.

#### 3.3.1 Discrete Wavelet Transform

The Discrete Wavelet Transform (DWT) is a processing technique that decomposes a given signal in the time domain to a set of wavelet basis functions which are spatially localized (i.e. only over a part of their length they are non-zero) [ 5 ]. The wavelet functions are dilated, scaled and translated versions of an archetype function called the mother wavelet. The key advantage of the DWT over the Discrete Fourier Transform (DFT) is the property of temporal resolution; that is, its ability to capture both frequency and location information.

DWT is a transformation highly dependent on several parameters and hyperparameters, the most important of which is the chosen mother wavelet. Unlike DFT which analyses a given signal to a summation of sinusoidal functions, DWT refers to a set of different transformations with respect to the chosen mother wavelet. In other words, different mother wavelets, decompose the signal in different ways, so the first step in wavelet analysis is determining the right (optimal) mother wavelet for the signal at hand.

##### 3.3.1.1 Mother wavelet selection

In principal, the optimal mother wavelet should be one whose shape “matches” that of the signal. If this is the case, then large wavelet coefficients will appear at just a few levels (associated with the desired signal), while noise will be evenly spread among all levels ([ 6 ], [ 7 ]). The optimal mother wavelet may be determined according to several criteria; however, the most popular ones are the cross-correlation criterion (derived from the statistical literature) and the energy-to-entropy criterion (derived from the information theory literature) ([ 8 ] – [ 10 ]). The former aims at measuring the similarity between the mother wavelet and the signal. The cross-correlation coefficient  $\gamma$  between signals  $X$  and  $Y$  is calculated according to the Equation below:

$$\gamma(X, Y) = \frac{\sum(X - \bar{X}) \sum(Y - \bar{Y})}{\sqrt{\sum(X - \bar{X})^2 \sum(Y - \bar{Y})^2}} \quad (6)$$

where  $\bar{X}, \bar{Y}$  are the mean values of  $X, Y$ , respectively. This criterion has been run iteratively on over 100 different mother wavelets for all signals in the time domain, both in-core and ex-core. Figure 44 below depicts an example analysis of this criterion. The  $x$ -axis represents the different wavelet families along with their hyperparameters, while the  $y$ -axis represents the value of the cross-correlation coefficient. Different colors are used for the different wavelet families examined.

### D3.3 Development of advanced signal processing techniques and evaluation results

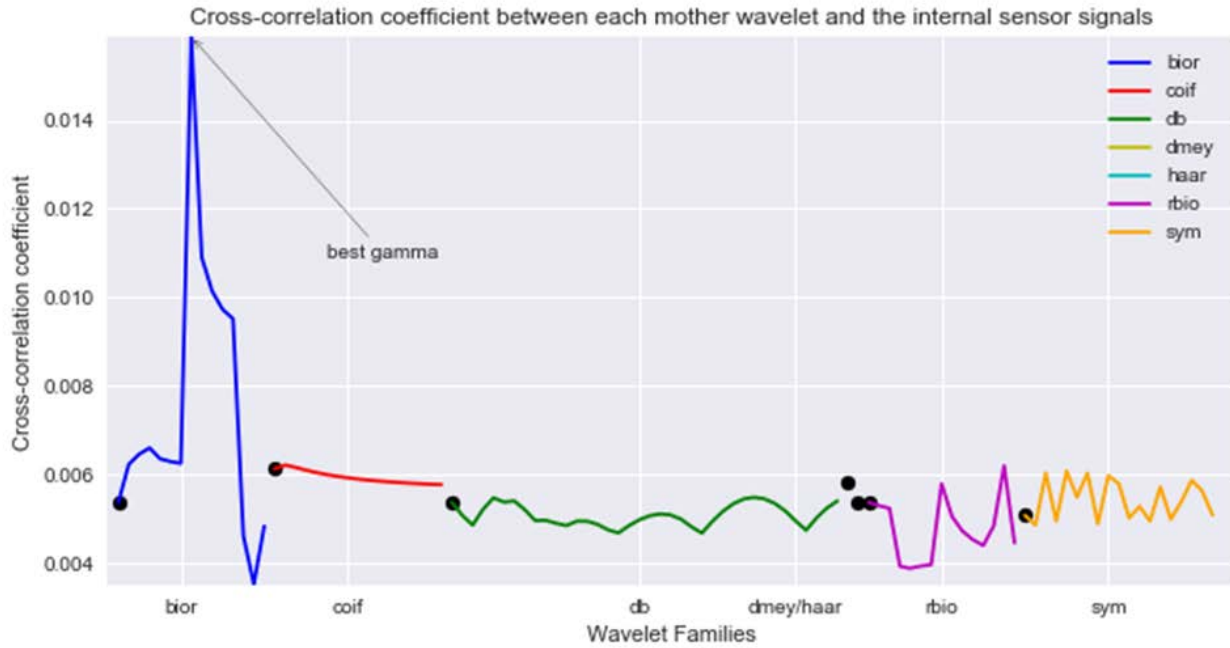


**Figure 44. Optimal mother wavelet selection based on the cross-correlation criterion**

The energy-to-entropy criterion maximizes the ratio of the decomposed signal's energy over its entropy. The energy can be considered as the amount of information carried by the signal coefficients, while (Shannon's) entropy is a measure of uncertainty and produces high values for "noisy" decompositions ([ 8 ], [ 11 ]). This criterion aims at maximizing the amount of energy the wavelet can extract from the signal, while minimizing the entropy of the decomposed signal ([ 10 ]) [6]. The energy and the entropy of the decomposed signal are calculated as follows:

$$Energy(s) = \sqrt{\frac{1}{N} \sum_{i=1}^N s_i^2} \quad (7)$$

$$Entropy(s) = \sum_i (s_i^2 \cdot \log(s_i^2)) \quad (8)$$

where  $s_i$  are the decomposed signal coefficients. The energy-to-entropy ratio is then given by the Equation below:

$$\zeta(s) = \frac{Energy(s)}{Entropy(s)} \quad (9)$$

Like the cross-correlation criterion, energy-to-entropy has been calculated over 100 different mother wavelets for all signals in the time domain, both in-core and ex-core. Figure 45 shows the value of the ratio for an example signal on a number of mother wavelet families. The wavelet exhibiting the highest ratio is the optimal.



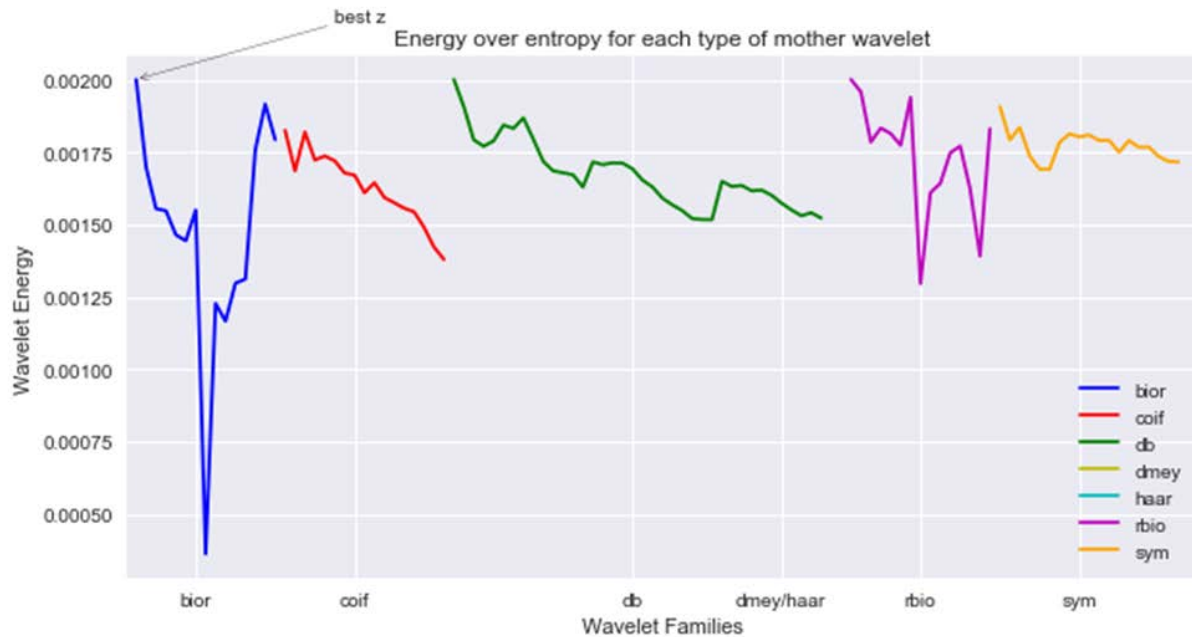


**Figure 45. Optimal mother wavelet selection based on the energy-to-entropy criterion**

### 3.3.1.2 Energy distribution

Having determined the optimal mother wavelet for each signal, the energy distribution of the overall wavelet transform may be computed on the function and wavelet coefficients. Since the wavelet transform is a recursive process, where at each step a detail and an approximation function are computed, it allows us to calculate the energy of the signals at every depth of the procedure ([ 5 ]).

Starting from Figure 46 up to Figure 49 below, the energy of the internal and external detectors of six simulated scenarios of a combined perturbation of a vibrating central cluster of fuel assemblies and a perturbation of thermal-hydraulic parameters are plotted. The  $x$ -axis represents the level of the coefficients and the  $y$ -axis depicts the energy value. D1 are the wavelet coefficients of the first level, D2 of the second and so forth until we finally reach the function coefficients at the last level of analysis (A11 for the 11th level and A9 for the 9th) ([ 5 ]). For each sensor, the optimal mother wavelet chosen according to the respective criterion is different and this is the reason for which, in some scenarios, the depth of analysis differs (e.g. in Scenario 4 of Figure 46, where the level of analysis is 10 and 12).

In Figure 46 and in Figure 47, we observe that it is possible to achieve perturbation identification up to the type and frequency level, but not up to the amplitude level, when the internal detectors alone are considered. For example, Scenarios 1 & 2 (5x5 central FAs, white noise) have distinct energy distributions, when compared to Scenarios 3 & 4 (5x5 central FAs, sinusoidal noise at 1.5 Hz) and Scenarios 5 & 6 (perturbation of thermal-hydraulic parameters). However, Scenario 1 (5x5 central FAs, white noise, 1mm amplitude) and Scenario 2 (5x5 central FAs, white noise, 0.5 mm) have a similar energy distribution, which could make the amplitude of the perturbation harder to detect.

### D3.3 Development of advanced signal processing techniques and evaluation results

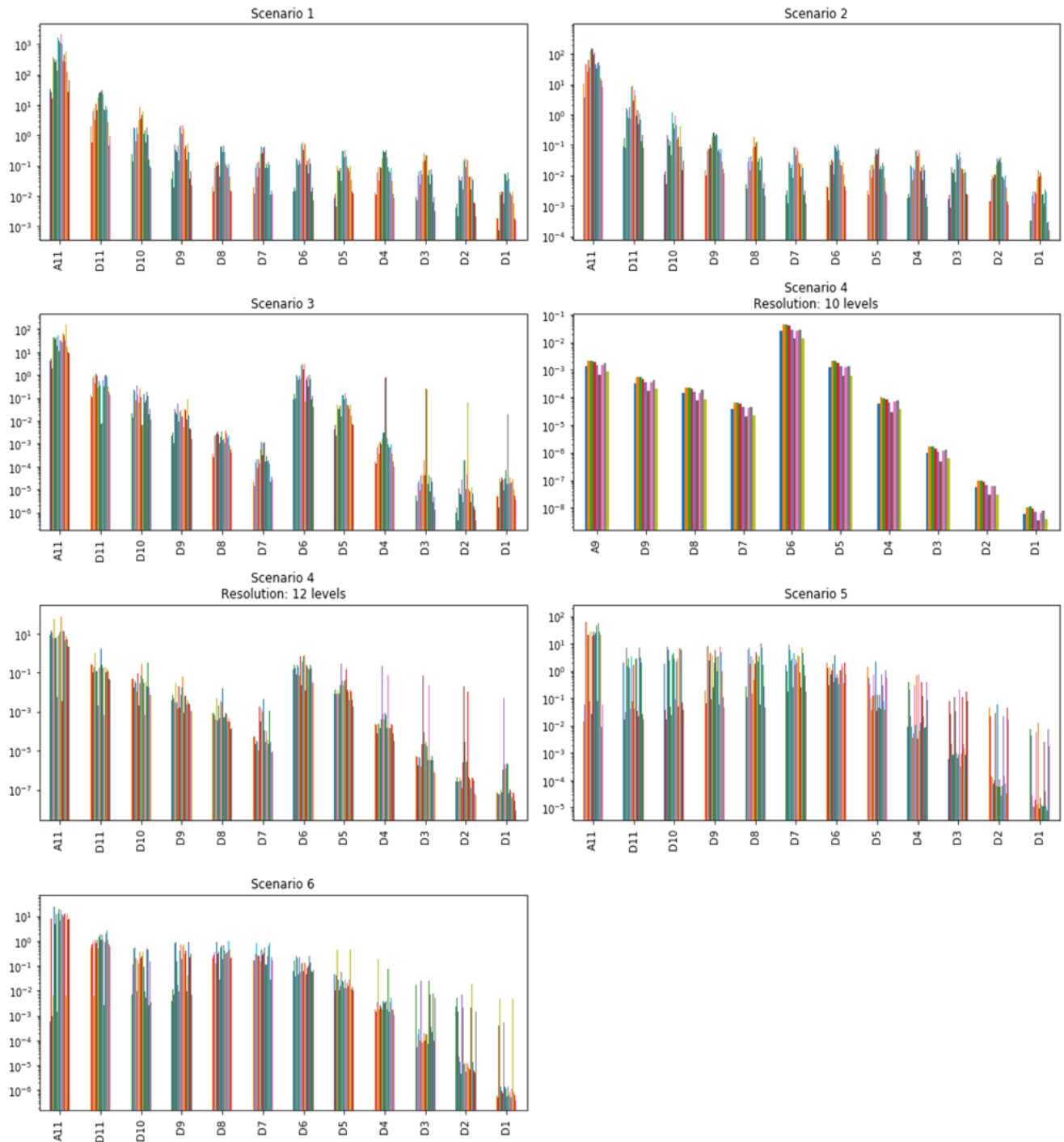


**Figure 46. Energy distribution of Internal Detectors (Energy-to-entropy criterion)**

### D3.3 Development of advanced signal processing techniques and evaluation results

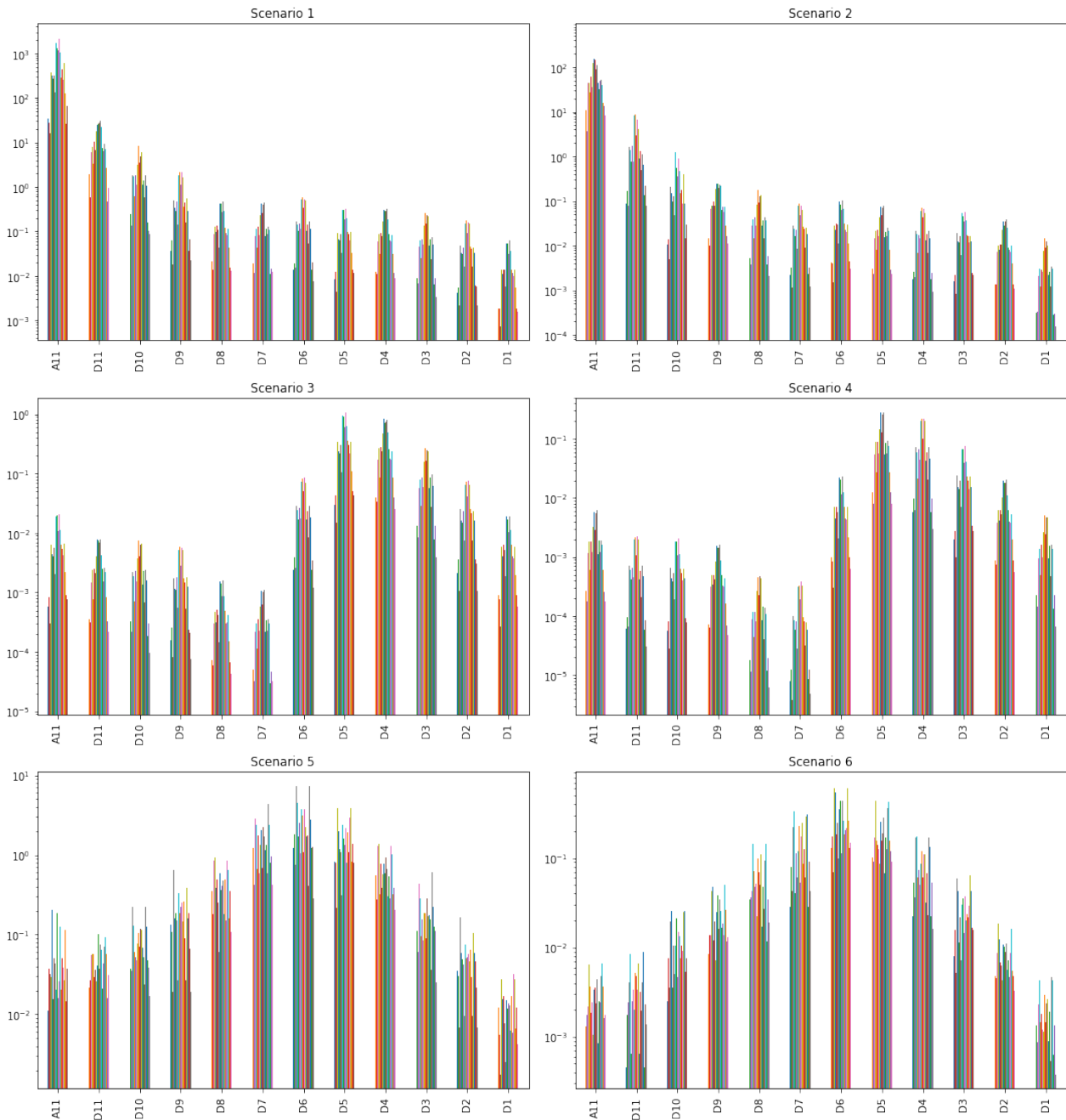


**Figure 47. Energy distribution of Internal Detectors (Cross-correlation criterion)**

### D3.3 Development of advanced signal processing techniques and evaluation results

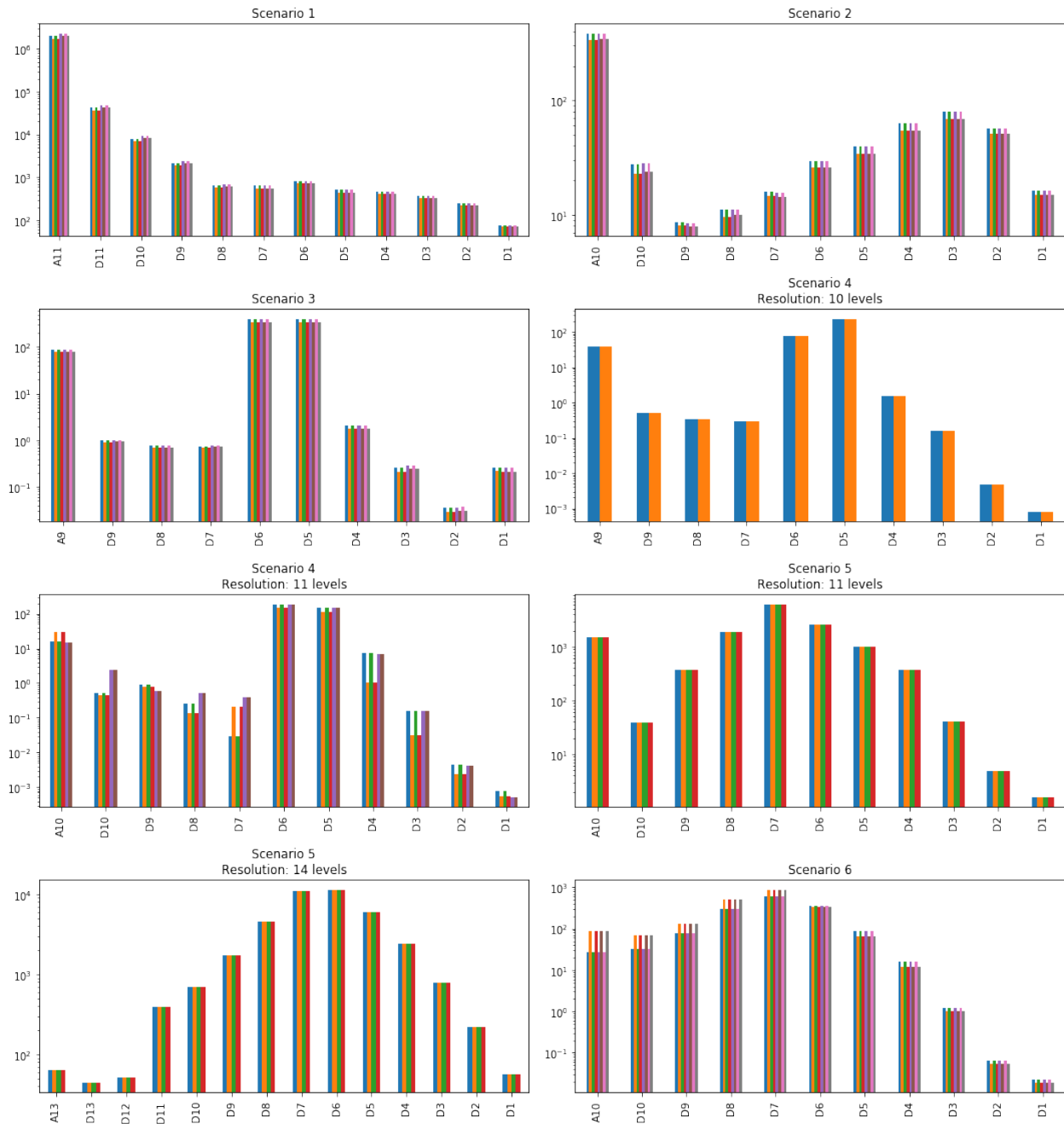


**Figure 48. Energy distribution of External Detectors (Energy-to-entropy criterion)**

### D3.3 Development of advanced signal processing techniques and evaluation results

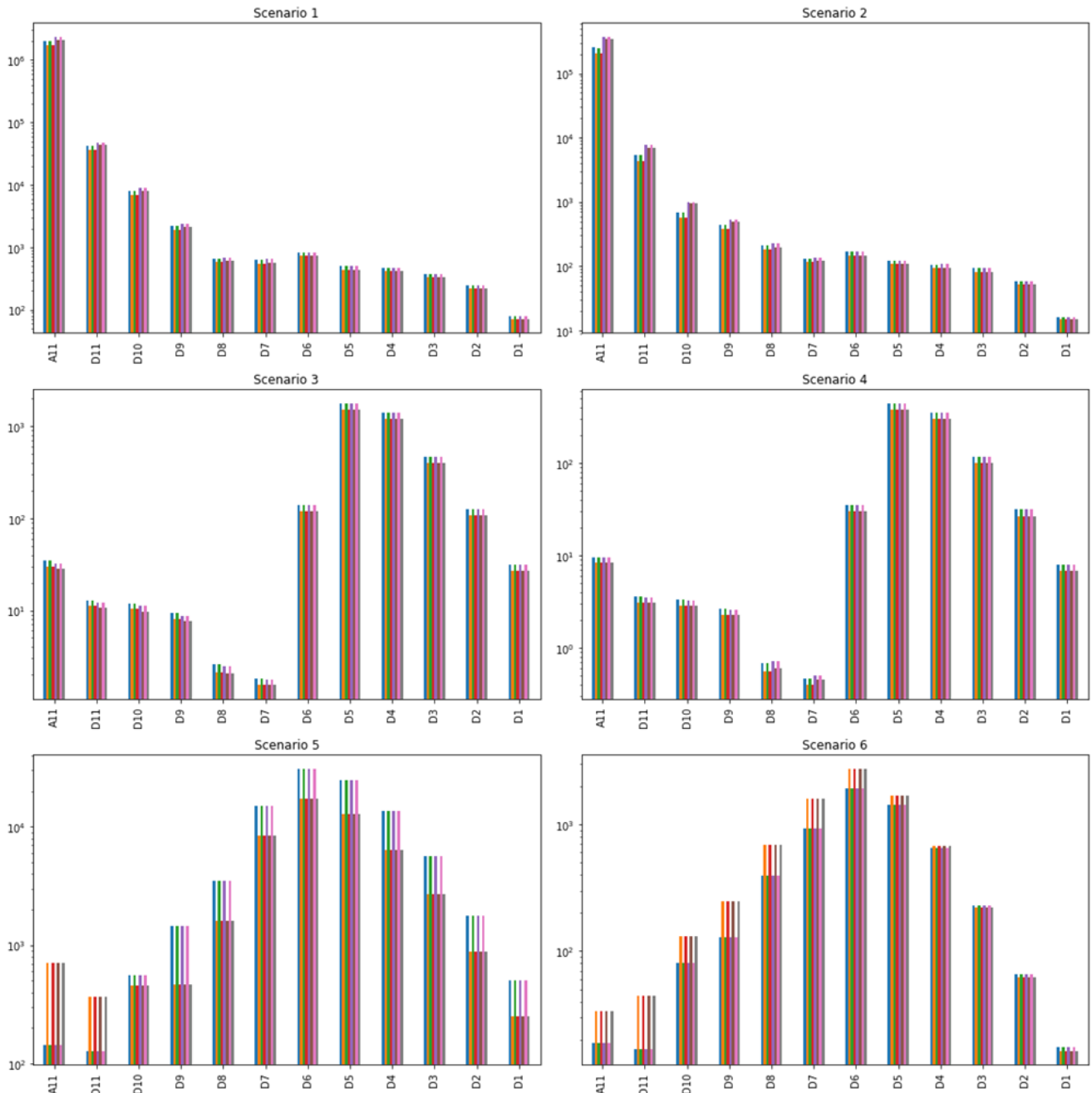


**Figure 49. Energy distribution of External Detectors (Cross-correlation criterion)**

Unlike the case of Internal Detectors, it is possible to achieve perturbation identification on all three levels (Type, Frequency and Amplitude) when the External Detectors are considered, and the energy-to-entropy criterion is used to obtain the optimum mother wavelet. Indeed, in Figure 48, it is evident that the energy distributions are distinctive in all 6 perturbation scenarios, thereby indicating that they could be used as input to a classification algorithm. However, the same cannot be said for the External Detectors when the cross-correlation criterion is used to determine the optimum mother-wavelet, as the energy distributions in this case exhibit a similar behavior to the Internal Detectors case. In conclusion, it could be argued that the energy distributions of the internal and external detector signals under the wavelet transform can be used to safely identify the type and frequency of the perturbations, but not their amplitude.

### 3.3.1.3 Wavelet Spectrum Analysis

A scaleogram is a visual representation of a wavelet transform, having axes for time, scale, and coefficient value, analogous to a spectrogram. Scaleograms visualize the time frequency localization property of the wavelet transform, as seen in the example of Figure 50. In this plot, each coefficient is plotted as a filled rectangle, whose color corresponds to its magnitude. The location and size of each rectangle is related to the time interval and the frequency range of the respective coefficient. Coefficients at low levels are plotted as wide and short rectangles to indicate that they localize a wide time interval but a narrow range of frequencies in the data. In contrast, rectangles for coefficients at high levels are plotted thin and tall to indicate that they localize small time ranges but large frequency ranges in the data. The width of the rectangles drops by approximately a factor of 2 at each subsequent level.

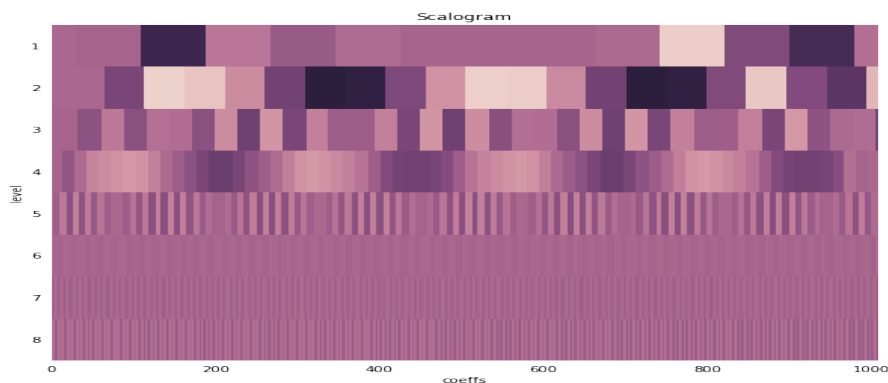


**Figure 50. Scaleogram of wavelet-decomposed signal**

Wavelet scaleograms may be used by machine learning methodologies (such as deep convolutional neural networks) in an effort to efficiently learn to identify features in the time-frequency domain associated with the various perturbation types and, thus, may be able to help distinguish the respective “classes” (types of perturbations). Moreover, this analysis may also serve as an additional fitness criterion of the wavelet decomposition, in addition to the cross-correlation and energy-to-entropy criteria discussed before. This criterion would identify those mother wavelets (along with their respective hyperparameters) that lead to better and more specific representations of the local features of decomposed signals and that could be subsequently captured by the deep convolutional architectures. Finally, we are also examining the possibility of using autoencoders as a means of compressing the information contained in the scaleograms, as suggested in ([ 12 ]).

### 3.3.2 Conclusion

A lot of useful information can be extracted from the input signals through the proper combination of signal processing and wavelet analysis techniques. The goal of this procedure is to use the extracted features to train Machine Learning models for classifying and localizing different types of perturbations that may exist in the reactor and appear in neutron noise measurements. The Discrete Wavelet Transform is deemed to be the proper tool for performing such analysis due to its ability of detecting transients, which are necessary for tasks like anomaly detection. In order to decompose the signal into coefficients that contain useful information, the optimal mother wavelet needs to be firstly selected. This is accomplished through the use of two criteria: energy-to-entropy and cross-correlation. Two distinct types of features are extracted from the coefficients. Their energy distribution per level of decomposition and their scaleograms. The first essentially shows how the signal energy is distributed per frequency band, while the second illustrates the value of the coefficients per decomposition level and time. This illustrates which frequencies are present in the signal at each timestep and is very useful for signals that evolve through time (e.g. if a perturbation begins occurring in the reactor). The scaleograms, which are 2-dimensional images, can be used to train Convolutional Neural Networks for tasks such as perturbation detection, classification and localization.



### **3.4 Plant data processing**

The main goal in this chapter is to show how the joint time frequency method resolves dynamic phenomena in core, where it is necessary to monitor the development of spectral characteristics over time. This is shown on examples of real noise datasets from two power plants - NPP Dukovany and NPP Temelín.

Joint time frequency analysis (JTFA) tools are used for this purpose. Short Time Fourier Transform (STFT) divides the dataset into time intervals and calculates the power spectral density (PSD) at each time interval separately. The type of sliding spectral windows, frequency and time resolutions are the parameters of these calculations. The result is then displayed in 2D or 3D spectrograms using a scale in decibels for the PSD value.

#### **3.4.1 NPP Dukovany**

The Dukovany Nuclear Power Plant located on South Moravia in Czech Republic has 4 PWR reactors of type VVER 440 – Model V 213 with 6 primary circuit loops. Each of these reactors has a heat capacity of 1 375 MW and an electric capacity of 510 MWe. The reactors are fuelled by uranium dioxide  $\text{UO}_2$  enriched by an average of 3.5% of the fission isotope  $\text{U}^{235}$ . Fuel is placed in the reactor in 312 fuel assemblies. Each assembly consists of 126 fuel rods with a hermetically sealed fuel. In addition, the reactor contains 37 control rod assemblies with the fuel part. The coolant flows through the core with 42 000  $\text{m}^3/\text{h}$  at nominal values of inlet and output temperatures of 267,0 °C resp. 297 °C and pressure of 12,25 MPa.

The in-plant operational diagnostic system SPD was delivered by Skoda Nuclear Machinery. For the time being, the diagnostic department of NPP Dukovany operates two basic systems – system for vibration monitoring SMV and loose part monitoring SVC, which constitute the ground of the operational diagnostic system SPD. The system SMV is intended for vibration monitoring of primary circuit components. Monitoring of reactor, main circulating pumps and steam generators vibration is realized by means of sensor set with electronic conditioning and processing computer working in the periodical and operative diagnostics mode. The main part of the system SMV was produced by KWU (absolute and relative displacement, acceleration, pressure pulsation) and the rest (neutron noise) was produced and delivered by UJV Řež. NPP Dukovany measurement UJV data sets are originated from operational diagnostic system SPD with special KWU system SÜS and UJV systems MVI, NNCS, DMTS. The operation analysis of these data sets was done to identify reactor vibration also by means of mathematical models originated from West Bohemian University.

At one of our operational measurement stay in NPP Dukovany we had been observing unusual reactor dynamic behaviour. Measuring instruments of MCP supply current in unit control room exhibited random current fluctuations in 150A range with maximum of 30A amplitude swing instead of the usual 3 – 5 A. The situation from the start of 5th cycle of Unit #4 in October 1992 is illustrated in Figure 51. This state of hydrodynamic instability with a significant beat pattern had operational consequences afterwards, i.e. growth of average reactor output temperature asymmetries and increase of number of thermocouples with these asymmetries in long-term horizon for more than 10 cycles. We have later confirmed that this unacceptable situation started exactly at the above mentioned date (shown in Figure 52).

### D3.3 Development of advanced signal processing techniques and evaluation results



**Figure 51. NPP Dukovany Unit #4 MCP supply current fluctuations**

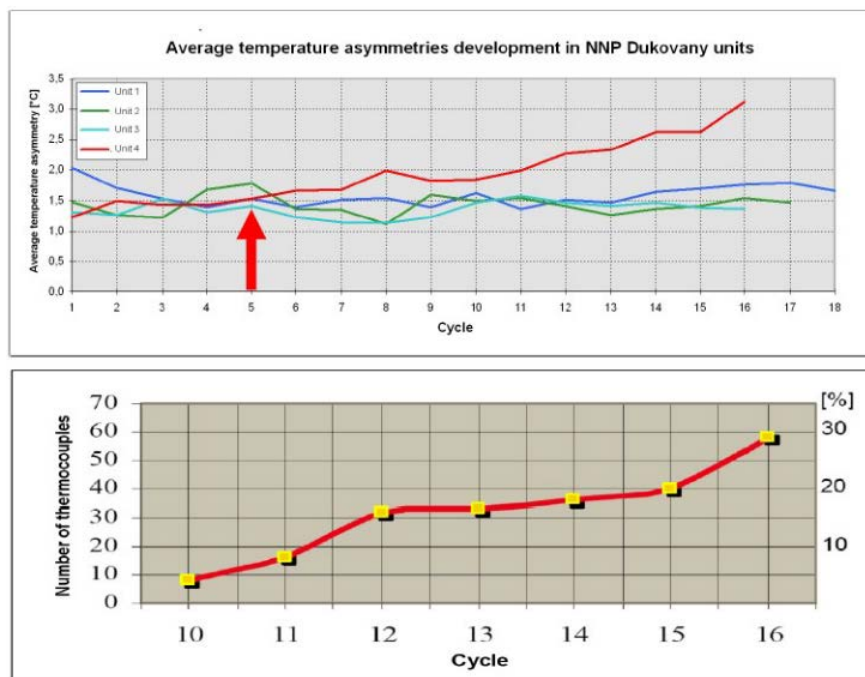


**Figure 52. NPP Dukovany Unit #4 long-term consequences of the fifth cycle**

Based on the visualisation of realized operational measurements, their processing, evaluation and comparison with computational models ([ 16 ]), the origin of that phenomena has become more clear. Different solutions using the measurement of MCP supply electrical current were developed ([ 17 ] – [ 19 ]). As a result, pressure fluctuations with proved dependency on MCP supply current were estimated as the cause of the reactor beat vibrations, which are shown in Figure 53 for the third unit in U3C18 cycle ([ 20 ] – [ 21 ]). However, since we know that the pressure fluctuations are generated on the blades of the MCP impellers, then one of the causality hypotheses of the above described state was an inappropriate combination of MCP impellers. Figure 54 shows the absolute displacement sensor OA3V beat signal at MCP 1st and 2nd revolution harmonics (24Hz, 48Hz) in U430 of the 4th unit NPP Dukovany.

### D3.3 Development of advanced signal processing techniques and evaluation results

It was further confirmed that beat character of pressure and flow oscillations are present in all NPP Dukovany units and are of a dynamic nature during stationary unit operation. Unfortunately, NPP Dukovany cannot confirm these phenomena inside the core, because the power plant does not have in-core noise instrumentation installed as in NPP Temelín. The beat phenomena in ex-core instrumentation are not as apparent as in the NPP Temelín.

Due to the fact that the diagnostic system in NPP Dukovany is currently undergoing reconstruction (including noise in-core instrumentation), such phenomena can be further monitored and evaluated in the future; failures emerging in core may also be the result of an unacceptable operating state in the U4C05 cycle, as described in this section.

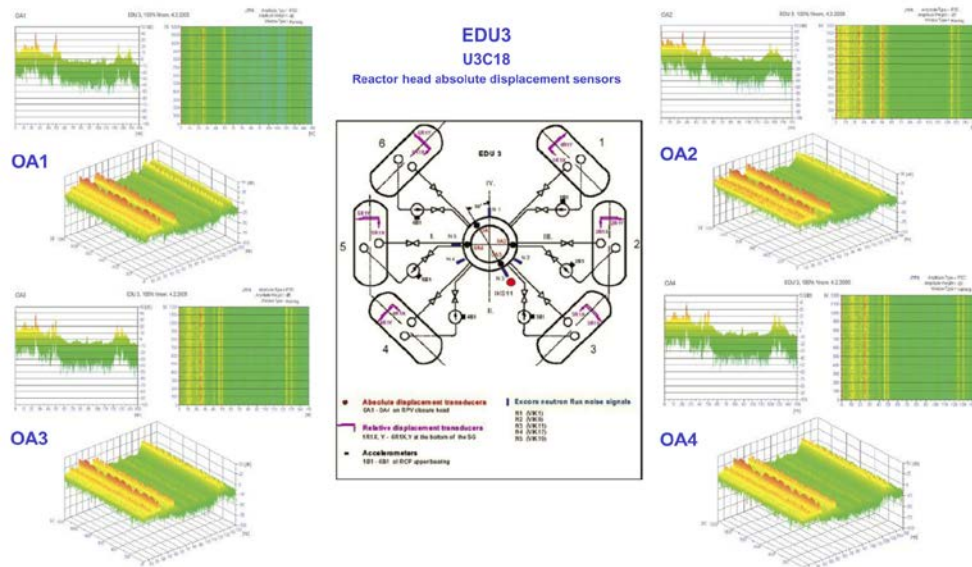


**Figure 53. NPP Dukovany Unit pressure vessel beat frequencies at MCP 1st and 2nd revolution harmonics (24Hz, 48Hz) in U3C18 cycle of the 3<sup>th</sup> unit**

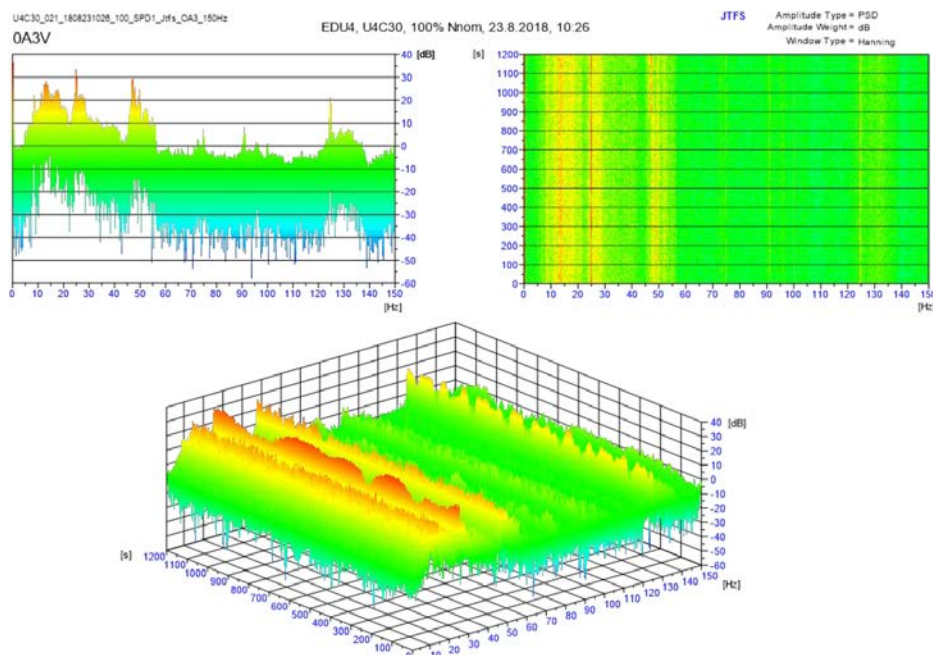


**Figure 54. Absolute displacement sensor OA3V beat signal at MCP 1st and 2nd revolution harmonics (24Hz, 48Hz) in U430 of the 4<sup>th</sup> unit NPP Dukovany**

### 3.4.2 NPP Temelin

The Temelin Nuclear Power Plant is located on South Bohemia in Czech Republic. It has 2 PWR reactors of type VVER 1000 – V 213 with 4 primary circuit loops. Each of these reactors has a heat capacity of 3 120 MW and an electric capacity of 1 026 MWe. The reactors are fuelled by 92t load with uranium dioxide  $\text{UO}_2$  content enriched by an average of 3.5% of the fission isotope  $\text{U}^{235}$ . Fuel is placed in the reactor in 163 fuel assemblies. Each assembly consists of 312 fuel rods with a hermetically sealed fuel. In addition, the reactor contains 61 control rod assemblies. The coolant flows through the core with 84 600  $\text{m}^3/\text{h}$  at nominal values of inlet and output temperatures of 290,0 °C resp. 320 °C and pressure of 15,7 MPa.

The entire primary circuit including the nuclear reactor, four steam-generators, circulation pumps, etc. is located in a fully pressurised reinforced concrete containment facility hermetically enclosed in a protection envelope. In the secondary circuit each steam-generator produces 1,470 tons of steam per hour with an output pressure of 6.3 MPa and temperature 278.5°C. The turbine works at 3,000 revolutions per minute.

The fuel was formerly supplied by the Westinghouse Company (USA), which also supplied the plant instrumentation and control system. Nowadays the fuel is supplied by the Russian company AO TVEL.

Diagnostic sensors of each unit include 4 accelerometers on reactor head flange, 12 ionization chambers placed in three vertical planes at two horizontal levels, more than 256 SPNDs simultaneously scanned in 16 channels groups across the whole core in four axial heights and in not so uniform radial spreading. 5 pressure fluctuation sensors at reactor output and input are available only on the 2<sup>nd</sup> unit.

Noise data have been measured and gathered either with standard Temelin plant diagnostic system RVMS or with UJV mobile in-house systems. RVMS systems of both Temelin NPP units operate periodically across the whole cycle but deliver the results only in the frequency domain. Non-periodic results of UJV mobile in-house systems DMTS and RVDT can be obtained, processed and recorded in the time, frequency and joint time frequency domains ([ 19 ], [ 21 ]). All diagnostic data sets together with records of technological data cover more than 10 fuel cycles in two periods with two different fuel vendors (Westinghouse and TVEL). The whole data pool of diagnostic data parametrized by technological data is concentrated and maintained by the UIZ database developed in UJV.

Measurement of RVMS diagnostic noise data by UJV system DMTS (16 channels, 24-bit resolution – used up to U1C15 cycle) and RVDT (64 channels, 18-bit resolution – used now) depends on the RVMS operation which is determined by settings given in 27 configuration files. Each file contains besides other RVMS operational parameters also a list of 16 SPND sensors which are available at the output of 256/16 switch. All noise diagnostic SPND signals are thus sequentially measured during the day in 18 groups with 16 SPNDs. The diagnostic data are saved with basic fixed frequency ranges 200Hz resp. 300Hz per channel and sampled by minimum 1kHz frequency with 18/24 bits resolution at 5-10V output signal of standard RVMS diagnostic measuring chains. RVMS measuring in-core and ex-core chains separate noise and DC channels and contain conditioning with isolation and buffer amplifiers, high/low-pass 8-pole Butterworth filters with a minimum of 48 dB per Octave roll off to form antialiasing filters in several bandpass ranges.

As in the case of the NPP Dukovany, the pressure fluctuations are also present in the stationary states of NPP Temelín units. They form one of the main parts of the driving forces on reactor internals and fuel assemblies with the dynamic beat character as shown in Figure 55. Beat effects are clearly recognized in the frequency ranges up to 5 Hz, at 6.6 Hz, 9.2 Hz, 13.8 Hz and 16.6 Hz, frequencies with well identified acoustic, mechanical and turbulent flow origin.



### D3.3 Development of advanced signal processing techniques and evaluation results

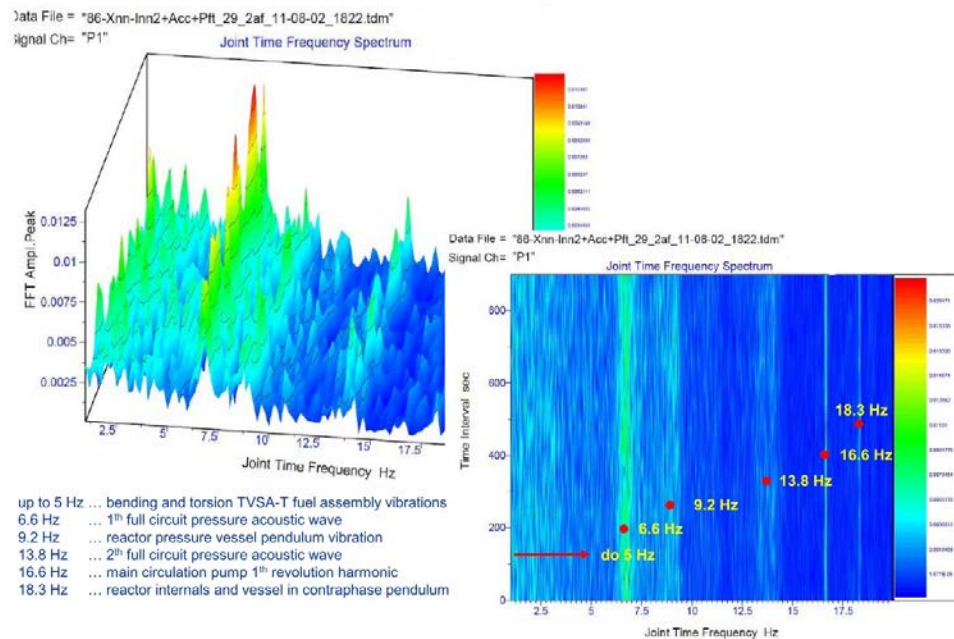


**Figure 55. Beat effects of the 1st loop hot leg pressure fluctuations (NPP Temelin, U2C09)**

Reactor head accelerometer and in-core SPND spectrograms are shown in Figure 56 to give the first preview of differences in dynamic behaviour for fuel assemblies VV6 and TVSA-T from two vendors. Accelerometer A513 and SPND N145 were selected for comparison from the last but one of VV6 fuel load in U1C07 cycle and the first TVSA-T fuel load in U1C09 cycle of NPP Temelín unit #01. Both measurements (10 – 15 min) were realized under the same operational conditions of cycle start-up at physical tests when the strict limitations on reactor stability are laid for calibration of I&C instrumentation. Both sensor sets had the same structure and they were processed up to 150 Hz by the same JTFS programming procedure. The red lines in Figure 56 mark differences in frequency regions.

For reactor head accelerometers (Figure 56) there is clear dissimilarity of beat vibrations in frequency region from the 1<sup>st</sup> to 6<sup>th</sup> MCP harmonic (16,7 – 99,7 Hz). More rigid TVSA-T construction could be the first explanation of shorter beat periods. As seen, the standard PSD spectra do not yield such detailed information. Other existing differences in standard PSD spectra are seen but not as sharply as in the case of joint time frequency spectrograms.

The SPND cluster with investigated N145 in Figure 56 was kept unchanged in the above-mentioned cycles. The characteristic dissimilarities between VV6 and TVSA-T fuel assemblies in head reactor accelerometers spectrograms, SPND spectrograms and PSD spectra are the following

- another frequency region with a shift to higher frequency (30 – 120 Hz)
- more dominant beat character at 120 Hz than at the 6<sup>th</sup> MCP harmonic (99,7Hz)
- further peaks of TVSA-T fuel in 30 – 50 Hz region.

### D3.3 Development of advanced signal processing techniques and evaluation results

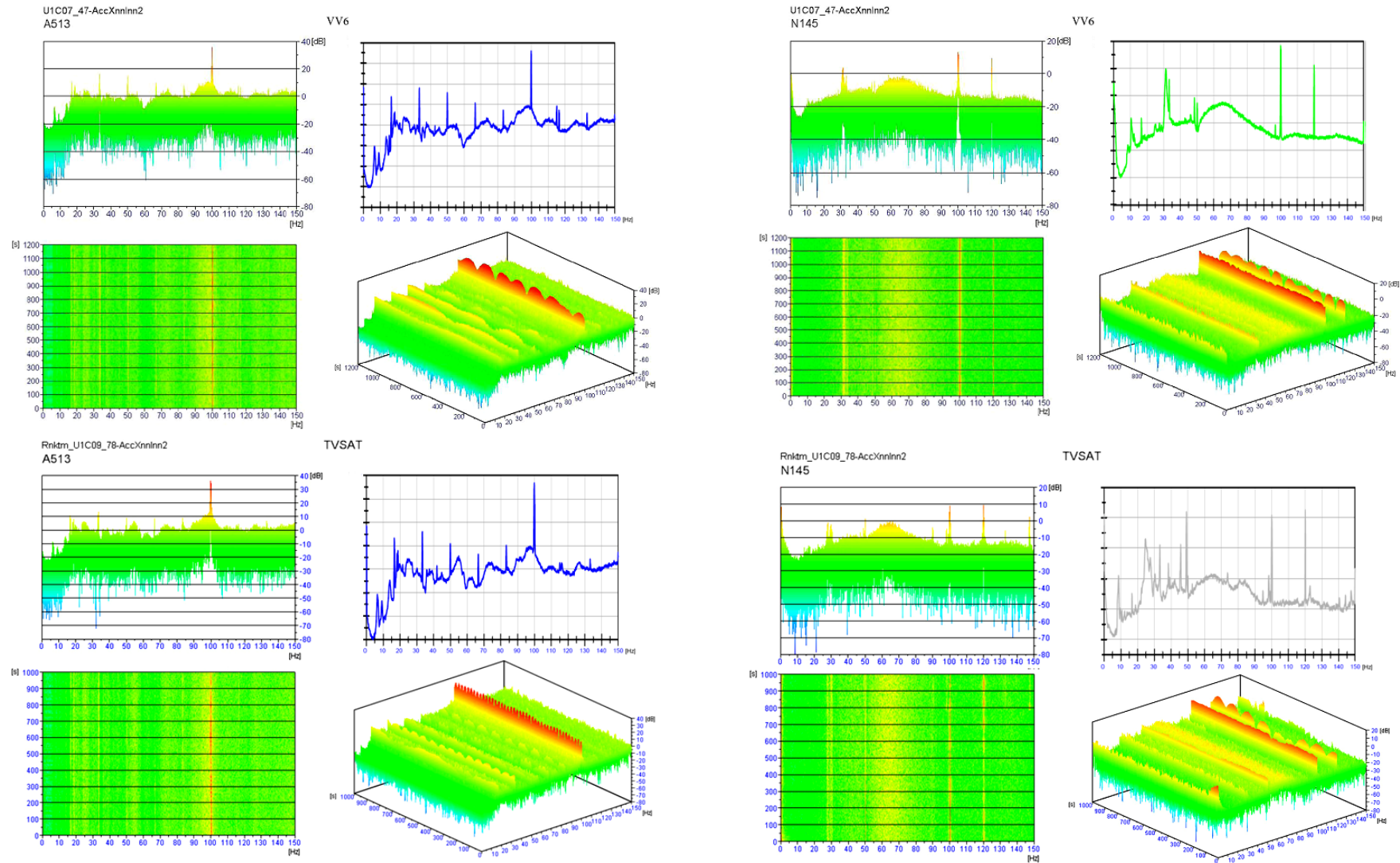


**Figure 56. Unit #01 reactor head accelerometers and in-core SPND spectrograms and PSD spectra of VV6 (U1C07) and TVSAT (U1C09)**



### D3.3 Development of advanced signal processing techniques and evaluation results

To show the relation between pressure vessel movement and fuel assemblies, the CPSDs (amplitude, phase and coherence) of couples of the accelerometer A513 and SPNDs from two upper layers of two adjacent SPND clusters (N075+N077, N145+N147) are presented for VV6 and TVSA-T fuel assemblies. It can be seen that:

- SPNDs of both upper layers 5 and 7 behave in the same manner (particularly with reference to coherence at 9,2 and 33,3 Hz for VV6; 33,3 and 99,7 Hz for TVSA-T)
- SPNDs in two adjacent clusters at zone coordinates 01-34, 02-35 do not behave in the same manner for both fuel loads, although SPNDs in clusters were not changed.

It is worth noting that the above-mentioned relationships are valid for most frequencies with beat character.

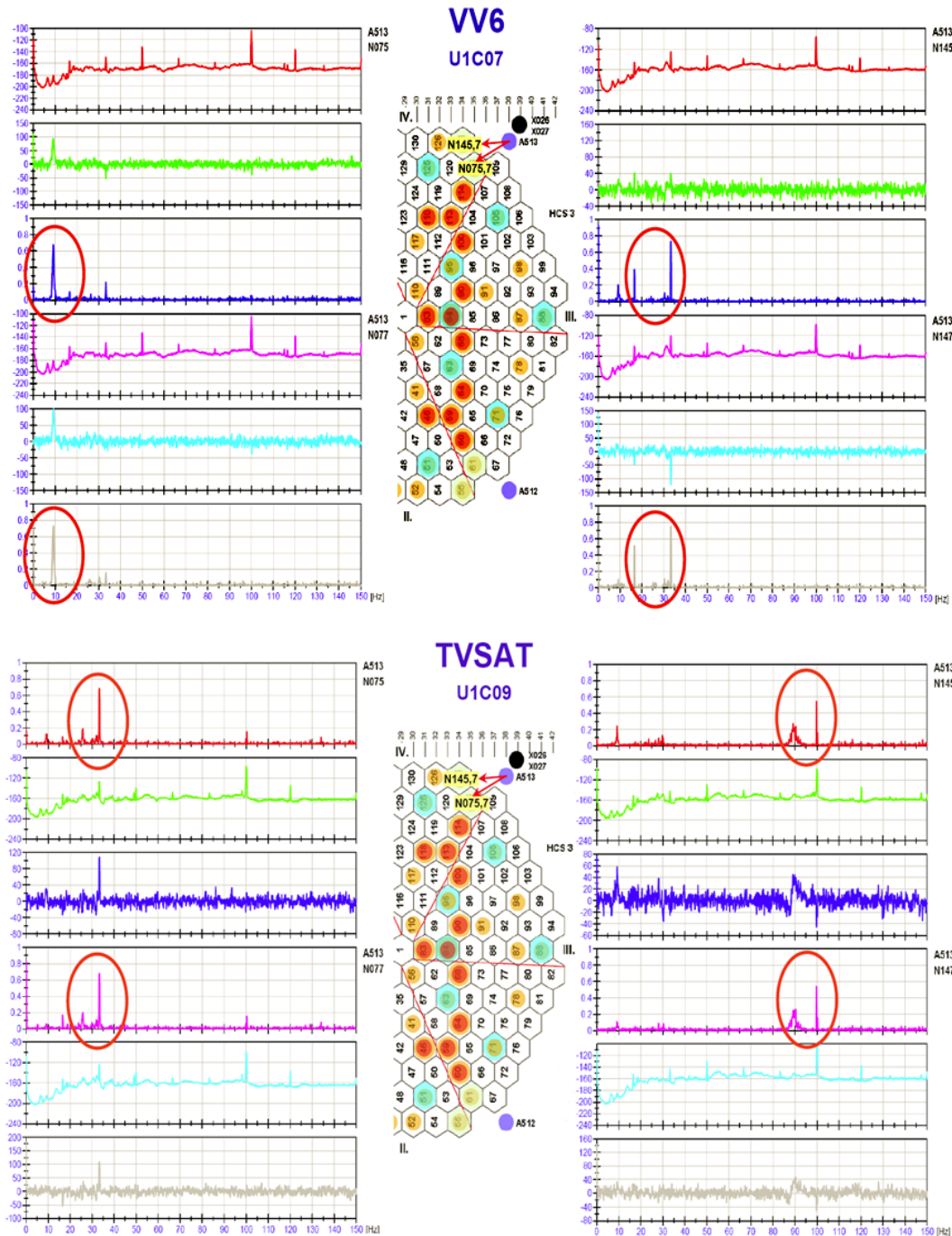


**Figure 57. Beat vibration effects at MCP harmonic frequencies generated by input pressure fluctuations (NPP Temelin, U2C03)**

### 3.4.3 Conclusions

In the described case vibration beats of pressure vessel and fuel assemblies, namely on main circulation pump revolution harmonics, were associated to pressure and flow fluctuations generated by the main circulation pumps with slightly differed revolutions.

Beat vibration effects of NPP Temelin and Dukovany were shown to be common features of dynamic pressure vessel and core behaviour. Also, MCP harmonic frequencies were shown common to both plants and dominating, with beat character representing inconsiderable component in overall reactor and core signal behaviour.

In the investigation of these phenomena, joint time frequency analysis proved to be a useful tool, better distinguishing technological irregularities, anomalies or failures. It provides a quick summary view for classifying and localizing possible perturbations, before using other more complex signal processing methods.

### 3.5 Single Spectrum Analysis

In the following, the Single Spectrum Analysis method (SSA) is considered and its application to acoustic signals from the CABRI facility is demonstrated.

#### 3.5.1 Principles of the SSA method

Consider a real-valued non-zero time series of length  $N$ . The main purpose of SSA is to decompose this time series into a sum of a small number of independent time series representing components of interest and a residual. The SSA technique consists of two complementary stages: decomposition and reconstruction. In this section, we briefly summarize the different steps, for further details on theoretical aspects we report the reader to references ([ 28 ] – [ 29 ]).

##### 3.5.1.1 Decomposition Stage

###### Embedding

Embedding is a classical procedure in time series analysis ([ 30 ] – [ 31 ]). It can be considered as a mapping which transfers the one-dimensional signal into the multidimensional signals  $X_1, \dots, X_k$  where  $X_i = (x_i, \dots, x_{i+L-1})^T \in \mathbb{R}^L$  and  $K = N - L + 1$ . The vectors, called  $L$ -lagged vectors, are grouped into the trajectory matrix

$$X = [X_1, \dots, X_k] = \begin{pmatrix} x_1 & x_2 & \dots & x_k \\ x_2 & x_3 & \dots & x_{k+1} \\ \vdots & \vdots & \ddots & \vdots \\ x_L & x_{L+1} & \dots & x_N \end{pmatrix} \quad (10)$$

This matrix is a Hankel matrix, so all the elements along the diagonal are equal. The single parameter of the embedding step is the window length  $L$  which is an integer such that  $2 \leq L \leq N$ . The SSA technique explores the empirical distribution of the pairwise distances between the lagged vectors  $X_i$  and  $X_j$ . Therefore, the choice of the dimension  $L$  of the lagged vectors is of major importance in SSA implementation, since it determines the quality of the decomposition.

###### Singular Value Decomposition (SVD)

Based on the so-called SVD theorem, the second step of the decomposition stage consists of applying an SVD to the trajectory matrix. Denote by  $\lambda_1, \dots, \lambda_N$  the eigenvalues of the matrix  $XX^T$  following a decreasing order of magnitude ( $\lambda_1 \geq \lambda_2 \geq \dots \geq \lambda_L \geq 0$ ), and by  $U_1, \dots, U_L$  the orthonormal system of the associated eigenvectors. Let  $d = \max \{i \text{ such that } \lambda_i \geq 0\}$ . If we consider  $V_i = X^T U_i / \sqrt{\lambda_i}$  the SVD of the trajectory matrix  $X$  can be then represented as a sum of rank-one bi-orthogonal elementary matrices  $X_i = \sqrt{\lambda_i} U_i V_i^T$ :

$$X = X_1 + \dots + X_d \quad (11)$$

The collection  $(\lambda_i, U_i, V_i)$  is called the  $i^{th}$  eigentriple of the SVD.

##### 3.5.1.2 Reconstruction Stage

###### Grouping

### D3.3 Development of advanced signal processing techniques and evaluation results

The grouping procedure consists of partitioning the set of indices  $\{1 \dots d\}$  into several groups, and in summing the matrices within each group. Considering the group  $I = \{i_1, \dots, i_p\}$  and the associated matrix  $X_I$  defined as  $X_I = X_{i_1}, \dots, X_{i_p}$  the split of the set of indices  $\{I_1, \dots, I_m\}$  leads to the decomposition:

$$X = X_{I_1} + \dots + X_{I_m} \quad (12)$$

The procedure for choosing the set  $\{I_1, \dots, I_m\}$  is called the eigentriple grouping.

#### Diagonal averaging

The last step of SSA transforms each matrix resulting from the grouping stage into a new signal of the same length  $N$  as the initial signal  $x$ , by using the procedure called Hankelization or diagonal averaging. It consists in transforming a given matrix  $X_{I_k}$  into the nearest Hankel one

$\tilde{X}_{I_k} = H(X_{I_k})$  where  $H$  is the Hankel operator. We thus obtain a signal  $\tilde{x}_t^{(k)}$  corresponding to

$\tilde{X}_{I_k}$  of the same length as  $x = (x_1, \dots, x_n)$  such that  $x_t = \sum_{k=1}^m \tilde{x}_t^{(k)}$ :

### 3.5.2 CABRI experiments and the acoustic noise data-processing

The CABRI facility is an experimental pulse nuclear reactor funded by the French Nuclear Safety and Radioprotection Institute (IRSN) and operated by the French Atomic Energy Commission (CEA). It is designed to study the behaviour of fuel rods at high burnup under Reactivity Initiated Accident (R.I.A.) conditions such as a control rod ejection. The distinctive feature of this reactor is its reactivity injection system which is based on the fast depressurization of 96  $^3\text{He}$ -loaded "transient rods" into a discharge tank ( $^3\text{He}$  strong neutron absorber). These transient rods are located in four peripheral core subassemblies. The rapid  $^3\text{He}$  gas depressurization induces a power burst tailorable from 100 kW to 20 GW with a full width at half maximum of 10 to 80 ms. The rapidly-acting Doppler temperature feedback effect inserts negative reactivity, so that the power excursion is quickly turned around. After that, the total energy deposited in the tested fuel (fissile column) located at the centre of the core is limited by dropping the control and shutdown rods into the core. Two microphones are positioned in the test zone, below and above the fissile column, on the test channel wall. They are used to detect clad rupture in the tested fuel rods, as they are sensitive to the acoustic waves produced by mechanical events in the test rod cladding, which propagate through the structure of the test device.

The purpose of the CABRI programs is to study irradiated fuel rod behaviour under Reactivity Initiated Accident (RIA). The test rod is submitted to a power transient (Figure 58) which simulates either sodium vaporization in the core (Fast Breeder Reactor) or the rapid ejection of a control rod.

D3.3 Development of advanced signal processing techniques and evaluation results

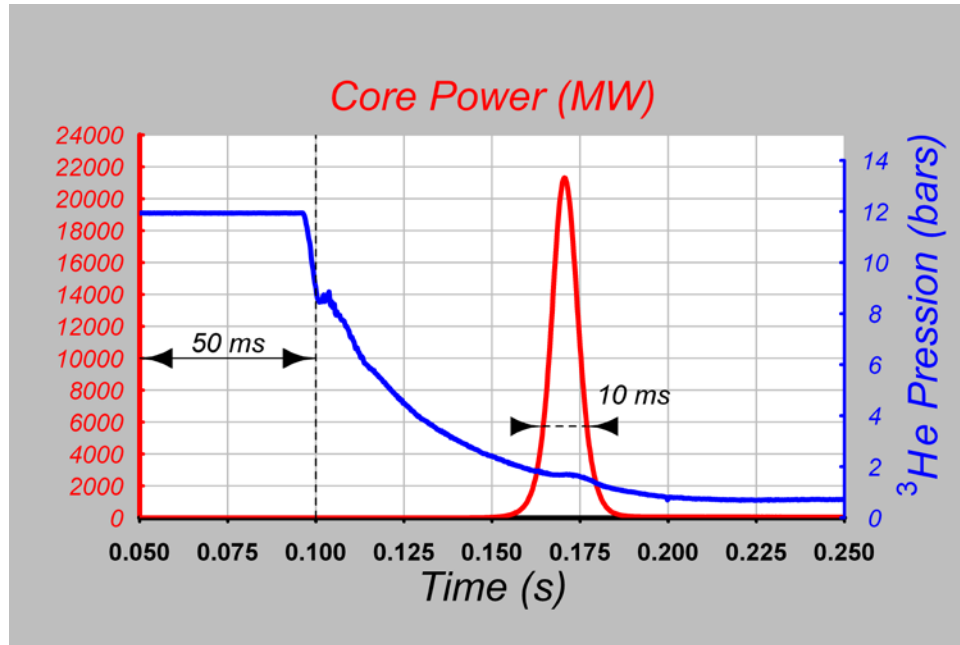


**Figure 58: Core power transient and  $^3\text{He}$  pressure (example of measurements)**

The key feature of the CABRI reactor lies in its reactivity injection system. Four 7-pin-by-7pin driver core subassemblies are replaced by four assemblies called Transient Rods containing gaseous  $^3\text{He}$  initially pressurized from 0 to 15 bars. As  $^3\text{He}$  is a strong neutron absorber, the rapid depressurization into a separate vacuum tank by fast opening valves causes a very fast reactivity injection into the core (Figure 59). The reactivity Doppler effect in the core quickly turns around the power surge.

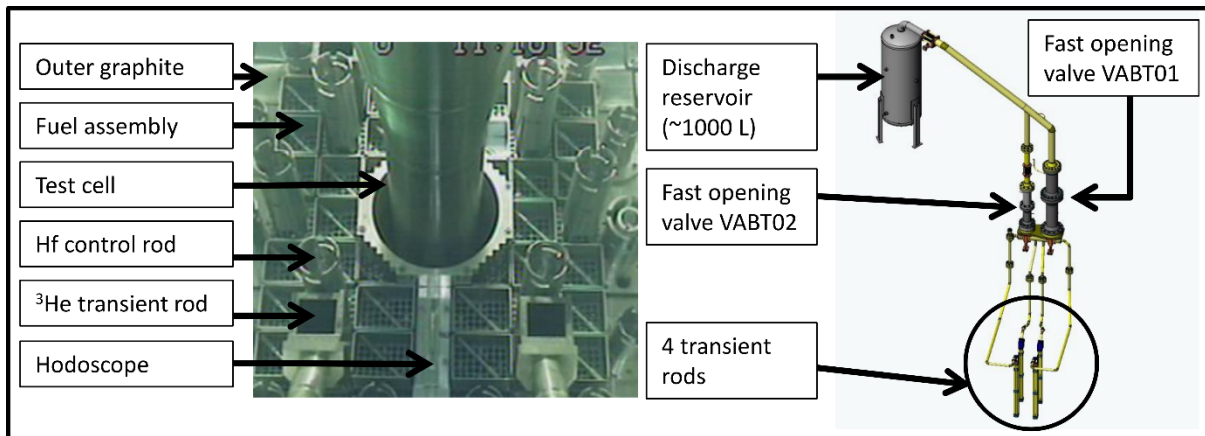


**Figure 59: CABRI core and Transient Rods system**

Two microphones are located in the test device of the facility and record acoustic signals, as represented in Figure 60.

### D3.3 Development of advanced signal processing techniques and evaluation results

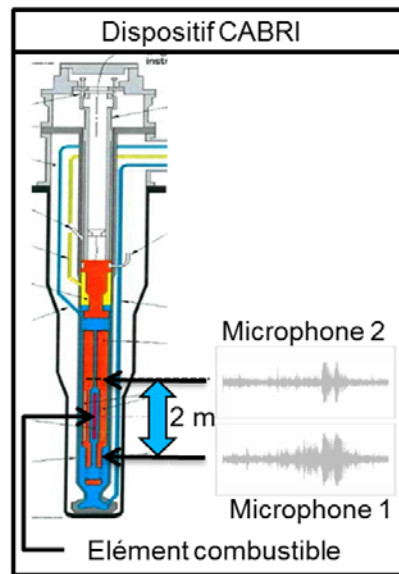


**Figure 60: Location of the two piezoelectric sensors in the test device**

For instance, Figure 61 shows the signals recorded by the microphones M1 and M2 for tests where there was a clad rupture during the RIA experiment; data come from the studies carried out on the last fourteen tests in Figure 61 [ 24 ]. The signals are acquired over a duration of about one second, i.e., the duration of an experiment. Table 12 gives the sampling rate for every test.

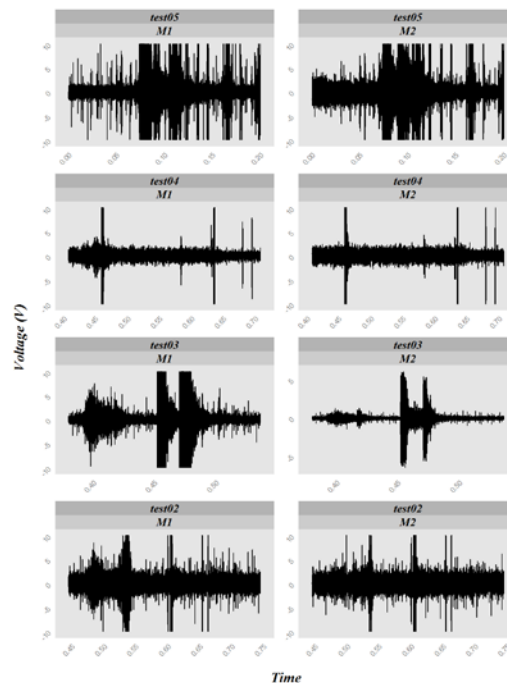


**Figure 61: Overview of the two microphones (M1 and M2) signals for every test. There is a clad rupture in every test**



**Table 12: Sample rates for every test**

<b>Test Name</b>	<b>Sampling Rate (<math>\mu s</math>)</b>
Test02	2.5
Test03	2.5
Test04	5
Test05	2.5

The signals have to be processed to extract useful information from them. Firstly, the background noise has to be analyzed in order to eliminate it [ 25 ]. The data acquisition starts a while before the actual RIA experiment, so some knowledge of the background noise alone is available. Very good results have been obtained using the spectral subtraction methodology [ 26 ].

In spectral subtraction, an estimate of the spectral amplitude of the signal is obtained by subtracting an estimate of the spectral amplitude of noise from that of the noisy signal. In spectral subtraction, the incoming signal  $x(m)$  is divided into frames of  $L$  samples length. Each frame is windowed, using a window (e.g. Hamming) and then transformed via Discrete Fourier Transform. In the spectral domain we do the difference of the module, keeping the phase of the raw signal. The parameter  $\alpha$  controls the amount of noise subtracted from the noisy signal (Eq. 1). Then, we transform this new spectrum into the time domain via the inverse discrete Fourier transform.

In time domain:

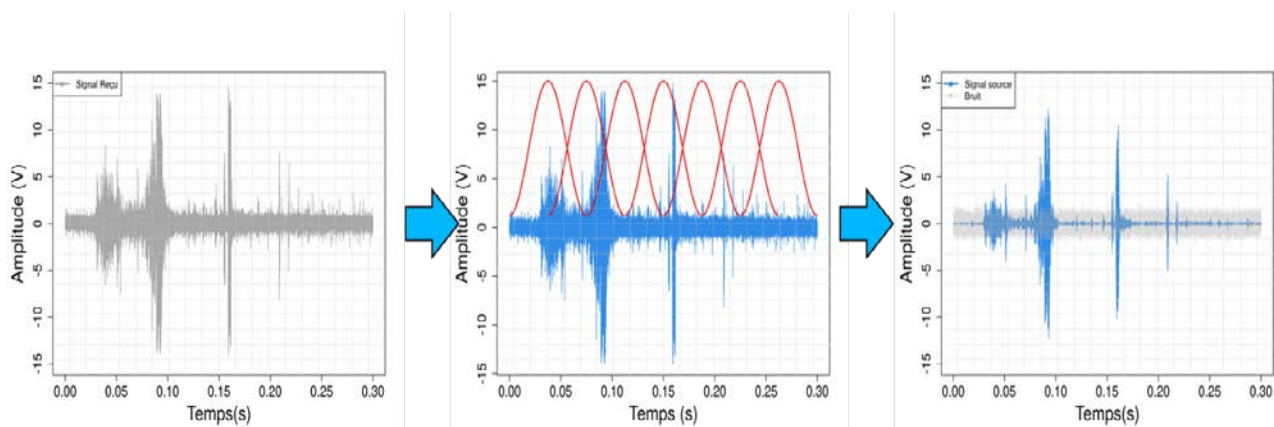
$$x(m) = s(m) + n(m) \quad (13)$$

with:  $x(m)$  raw signal,  $s(m)$  denoised signal,  
 $n(m)$  noise

In frequency domain:

$$X(f) = S(f) + N(f)$$

$$\hat{S}(f) = [|X(f)| - \alpha \cdot |N(f)|] e^{i\theta_x(f)}$$



To evaluate the quality of the subtraction, we use the Signal to Noise Ratio (SNR) vs the correlation coefficient in the time domain and the Kullback-Leiber indice in the frequency domain. We choose a trade-off according to different values for the window size and  $\alpha$  (Figure 62).

### D3.3 Development of advanced signal processing techniques and evaluation results

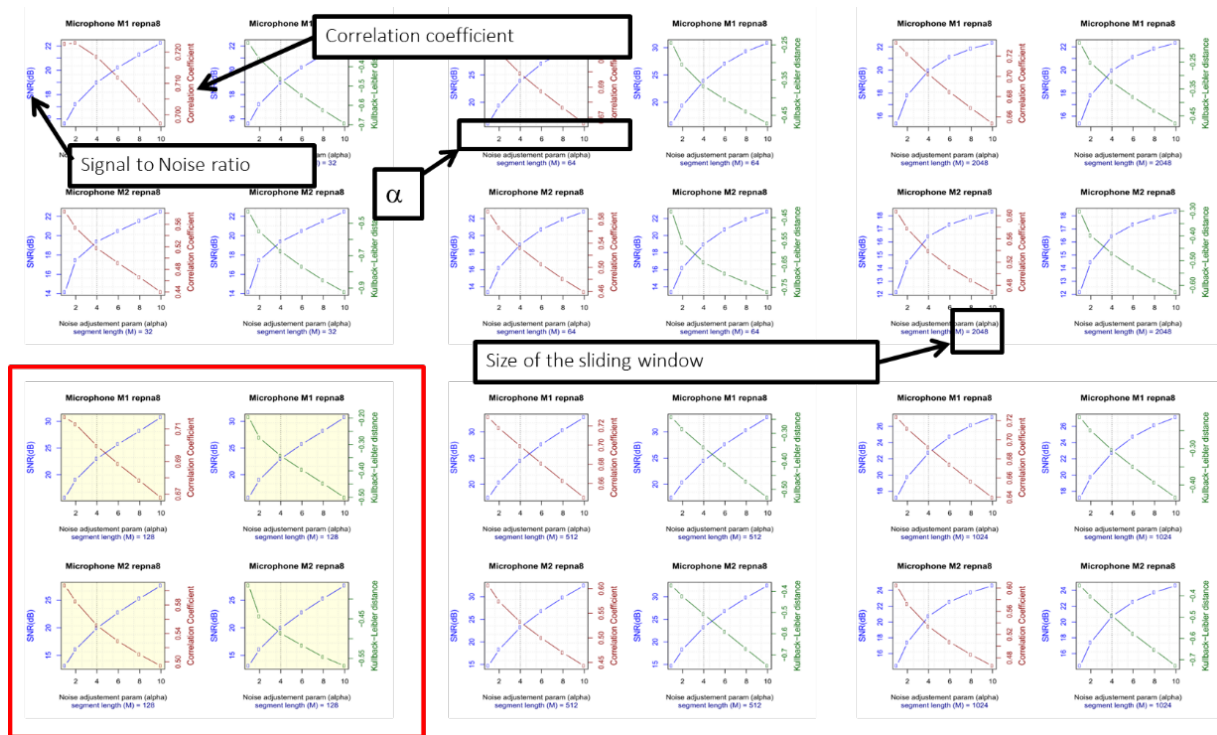


**Figure 62: Strategy to choose the window size for the spectral subtraction calculation for different values of the  $\alpha$  parameter and the SNR**

Sometimes, it is not possible to do specific assumptions on the stochastic behaviour of noise. So, the Singular Spectral Analysis (SSA) has been used on the data [ 27 ]. The SSA needs no statistical assumption on signal, or noise. By using a decomposition of the signal into the sum of a small number of orthogonal components, SSA allows to perform various tasks such as extraction of specific components from a complex signal (noise, trend, seasonality), detection of structural changes and missing values imputation.

#### 3.5.3 Conclusions

The SSA methodology is a powerful technique, as demonstrated in the analysis of acoustic signals in the CABRI reactor. In the future, we plan to apply the SSA methodology on real neutron noise signals as well. In some preliminary investigations, we have tested the classical SSA method on neutron noise data. We have shown how the method works on a simulated data set provided by PSI. Then we have applied the method on actual data provided by UJV (WWER 1000/320 reactor). We chose to analyse the axial locations of the Self Power Neutron Detectors in string N31. We observed that the SSA can be used to improve dramatically the frequency resolution. We will continue applying the method on the other strings.

## 4 Reconstructing data

This section is devoted to a relatively new methodology of reconstructing correlated signals like in or ex-core neutron measurements. The first subsection 4.1 explains why we need to reconstruct signals. The second subsection 4.2 summarises basic assumptions of the signal reconstruction and methods of use. The third and fourth subsections 4.3 and 4.4 are devoted to the reconstruction algorithm. The practical examples show, how it is used for diagnosis of bad (incorrect) data or how to add missing data (fill gaps in data). The fifth subsection 4.5 summarises results of the described methodology on PSI simulated and NPP reactor data.

### 4.1 Purpose of reconstruction

Via comparison of original signal and its reconstruction one can distinguish between correct and incorrect (valid and invalid) signal measurements. Increased deviations between measurement and reconstruction can also be indicators of various phenomena. As an example, increased deviations in the 7<sup>th</sup> layer of VVER-1000 reactors usually indicate control rod movability tests, that are regularly performed on this type of the reactor.

Reconstruction is thus a useful diagnostic method, which:

- (a) helps in diagnosing reactor performance,
- (b) prevents false conclusions in case of incorrect measurements, that sometime occur even in records of reputable companies,
- (c) allows to fill in potential gaps in data (missing data) or to replace invalid data with correct estimates from other measurements.

Reconstruction of reactor signals is described in literature [ 24 ], [ 29 ]; it can be used as pre-processing step, assuring that only correct data are used for training e.g. neural networks.

### 4.2 Reconstruction assumptions

When reconstructing signals, the following hypothesis are assumed.

1. Reconstruction is only possible in frame of one fuel cycle. The estimates of bad or missing SPND signals do not hold in following or preceding cycles.
2. For the reconstruction it is necessary to have at least some valid SPND data, which we want to reconstruct. The more valid data is available, the more precise is the reconstruction. Valid data should fulfil validation criteria. The latter have to be developed individually for each reactor and SPND instrumentation type. Examples of valid and invalid data usable for reconstruction are given in Figure 63 – Figure 65.
3. There are three types of reconstruction, depending on the direction of reconstruction. If we have valid data of some SPND at the beginning of fuel cycle and then we lose the signal, or signal starts to be invalid, we perform **forward** reconstruction. On the contrary, if we only have some valid data at the end of fuel cycle and we reconstruct data from the beginning of fuel cycle to the beginning of valid data, we perform **backward** reconstruction. If we only have some valid data somewhere in the middle of the fuel cycle and we reconstruct both past and future date, we perform backward and forward reconstruction. All three possibilities were successfully tested on VVER-1000 data.

### 4.3 Reconstruction algorithm

The reconstruction algorithm is detailed hereafter.

1. Define the valid data interval for the SPND signal that you want to reconstruct.
2. Order valid SPND measurements based on the distance from the reconstructed one (order all SPNDs and exclude those with invalid measurements). Select  $m$  closest measurements ( $m = 10$  suits well for VVER-1000).

3. Apply linear regression model on the problem in the following form:

$$N_r = c_1 N_1 + c_2 N_2 + \dots c_m N_m$$

where  $N_r$  is the reconstructed SPND signal,

$N_1$  is the SPND valid signal of the closest SPND to reconstructed SPND

$N_2$  is the SPND valid signal of the second closest SPND to reconstructed SPND

...

$N_m$  is the SPND valid signal of the m-th closest SPND to reconstructed SPND.

Using least squares minimization calculate the coefficients  $c_i$ ,  $i = 1, 2, \dots m$ . The number  $m$  of SPNDs suitable for reconstruction depends on the overall valid measurements that are available. For the VVER-1000 with 64 strings, 7 SPND each, suitable value of  $m$  is 10 (empirically selected).

4. Reconstruction of the missing, or bad data, as a linear combination of valid measurements in the vicinity, using coefficients calculated in the previous step.

Experience with different data showed, that this algorithm can be modified according to data available. In case of Gösgen NPP data we came to the conclusion that concerning the in-core data, instead of the 10 closest SPND data we can preferably use five remaining SPNDs of the same string (Konvoi reactors use SPND strings with 6 SPND each). As for ex-core data, optimal solution was to reconstruct each ex-core measurement using seven remaining signals (there are eight ex-core measurements). This modification is also suitable for VVER-1000 ex-core measurements. As proved on PSI simulated signals, ex-core measurements can also be reconstructed by in-core measurements, but we cannot recommend it for real data due to different responses of ex-core and in-core detectors. The ex-core detectors (ionization chambers) react much faster to neutron flux changes and thus we receive big errors in fast transient reconstructions.

## 4.4 Details of the algorithm and examples of its use

### 4.4.1 Definition of valid data interval

Definition of valid data interval is illustrated in the two following figures. The first (Figure 63) shows the SPND failure due to penetration of water into the tube, holding and protecting the SPNDs:

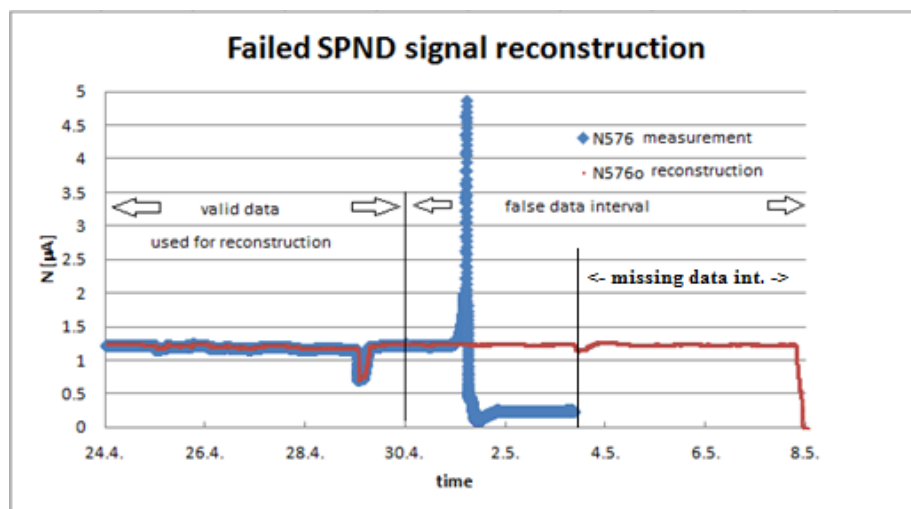
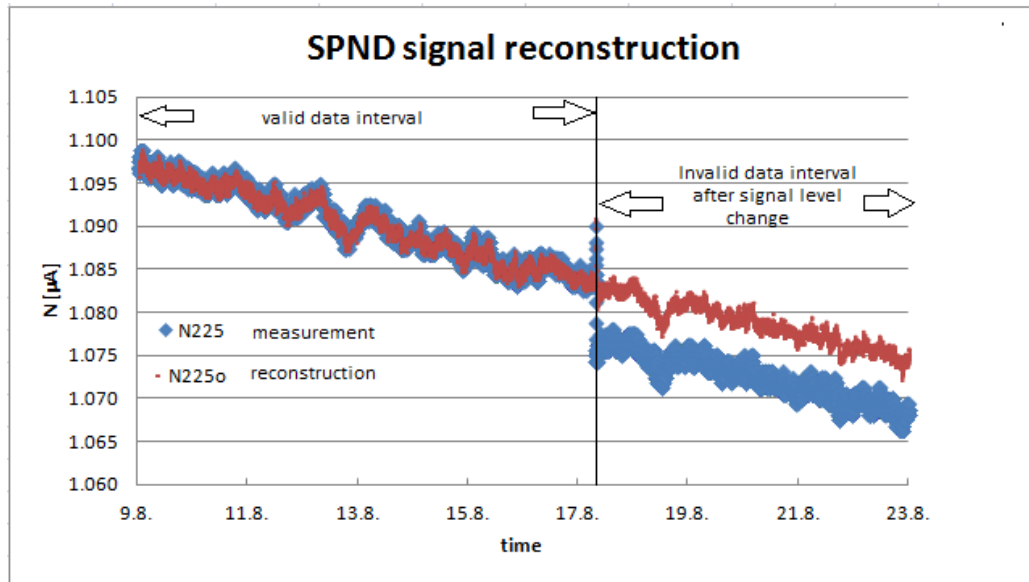


Figure 63: Example of SPND failure and reconstruction of its data

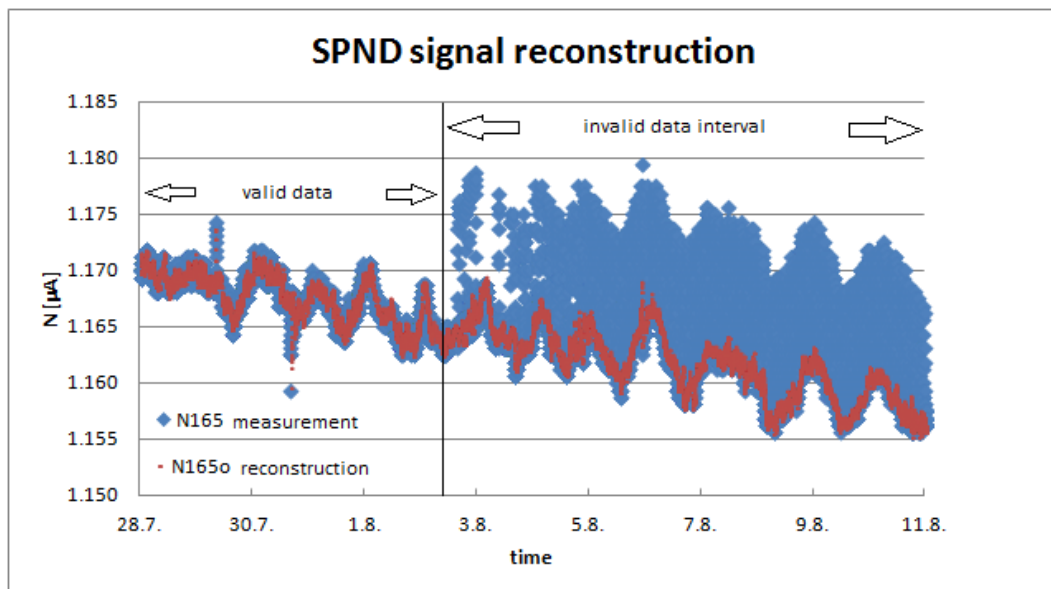
### D3.3 Development of advanced signal processing techniques and evaluation results

Figure 64 explains the valid data interval selection in case of signal level change - which sometimes occurs due to faults of electronic circuits - evaluating the SPND signal:



**Figure 64: Example of SPND signal level change and corresponding invalid data reconstruction**

Figure 65 shows large one side deviations, which sometimes corrupt the SPND signal:



**Figure 65: Example of SPND one side deviations and corresponding invalid data reconstruction**

#### 4.4.2 Ordering SPNDs according to their distances

Selection of the nearest (closest) SPND to the selected SPND can easily be done in Excel or another spread sheet environment. First it is necessary to create the matrix of distances between SPNDs.

If we have available the map of strings in the core, the fuel dimensions and the distance between SPND layers, we can define their mutual distances as the square root of sum of squares of x,y,z ordinates differences. The list of the closest SPND in the vicinity can easily be obtained through ordering the data (ordering the SPND distances from the highest to the smallest one).

#### 4.4.3 Calculation of reconstruction coefficients

Coefficient calculation can be performed, using the Excel function LINREGRESE, with parameters Bi:Bj;Ci:Lj;FALSE where:

Bi:Bj are data of the reconstructed SPND,

Ci:Lj are data of SPNDs in the vicinity,

FALSE is a constant parameter, indicating that there is no constant parameter in the linear regression model.

The function LINREGRESE returns the field of coefficients, which minimize the sum of deviation squares in reverse order, i.e., the first resulting coefficient belongs to the last SPND in the input list.

### 4.5 Reconstruction results

Two types of data were reconstructed – simulated data from PSI and measured data from NPP Gösgen.

#### 4.5.1 Reconstruction of PSI simulated data

##### Simulation E4\_11rnd

These data simulate random vibrations of fuel assembly E4 in a time interval with length 45 sec and time step 0,01 sec. Reconstruction coefficients were calculated from first 10 seconds (first 1000 records). Detailed description of the simulation can be found in [ 35 ].

Differences between simulation and its reconstruction were very low, usually of the order  $10^{-6}$ . The only exception were the first records of O5Lv3 and N12Lv2 sensors, as illustrated in the next Figure:

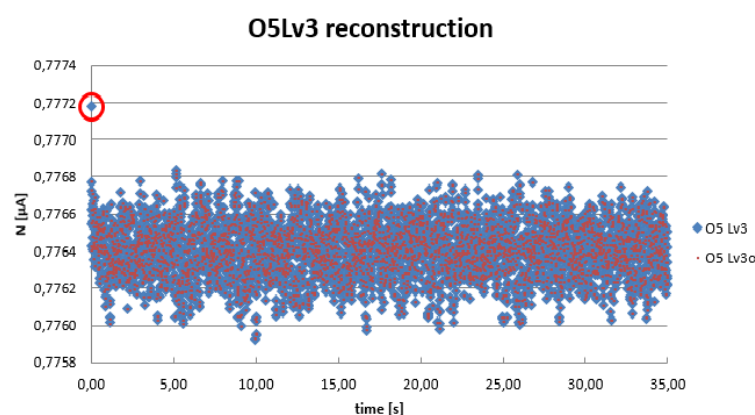


**Figure 66: Simulated O5Lv3 random signal and its reconstruction**

It can be concluded that, for neural network training purposes, bad records of simulated signals O5Lv3 and N12Lv2 should be deleted.



### Simulation E4\_11sine

These data simulate sinusoidal vibrations of fuel assembly E4 in a time interval with length 45 sec and time step 0,01 sec. Vibration amplitude is 1.1mm with frequency 1.5 Hz. Reconstruction coefficients were calculated from the first 10 seconds (the first 1000 records). Detailed description of the simulation can be found in [ 35 ].

Differences between simulation and its reconstruction were very low, usually of the order  $10^{-6}$ . The exceptions were the first and last records of O5Lv3 and N12Lv2 sensors, as illustrated on next figure:

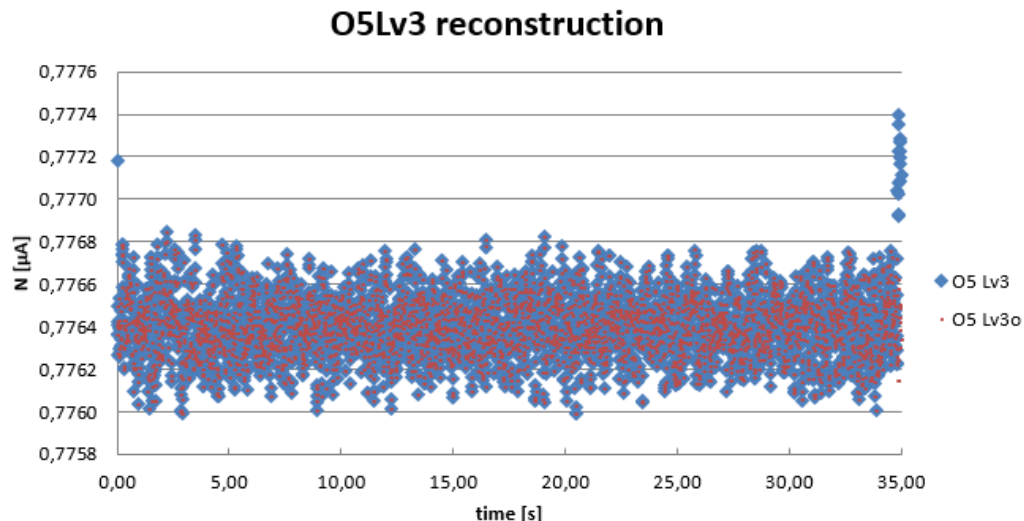


**Figure 67: Simulated O5Lv3 sinusoidal signal and its reconstruction**

The problem in these cases is not the increased deviation of the signal, but the fact that the response to sinusoidal excitations of one fuel assembly in linear systems should be also sinusoidal; this can be seen in scenarios 2019-05-Dataset7-C03,04 (version 10), where all responses to sinusoidal excitation are almost exactly sinusoidal – see following examples:

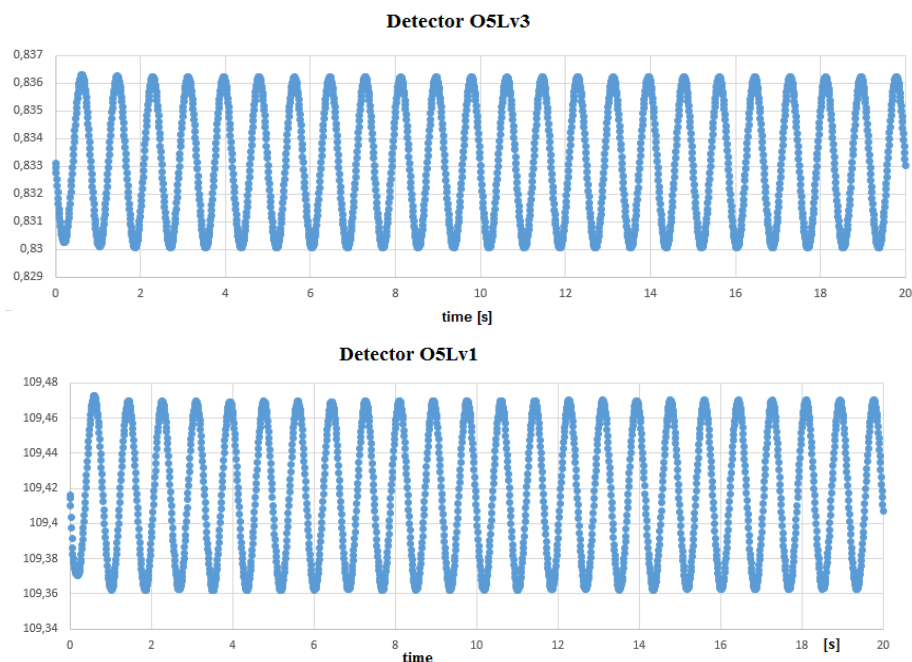


**Figure 68: Simulated O5Lv1, O5Lv3 signals in 2019-05-Dataset7-C03-FA1-SIN-1.2Hz-1mm-1**

### Vibrating FA 10-7, white noise, amplitude 1,1 mm

These data simulate random vibrations of fuel assembly 10-7 in a time interval with length 45 sec and time step 0,01 sec. Reconstruction coefficients were calculated from first 10 seconds (first 1000 records). Detailed description of the simulation can be also found in [ 35 ].

Differences between simulation and its reconstruction were very low of the order  $10^{-6}$  without any exception.

### 4.5.2 Reconstruction of NPP Gösgen data

#### Gösgen data EOC 39

These data are from the end of Gösgen fuel cycle 39, as described in detail in [ 33 ]. The results of the reconstruction are summarised in Annex 8.5.

Interesting results were obtained, most notably:

- The identification of defective in-core neutron flux measurements: L-N08-2 and L-N08-4 (in accordance with [ 33 ]).

Moreover, new results ( not reported in [ 33 ] ) were obtained:

- L-J14-1 also represents a defective measurement, because it is constant (frozen value).

L-J06-2 is partially defective, as is illustrated in the following two Figures. At first, the signal from time 0 to 376 sec is invalid, then from time 376 sec to time 2870 sec follows valid data and at the end it is also invalid:

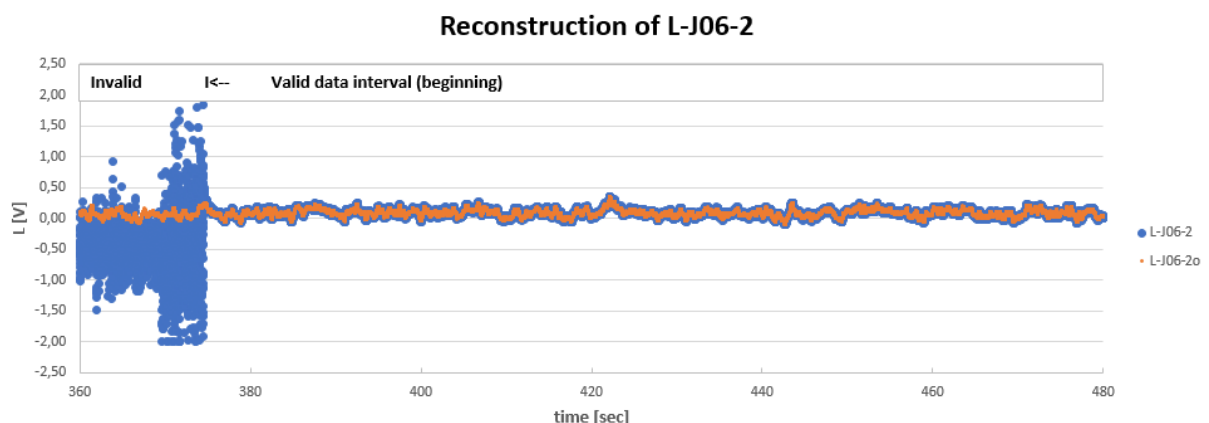


**Figure 69: Reconstruction on L-J06-2 signal - beginning of valid data part**

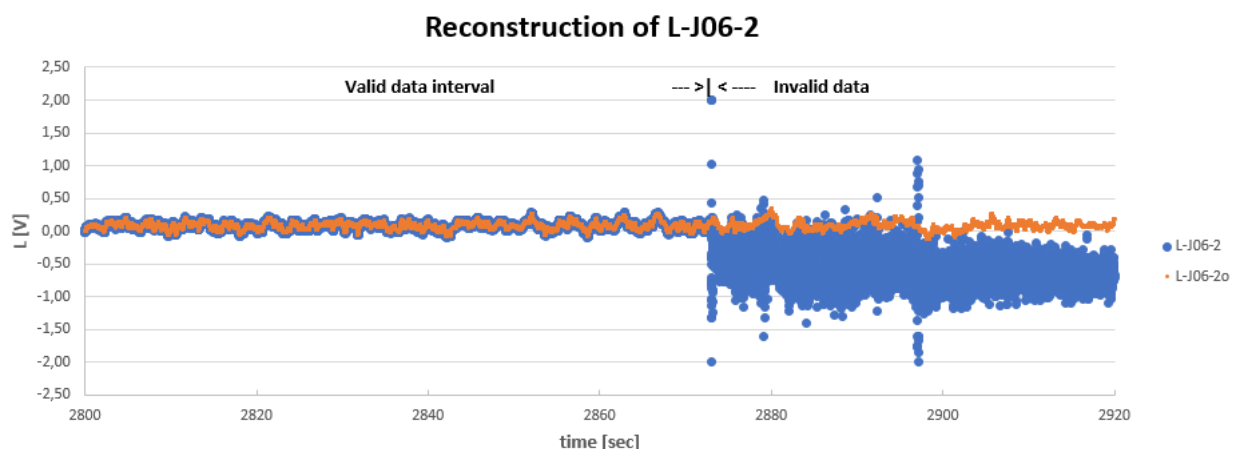


**Figure 70: Reconstruction on L-J06-2 signal - end of valid data part**

All ex-core measurements are OK, as documented in Annex 8.6.

### **Gösgen data BOC 40**

These data are from the end of Gösgen fuel cycle 40 and are described in detail in [ 33 ]. The results of reconstruction are summarised in Annex 8.7 (in-core) and 8.8 (ex-core data).

Some interesting results were also obtained:

- Invalid (defective) measurements are in accordance with [ 33 ] for L-C08-4, LG02-6, L-N08-2.
- Reconstruction of other signals than string L-N08 shows, that they contain a lot of added noise and thus are of low quality, if not invalid.
- The same holds for L-G10-6 signal, although according to [ 33 ] it should be OK.
- Reconstruction of ex-core measurement shows that all ex-core measurements are OK, as documented in Annex 8.8.

### **Gösgen data MOC 40**

These data are from the middle of Gösgen fuel cycle 40, as described in detail in [ 33 ].

The results of the reconstruction are summarised in Annex 8.9 (in-core) and 8.10 (ex-core data). The quality of the data is very similar if not the same as in BOC 40. Reconstruction of ex-core measurement shows, that all ex-core measurements are OK, as documented in Annex 8.10.

### **4.5.3 Conclusions**

This chapter showed that the methodology of neutron in-core and ex-core signal reconstruction - based on linear combination of these signals - works very well, also in the area of fast dynamic measurements; this had not been tested until now. It was shown that each of the six signals of the neutron measurement string of Konvoi reactors can be expressed as a linear combination of the five remaining signals of the same string and each of the eight ex-core signals can be expressed as a linear combination of the seven remaining ex-core signals. This relation can be used both for filling in data gaps and for recognition of invalid (bad, incorrect) measurements.

## 5 Preliminary processing of real data

This section presents some preliminary application of the developed methods on real plant data. The analysis was performed on neutron flux plant data that were provided by several contributors (KKG & ISTec, PEL & GRS, MTA EK, UJV, AMS) for altogether five different PWR reactor types (3 and 4-loop pre-KONVOI, VVER 440 and 1000, 3 and 4-loop WEC).

According to [ 33 ], these data consist mainly of in-core and ex-core neutron signals, but also any other type of signals that could give some hints on the transport of perturbations. A preliminary comparison of the real plant data with the former analysed simulated data was performed in order to check if traces of perturbations can be found in the time and frequency domains.

### 5.1 Swiss 3-loop pre-KONVOI reactor in Gösgen

The main objective of this section is to find the characteristics described in section 3.2.3.2 (i.e. high transit speed of the transport phenomenon, response amplitude at low frequencies, out-of-phase relationship between opposite detectors) and discuss specific findings. For this aim, we analyzed the data from measurement (EOC) cycle 39 of the Swiss NPP with 3-loop reactor. To illustrate the results obtained in the frequency domain, selected spectrograms of power spectral densities in the joint time frequency domain are also presented.

#### 5.1.1 Measurement

The measurement has been performed during a stationary core condition at 100% reactor power in the fuel cycle 39. No control rods have been moved in the measuring time interval. According to the core burn up the measurement was done at nearly the end of the fuel cycle (EOC) or 320 EFPDs (equivalent full power days). The boron concentration in the core amounted to 34 ppm during the measurement. The average core burnup during the measurement was 44 MWd/kgHM.

The core is composed of 177 fuel assemblies (100%) of HTP™ (High Temperature Performance) design delivered by AREVA. The fuel assemblies are characterized by the HTP™ Spacer Grid to improve the thermal-hydraulic performance and the HMP™ end grid to reduce fretting failures in the lower part of the assemblies. The HTP fuel elements are designed to achieve a higher burn up (up to 5 fuel cycles) with a higher enrichment up to 5.06 w/o  $U_{235}$  (ERU) at the beginning of the fuel cycle. The core loading in fuel cycle 39 of Gösgen NPP (KKG) is represented in the following. The Figure 71 and Figure 72 show the radial and axial distributions of the neutron detectors involved in the analysis.

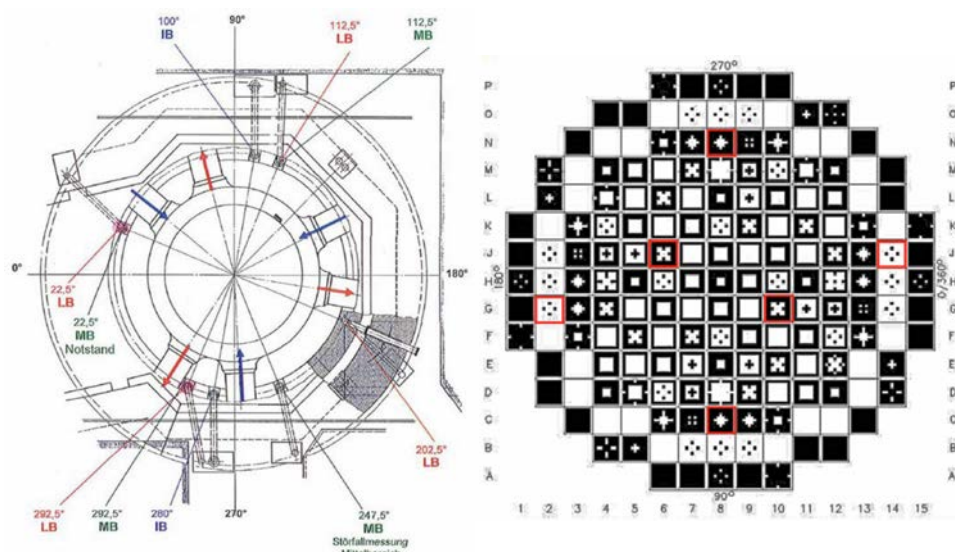


**Figure 71: Radial distribution of excore and incore detectors respectively, note that the figure of incore is rotated 180°.**

### D3.3 Development of advanced signal processing techniques and evaluation results

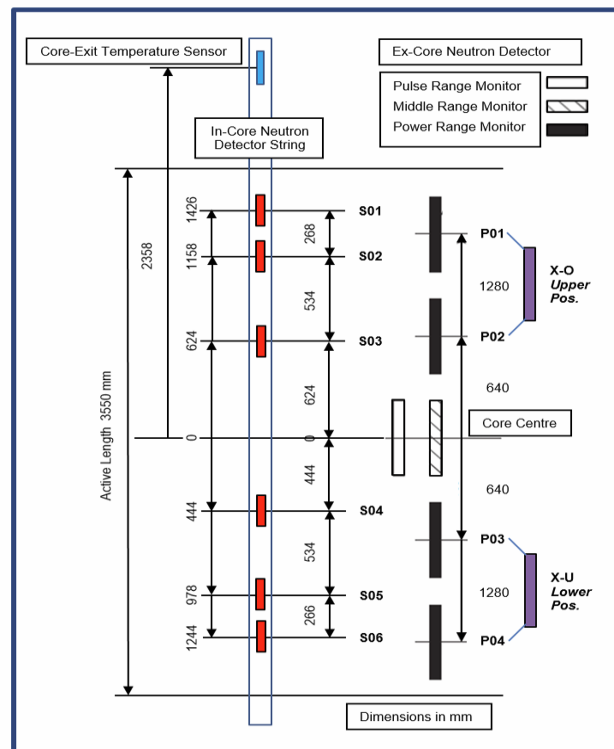


**Figure 72: Axial Positions of Used detectors.**

#### 5.1.2 Preliminary analysis of the spectral characteristics

The objective of the following preliminary analysis is to relate the spectral characteristics observed in simulations and in real signals. For this purpose, a Fourier analysis was performed, by computing the APSDs of the signal, as well as the coherences and phases between pairs of sensors. Then the results were observed analogously as in the simulations.

##### Regarding the APSD:

Figure 73 shows the APSDs of the 8 detectors at level 1 (the uppermost part). On the left-hand side, the APSD is plotted up to 115 Hz, while in the right, up to 10 Hz. We can point out that most of the signal content is located below 1 Hz, and we can appreciate a relative uniformity in the APSDs at different radial positions.

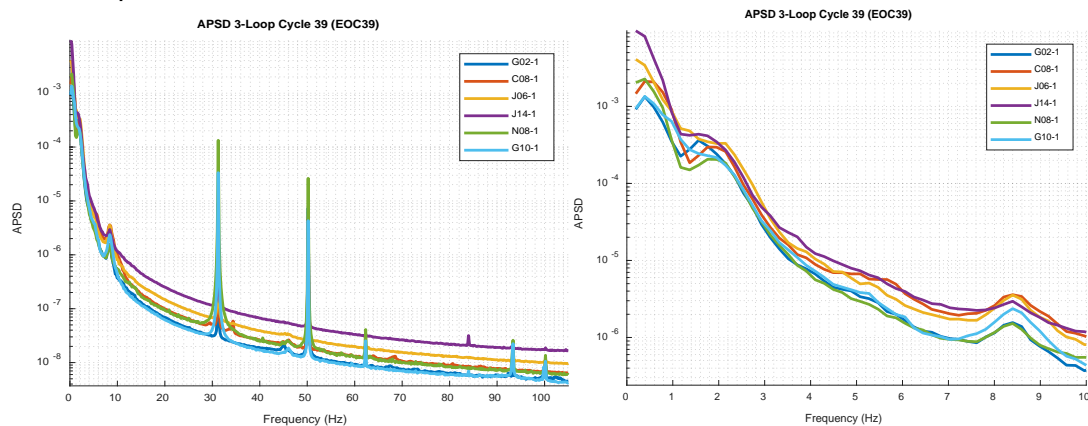


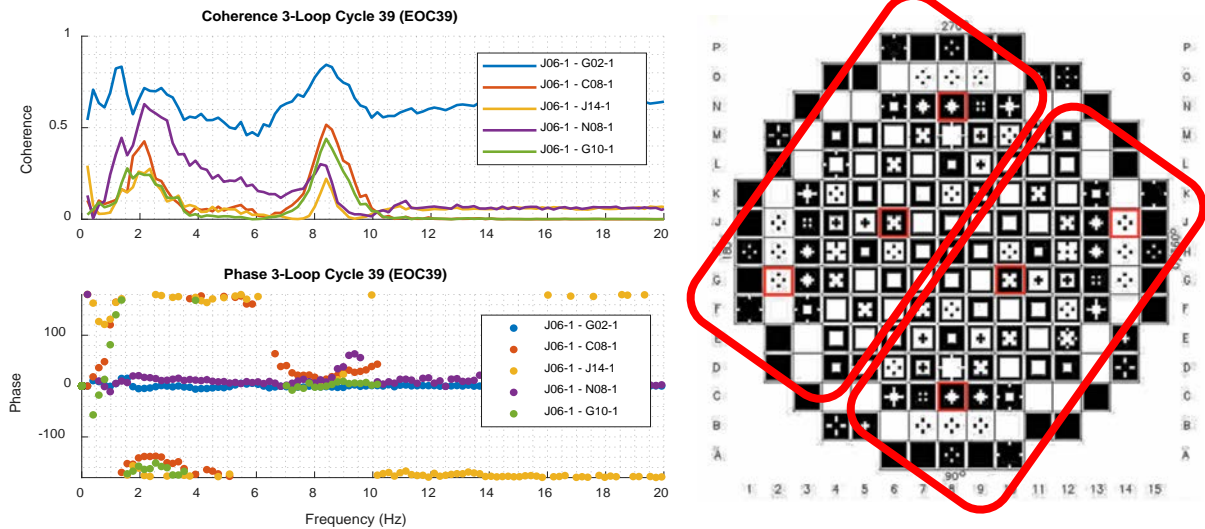
**Figure 73: APSDs of 8 detectors at the level 1 (the uppermost). The right figure shows the APSDs up to 10 Hz.**



### D3.3 Development of advanced signal processing techniques and evaluation results

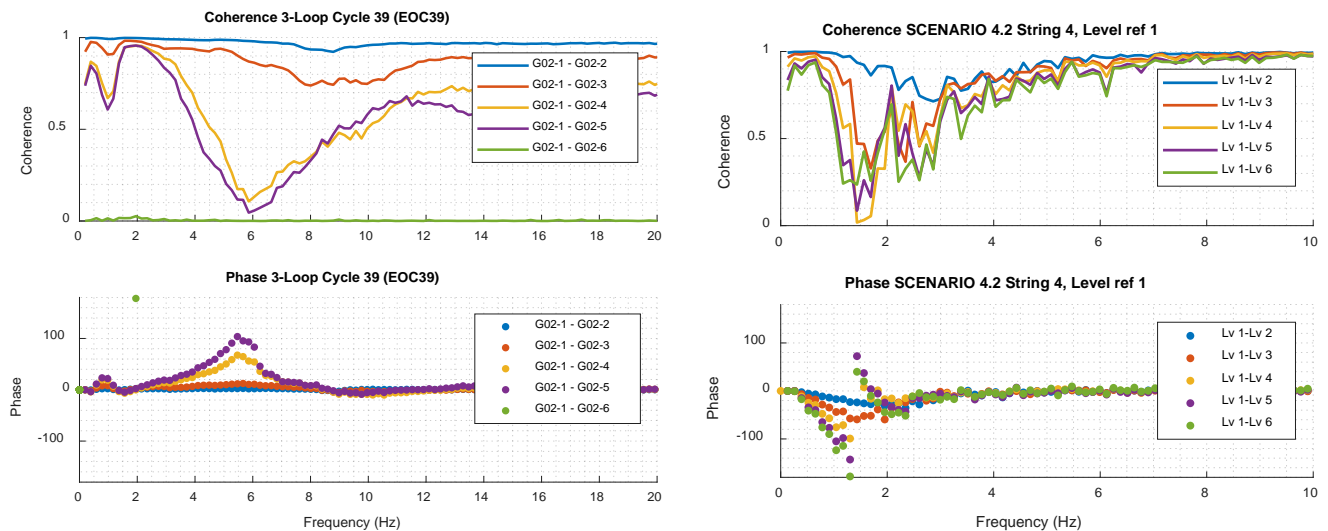
#### Regarding the coherences and phases:

Figure 74, on the left-hand side, shows the coherences and phases between pairs of sensors, using sensor J06-1 as reference. On the right-hand side, it shows how the reactor is divided radially in two out-of-phase zones. In Figure 74 and Figure 75, we can observe that the coherence decreases as the distance from the reference sensor (J06-1) increases, in radial and axial cases.



**Figure 74: Coherences and phases of Incore detectors at level 1 with string J06 as reference.**  
In the left figure we can see the out-of-phase zones.

In the same string taking the coherence and phase between pairs of sensors at the same longitudinal position, we can observe the low slope in the linear phase; this points out a high speed of transport phenomenon. This characteristic is different from what we can observe in simulated mixed scenarios, i.e., with thermal-hydraulic oscillations and mechanical vibrations.



**Figure 75: Coherence and phase between in-core sensors. Real case of Göesgen and PSI simulation of mixed scenario, respectively**



### Regarding joint time frequency domain spectrograms:

The PSD sequences in JTFS spectrogram and range 0 – 100Hz are shown in Figure 76, where the coordinates are: X frequency [Hz], Y time [s] and Z amplitude of PSD [ $1/\text{Hz}^2$ ] in dB. Processing PSD sequences with sliding Hanning window in time intervals of 10 sec results in frequency resolution of 100 mHz. All X, Y, Z values were taken from the delivered file CORTEX D4.1 Goesgen MOC39 Data 07-02-2018 PartA.csv with measurements' record of L-G02-1 SPND.

It should be noted that X-Z JTFS spectrograms are plotted in their maximum amplitude values, so that we can see the frequency dispersion of the peaks through the whole time of record. It is clearly seen that the 1D PSD spectra have somewhat other forms of peaks, e.g. as compared to Figure 56 of 3.4.2 section.

The whole range of 0 – 100Hz was initially divided (as shown in Annex 8.1) into ranges of frequencies (0-10Hz, 10-20Hz, 20-30Hz, 30-50Hz, 50-100Hz); these can be investigated in more detail for subsequent signal analysis of preliminary feature extraction, selection and classification; these can feed DNN training.

In this case, it is worth noting that it is possible to pre-select time intervals for further processing, in order to bypass isolated faults (one per record) of hitherto unknown origin. This can also be applied to the case of long records (tens to hundred minutes) with dynamically changing time waveforms (transients).

The upper L-G02-1 SPND in Goesgen EOC of U1C39 in the frequency range 0 – 100Hz was selected for preliminary comparison with other investigated reactors under similar initial conditions.

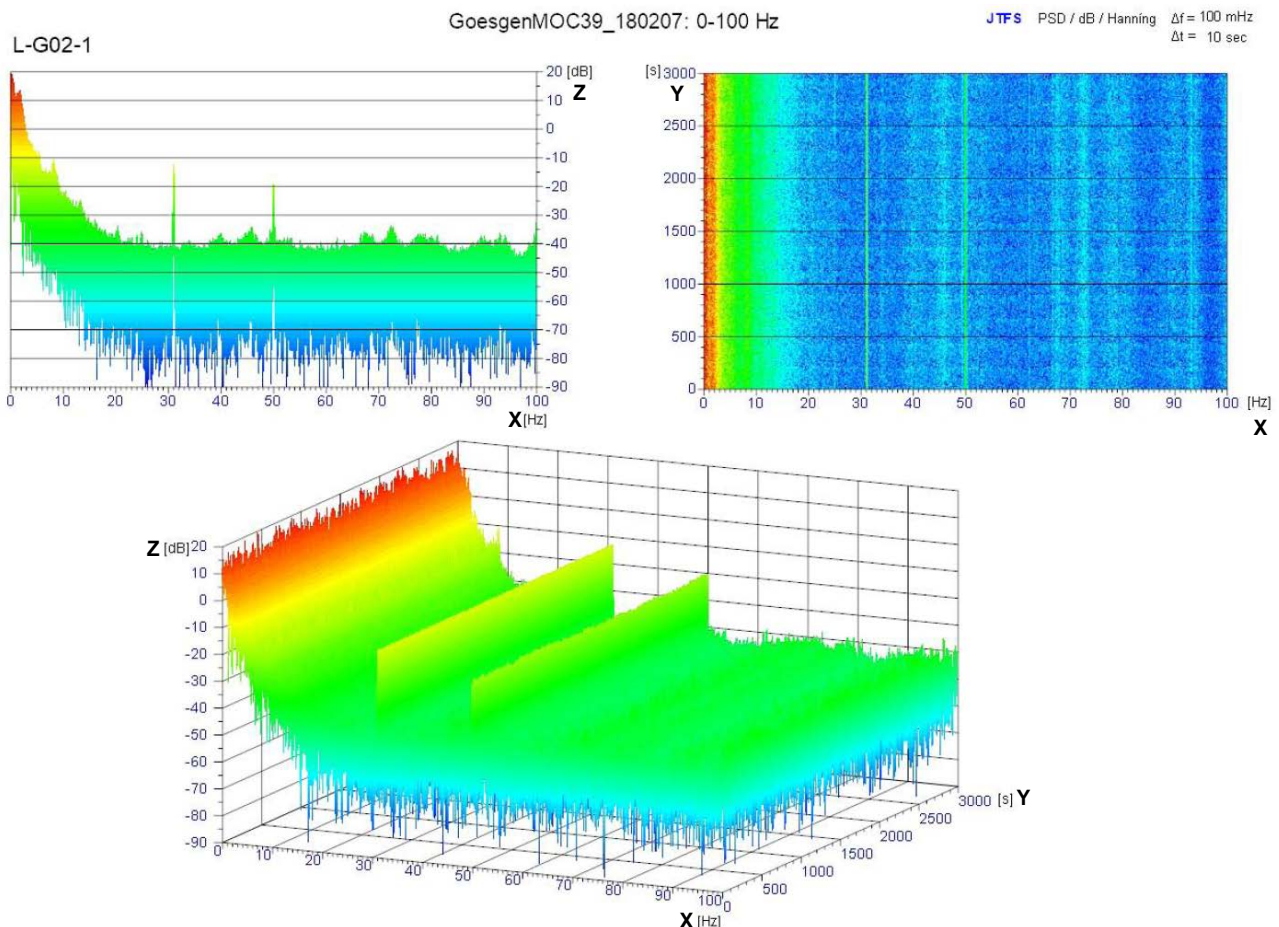


**Figure 76 JTFS spectrogram of upper L-G02-1 SPND in Goesgen EOC of U1C39 in the frequency range 0 – 100Hz**

## 5.2 American 4-loop and 3-loop Westinghouse reactors

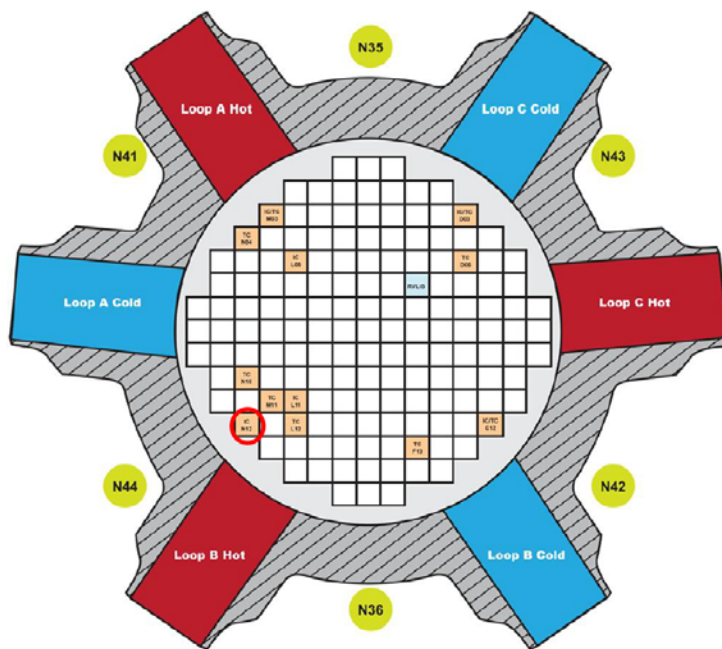
In this task we used the data provided by AMS (Analysis and Measurement Services Corporation). The noise analysis data sets were prepared from one 3-loop PWR and two 4-loop PWRs that have experienced various reactor internals anomalies. The preliminary steps to analyse these PWR data were done by selecting mother wavelets, as well as sensors, for comparable processing with other reactors in the joint time frequency domain.

### 5.2.1 Measurement

Both types of reactors exhibit radial distribution of the in-core and ex-core neutron detectors shown in Figure 77 and Figure 78 along with typical design parameters.

The data consisted of signals in time domain, measured by various sensors in two different types of nuclear reactors; 3-loop Westinghouse PWR (Pressurized Water Reactor) and 4-loop Westinghouse PWR. The types of sensors involved were the following:

1. In-Core Flux Sensors
2. Intermediate Range NI (Nuclear Instrumentation)
3. Power Range NI
4. Reactor Vessel DP (RVLIS)
5. Core Exit Thermocouple



Active Core Length	3.66 m
Active Core Diameter	3.05 m
Number of Fuel Assemblies	157
Vessel Wall Thickness	203 mm
Vessel Wall Height	13.0 m
Vessel Inside Diameter	4.0 m
Core Inlet Temperature	284°C
Core Outlet Temperature	322°C
Reactor Coolant Pumps (RCPs)	3
RCP Speed (at operating temp.)	1190 rpm
Number of Loops	3
Number of Turbines	1
Turbine Speed (RPM)	1800
Net Electrical Output	860 MW

Typical Design Parameters for a Three-Loop Westinghouse PWR  
Source: World Nuclear Industry Handbook, Nuclear Engineering International

**Figure 77 The radial distribution of the in-core and ex-core neutron detectors of 3-loop Westinghouse reactor**

### D3.3 Development of advanced signal processing techniques and evaluation results

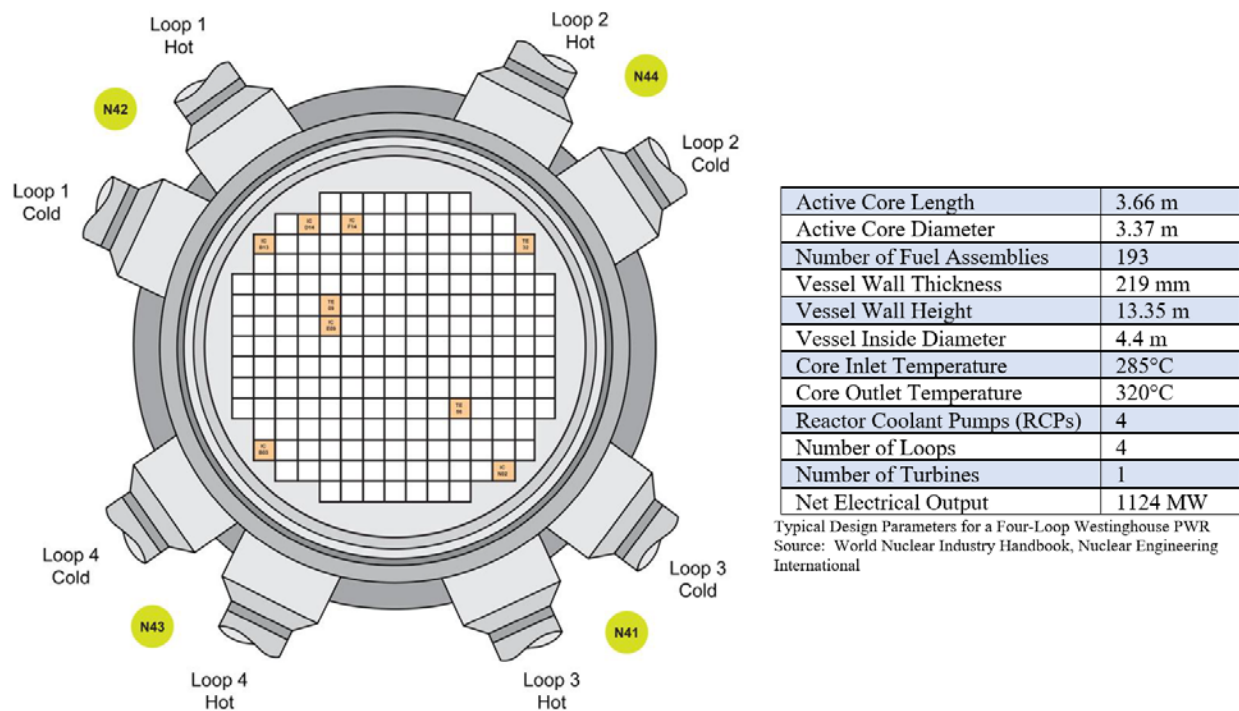


**Figure 78 The radial distribution of the in-core and ex-core neutron detectors of 3-loop Westinghouse reactor**

#### 5.2.2 Mother Wavelet Selection

We followed a similar approach to the one described in Section 3.3 in order to observe similarities (or differences) between real and simulated data. The analysis consisted of two steps; trend detection and removal and mother wavelet selection.

In the first step, the underlying trend of data has been removed. This is a very important task because it improves the wavelet decomposition. A linear trend of small amplitude was observed in the data and was subsequently removed.

Next we performed wavelet analysis to find the best mother wavelet that fits the signals in the wavelet decomposition. The selection of the optimal mother wavelet was based on the energy-to-entropy and cross-correlation criteria discussed in Section 3.3.1.1., which were applied on every signal for each mother wavelet. In order to find one mother wavelet for all signals a voting scheme has been employed. This means that the selected mother wavelet has been the one that best fit a signal. This analysis on the detrended signals yielded that the best mother wavelet was Bi-Orthogonal 5.5, based on the energy-to-entropy criterion and Bi-Orthogonal 3.1, based on the cross-correlation criterion.

The selected optimal mother wavelet for the real data is of the same family of wavelets (Bi-Orthogonal) as the one selected for the simulated data. Particularly, using the cross-correlation criterion, the mother wavelet is the same (Biothogonal-3.1), while using the energy-to-entropy criterion, the mother wavelet is within the same family but with different hyperparameters. Therefore, an initial observation is that there exists a connection in the optimal mother wavelet selection between the simulated and the real data.



### 5.2.3 Joint Time Frequency Domain

The PSD sequences in JTFS spectrogram in range 0 – 100Hz are shown in Figure 79, where the coordinates are: X frequency [Hz], Y time [s] and Z as amplitude of PSD [ $1/\text{Hz}^2$ ] in dB. Processing PSD sequences with sliding Hanning window in time intervals of 10 sec results in frequency resolution of 100mHz. All X, Y, Z values were taken from delivered file P3-1a-1.csv, with measurement record of IC-N12-44 fission ionization chamber in lower core position.

It should be noted that X-Z JTFS spectrograms are plotted in their maximum amplitude values, so that we can see the frequency dispersion of the peaks through the whole time of record. It is then clearly seen that the 1D PSD spectra have somewhat other forms of peaks, e.g. as compared to Figure 56 of 3.4.2 section.

The whole range of 0 – 100Hz was initially divided (as shown in Annex 8.2) into ranges of frequencies (0-10Hz, 0-25Hz, 10-25Hz); these can be investigated in more detail through subsequent signal analysis of preliminary feature extraction, selection and classification; finally they can feed DNN training.

On this occasion it is also worth to repeat that there is a possibility of pre-selecting time intervals for further processing, in order to bypass isolated faults (one per record) of hitherto unknown origin. This can be applicable to the case of long records (tens to hundreds minutes – especially in the AMS data sets), with dynamically changing time waveforms (transients).

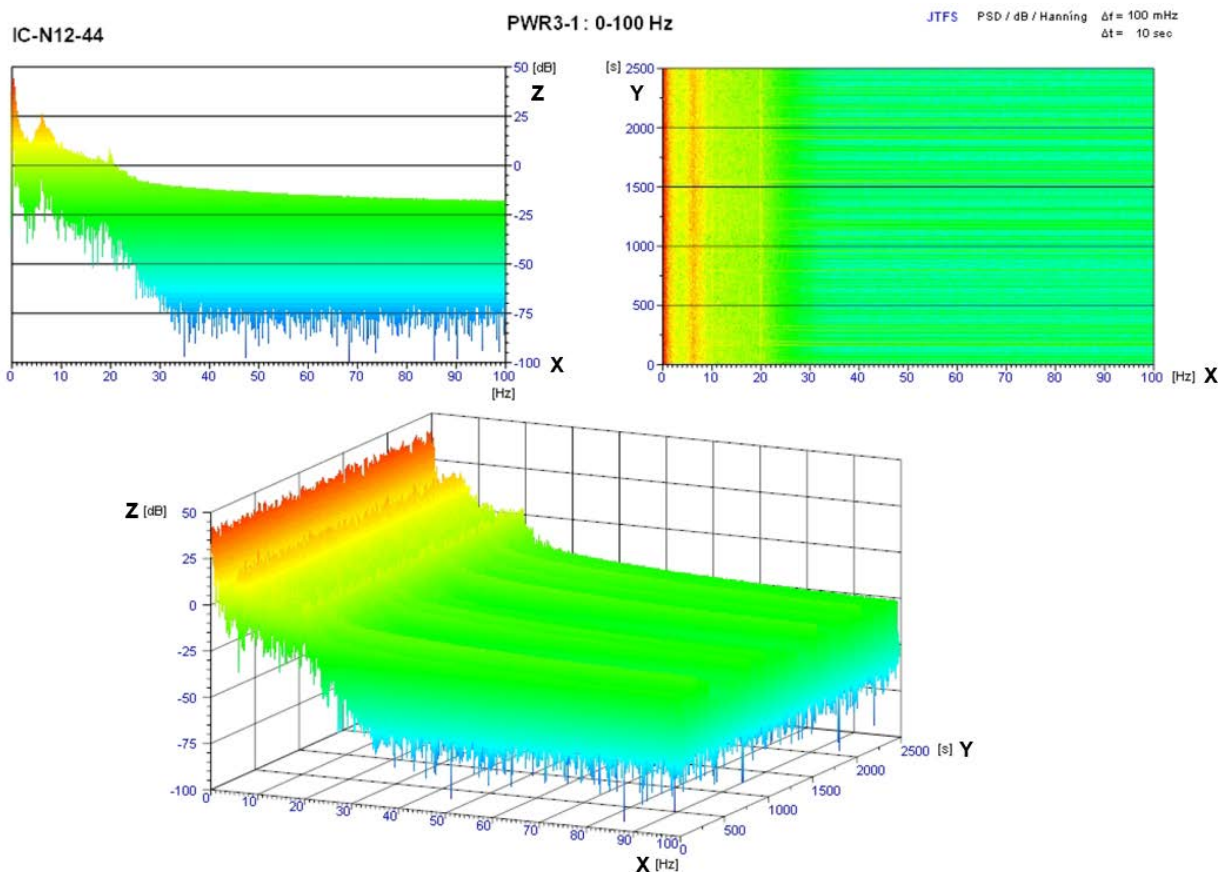


**Figure 79 JTFS spectrogram of lower fission chamber IC-N12-44 in WEC PWR3 in the frequency range 0 – 100Hz**

### 5.3 German 4-loop pre-KONVOI reactor

This section describes the preliminary processing of provided neutron noise measurements from a German pre-KONVOI reactor in joint time frequency domain. Radial and axial detector positions for this type of a reactor are shown in Figure 80.

The pre-KONVOI reactor's main data are as follows: Thermal power 3765 MWth, KWU/Siemens built 4-loop PWR, 193 fuel assemblies, 390 cm active core height, 16x16-20 fuel assembly layout, 23 cm fuel assembly pitch, 1.430 cm fuel rod pitch and 1.075 cm fuel rod outer diameter.

#### 5.3.1 Measurement

The following three measurements from cycle 30 to cycle 32 were done at EOC conditions

1. Cycle 30 on 28.02.2012 at 78 ppm, 3730 MWth, 304.2°C average coolant temperature
2. Cycle 31 on 06.03.2013 at 88 ppm, 3729 MWth, 304.2°C average coolant temperature
3. Cycle 32 on 02.04.2014 at 78 ppm, 3610 MWth, 304.7°C average coolant temperature

The core has eight radial positions with n-β detectors. In each of those positions, the axial string contains six n-β detectors. The layout of the radial and axial positions is shown in Figure 80. Each string of six detectors is in an unoccupied guide tube of each of the monitored fuel assembly.

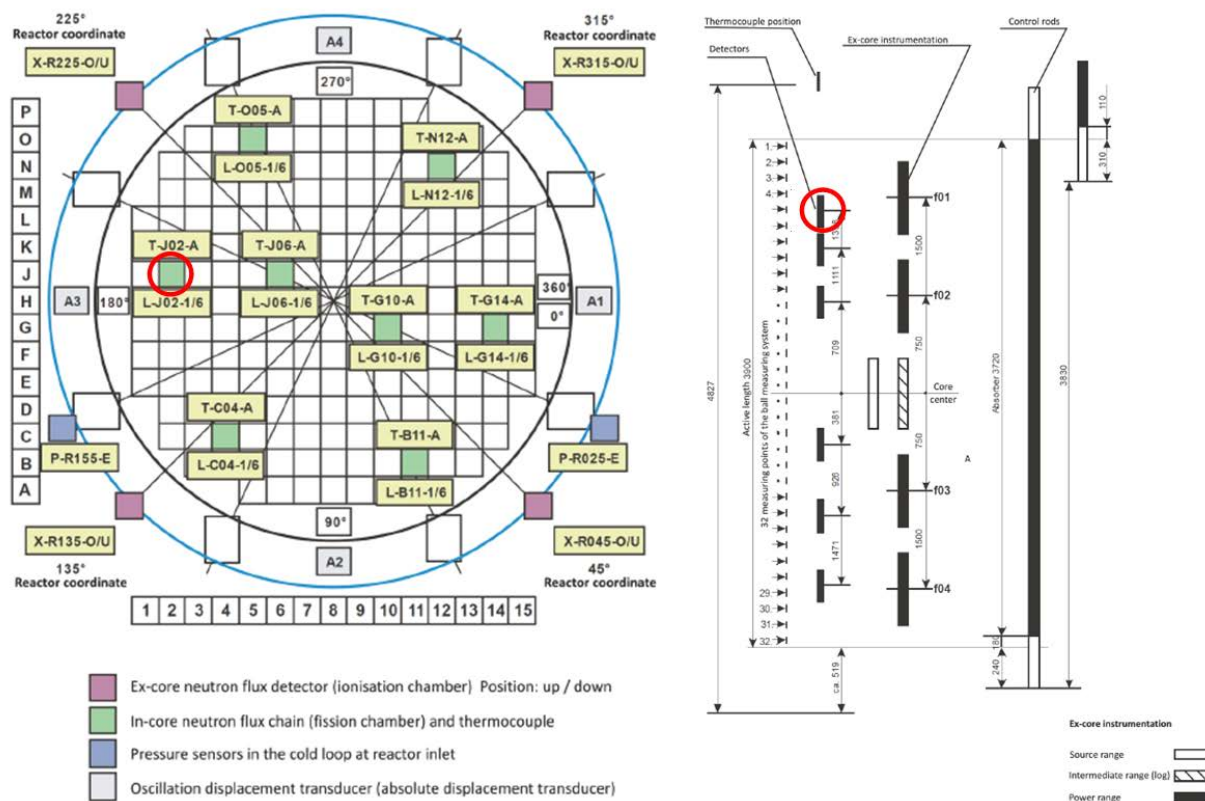


Figure 80 Radial and axial detector positions in the German 4-loop pre-KONVOI reactor

### 5.3.2 Joint Time Frequency Domain

The PSD sequences in JTFS spectrogram in range 0 – 100Hz are shown in Figure 81, where the coordinates are: X frequency [Hz], Y time [s] and Z as amplitude of PSD [ $1/\text{Hz}^2$ ] in dB. Processing PSD sequences with sliding Hanning window in time intervals of 10 sec results in frequency resolution of 100mHz. All X, Y, Z values were taken from the delivered file DC-DWR\_64\_KANAL\_A\_30.csv, with the measurement record of L-J02-1 SPND in the upper core position.

It should be noted that X-Z JTFS spectrograms are plotted in their maximum amplitude values, so that we can see the frequency dispersion of the peaks through the whole time of record. It then becomes clear that the 1D PSD spectra have somewhat other forms of peaks, e.g. as compared to Figure 56 of section 3.4.2.

The whole range of 0 – 100Hz was initially divided (as shown in Annex 8.2) into ranges of frequencies (0-10Hz, 10-20Hz, 20-30Hz, 30-50Hz, 50-100Hz); these can be investigated in more detail through subsequent signal analysis including preliminary feature extraction, selection and classification; then they can be used for feeding DNN training.

It is also worth repeating that there is a possibility of pre-selecting time intervals for further processing, in order to bypass isolated faults (one per record) of hitherto unknown origin. This can be also applied to the case of long records (tens to hundreds) with dynamically changing time waveforms (transients).

The upper L-J02-1 SPND in KWU EOC of U1C30 in the frequency range 0 – 100Hz was selected for preliminary comparison with other investigated reactors under similar initial conditions.

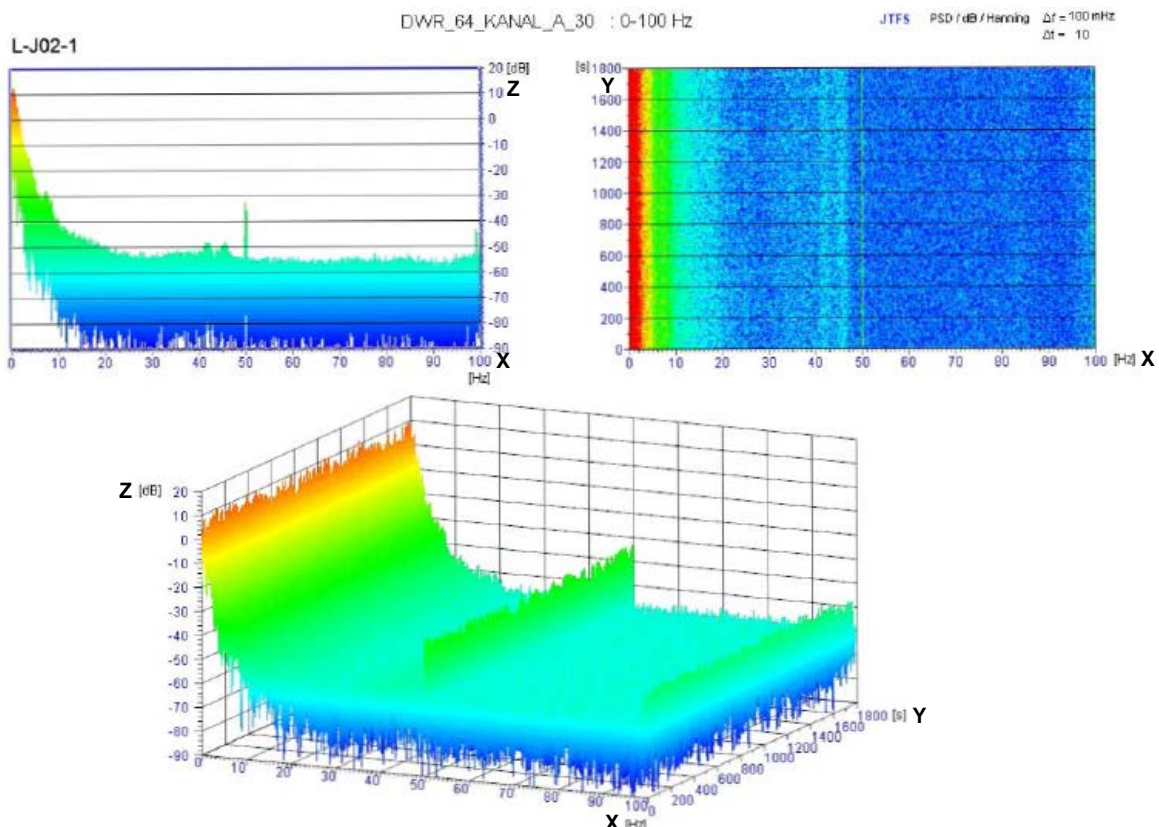


**Figure 81 JTFS spectrogram of upper LJ02-1 SPND of German 4-loop pre-KONVOI reactor in EOC U1C30 in the frequency range 0 – 100Hz**



## 5.4 Czech 4 loop VVER 1000 reactor in Temelin

This PWR has 193 fuel assemblies of TVSA-T type with length 4 570 mm and diameter 248,53 mm. There are 312 pcs of rods per fuel assembly with fuel column height 3 680 mm, rod outer diameter 9,1 mm and rod pitch 12,75 mm. Rod max burnup is rated on 72 MWd/kgU and on average linear loading 156,3 W/cm.

### 5.4.1 Measurement

The radial location of in-core strings N01-64, ex-core detectors YC00X006-29, reactor head accelerometers YC00A511-4 and main circulating loops MCL1-4 are shown in Figure 82. The fuel assembly instrumented with SPNDs (string S31 as an example) is also shown in Figure 82. There are 256 diagnostic Rh SPNDs with lead/emitter part diameter 1.00/1.52 mm, with 242.5mm length and 13,990 mm cable length. The ex-core instrumentation contains altogether 12 ionization chambers located in three vertical planes.

There are four noise data records available from consecutive U1C10 – U1C12 cycles (2010-3). All noise records were taken at BOC conditions during physical tests of the neutron instrumentation. The preliminary U1C09 cycle dataset processing in joint time frequency domain is described in this section for the frequency range 0 – 150Hz.

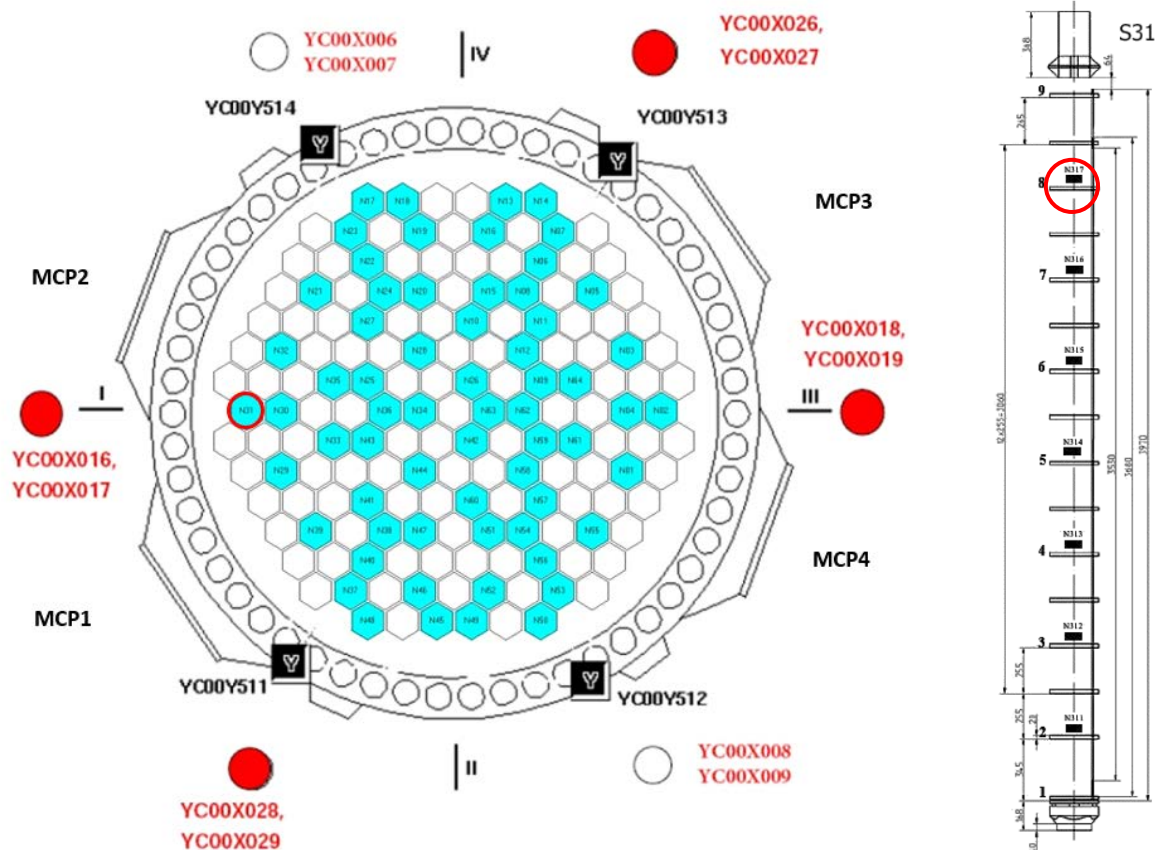


Figure 82 Radial and axial detector positions in the Czech 4 loop VVER 1000 in Temelin

### 5.4.2 Joint Time Frequency Domain

The PSD sequences in JTFS spectrogram in range 0 – 150Hz are shown in Figure 83, where the coordinates are: X frequency [Hz], Y time [s] and Z as amplitude of PSD [ $1/\text{Hz}^2$ ] in dB. Processing PSD sequences with sliding Hanning window in time intervals of 10 sec results in frequency resolution of 100mHz.

All X, Y, Z values were taken from delivered files 75-Zona1\_X\_N.xlsx, 69-Zona3.xlsx, 71-Zona5.xlsx, and 73-Zona7\_X\_N.xlsx with measurement records of N311, N313, N315, N317 SPNDs from all axial core positions in S31 fuel assembly.

It should be also noted that X-Z JTFS spectrograms are plotted in their maximum amplitude values so that we can see the frequency dispersion of the peaks through the whole time of record. It is then clear that the 1D PSD spectra have somewhat other forms of peaks, e.g., as compared to Figure 56 of 3.4.2 section.

The whole range of 0 – 150Hz was initially divided (as shown in Annex 8.4) into ranges of frequencies (0-10Hz, 10-20Hz, 20-30Hz, 30-50Hz, 50-100Hz, 100-150Hz); these can be investigated in more detail through subsequent signal analysis, including preliminary feature extraction, selection and classification; finally being provided as input to DNN training. The JTFS spectrograms of axially positioned SPNDs in one fuel assembly (S31) are shown in Annex 8.4 to point out that quite distinct signal behavior could also be a reality.

It is also worth highlighting that there is a possibility of pre-selecting time intervals for further processing, in order to bypass isolated faults (one per record) of hitherto unknown origin. This can also be applicable to the case of long records (tens to hundreds) with dynamically changing time waveforms (transients).

The record of upper N317 SPND of Temelin BOC U1C09 in the frequency range 0 – 150Hz was selected for preliminary comparison with other investigated reactors under similar initial conditions.

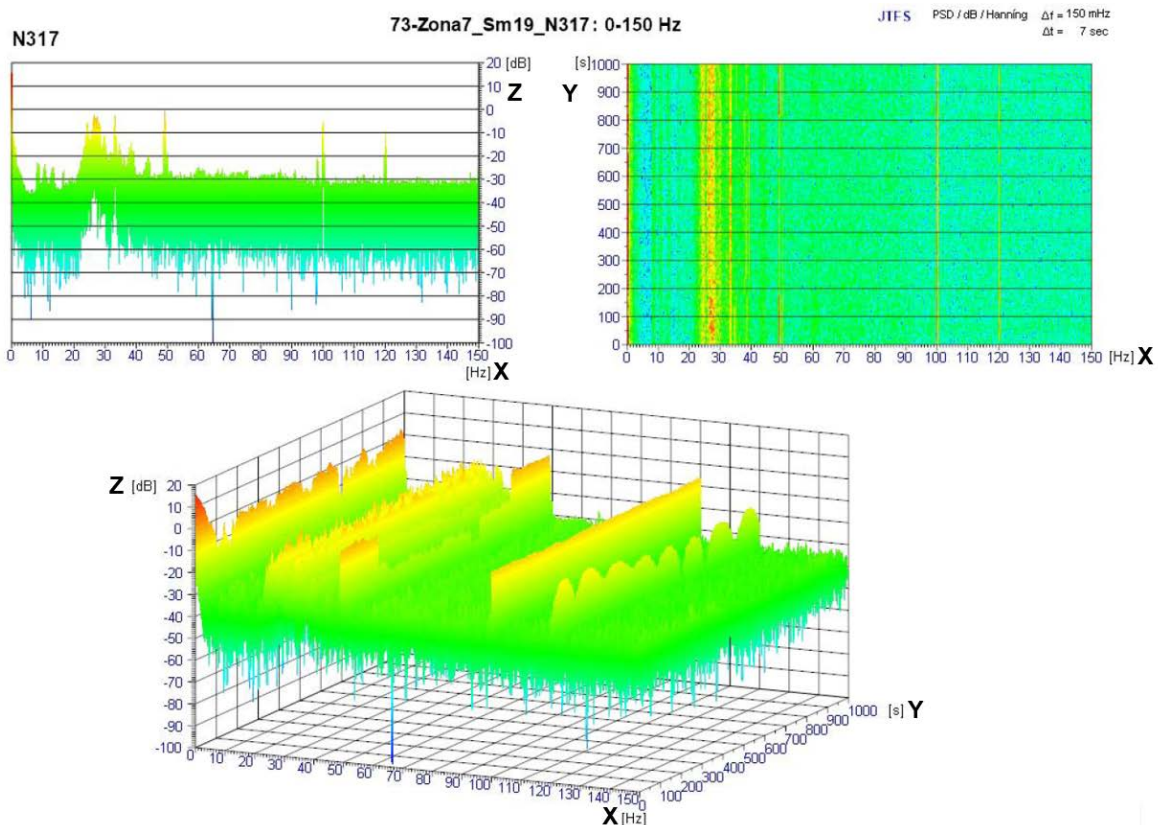


**Figure 83 JTFS spectrograms of upper N317 SPND in the Czech 4 loop VVER 1000 Temelin of BOC U1C09 in the frequency range 0 – 150Hz**

## 5.5 Conclusions

In this section, the analysis of simulation and real plant data in frequency, time and joint time frequency domains were done by spectral FFT analysis (power density, coherence, phase studies, short time FFT spectrograms), Wavelet and Hilbert-Huang transformations.

It is obvious that fulfilling the overall goals of the CORTEX WP4 requires to work on multilevel analysis basis, as illustrated in Figure 84 (Cortex workshop, UJV Rez, February 2019, [ 13 ]). The different steps described in this Figure can be further divided into several subcategories, as follows:

Pre-processing phase:	Filtering, artefact detection/removing, signal segmentation
Feature extraction phase:	Statistical features, spectral/coherence analysis, wavelet transform, singular spectrum analysis
Classification phase:	Linear models, neural networks, mixture models, fuzzy approaches, ensemble learning
Visualisations:	Necessary activity in result demonstration. It is illustrated e.g. in chapters 3.1, 3.2, 3.5.2, Annexes A1 – A4 or in [ 33 ] (D4.3, VVER440, p.63)
Optimizations:	It is a repeating point in all subcategories.

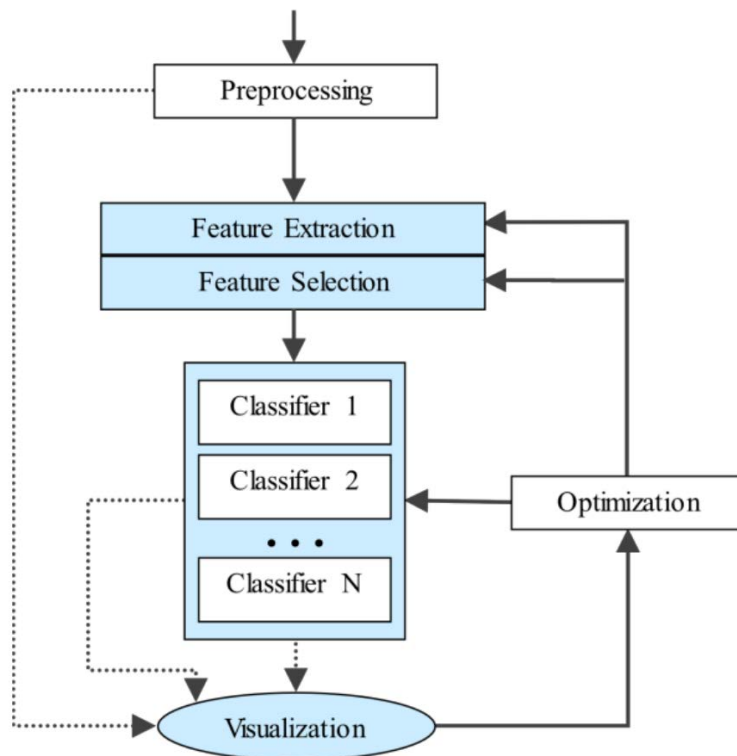


**Figure 84 Multilevel analysis process**

## 6 Conclusions

The developed advanced signal processing methods in WP3 have the ability to provide thoughtful analysis and extract relevant and meaningful fluctuations from measured signals.

The analysis of frequency domain simulated data, describing the induced neutron noise throughout the core, provided cues that justify our approach intended to successfully investigate the simulated data having more complicated structure and better corresponding to real plant conditions.

Spectral analysis of simulated time series of fuel vibrations and flow/temperature fluctuations also shows the capability to elaborate maps of features for effective recognition of patterns in the signals.

By selecting first the optimal mother wavelet, we were able to apply the wavelet transformation and based on scaleograms to effectively perform feature extraction, classification and localization; these can subsequently be used for DNN training.

In the chain of these signal processing methods, investigating operational vibration phenomena, through short time Fourier transform in joint time frequency domain, proves to be a useful pre-processing tool for quick summary generation and visualization.

The methods developed in WP3 will thus enable an efficient processing of large volumes of data from nuclear facilities to be undertaken in the context of WP4.

## 7 References

- [ 1 ] Demazière C, P. Vinai P., M. Hursin M., Kollias S., Herb J.  
Noise-based core monitoring and diagnostics – overview of the Cortex project  
Advances in Reactor Physics, Mumbai, December 2017
- [ 2 ] Demazière C., Vinai P., Hursin M., Kollias S., Herb, J.  
Overview of the Cortex project  
PHYSOR, Mérida, April 2018
- [ 3 ] Alexandridis G.  
Signal processing methodologies for nuclear reactor data  
Presentation in CORTEX workshop, Rez, February 22, 2019
- [ 4 ] Tambouratzis T.  
The Combination of State-of-the-Art Signal Processing and the Computational  
Intelligence Paradigm for the Efficient, Accurate and Robust Processing of Nuclear  
Reactor Data Signal  
Presentation in CORTEX workshop, Rez, February 22, 2019
- [ 5 ] Mallat, Stéphane. A wavelet tour of signal processing. Elsevier, 1999.
- [ 6 ] Ma, X., Chengke Zhou, and I. J. Kemp. "Automated wavelet selection and  
thresholding for PD detection." IEEE Electrical Insulation Magazine 18.2 (2002): 37-  
45.
- [ 7 ] Li, Wenjie. "Research on extraction of partial discharge signals based on wavelet  
analysis." 2009 International Conference on Electronic Computer Technology.  
IEEE, 2009.
- [ 8 ] Bafroui, Hojat Heidari, and Abdolreza Ohadi. "Application of wavelet energy and  
Shannon entropy for feature extraction in gearbox fault detection under varying  
speed conditions." Neurocomputing 133 (2014): 437-445.
- [ 9 ] Jafarizadeh, M. A., et al. "Asynchronous input gear damage diagnosis using time  
averaging and wavelet filtering." Mechanical Systems and Signal Processing 22.1  
(2008): 172-201.
- [ 10 ] Kankar, Pavan Kumar, Satish C. Sharma, and Suraj Prakash Harsha. "Fault  
diagnosis of ball bearings using continuous wavelet transform." Applied Soft  
Computing 11.2 (2011): 2300-2312.
- [ 11 ] Shannon, Claude Elwood. "A mathematical theory of communication." Bell system  
technical journal 27.3 (1948): 379-423.
- [ 12 ] L. Deng, M. Seltzer, D. Yu, A. Acero, A.-r. Mohamed and G. Hinton, "Binary Coding  
of Speech Spectrograms Using a Deep Auto-encoder," in Interspeech 2010, 2010.
- [ 13 ] Lhotska L., Gerla V.  
Challenges in signal processing in complex applications  
Presentation in CORTEX workshop, Rez, February 22, 2019
- [ 14 ] Bermejo J., Montalvo C., Ortego A.  
On the possible effects contributing to neutron noise variations in KWU-PWR  
reactor: Modelling with S3K  
in Progress in Nuclear Energy, 2017, vol. 95, pp. 1–7.



*D3.3 Development of advanced signal processing techniques and evaluation results*

- [ 15 ] Torres L. A., Chionis D., Montalvo C., Dokhane A.  
Neutron noise analysis of simulated mechanical and thermohydraulic perturbations in a PWR core  
Annals of Nuclear Energy 126, April 2019
- [ 16 ] Zeman V., Hlavac Z. : “Dynamic response of WWER 1000 type reactor excited by the main circulating pump pressure pulsations“, Colloquium Dynamics of Machines, Prague, February 2008
- [ 17 ] Pecinka L., Stulik P. : “Experimental verification of WWER 1000/320 reactor dynamic response to pressure pulsations generated by the main circulating pumps“, Colloquium Dynamics of Machines, Prague, February 2008
- [ 18 ] Pochyly F., Haban V. : “Study of pressure fluctuations in the WWER 1000/320 primary circuit“, Technical University of Brno, Report No VUT-EU13303-QR-14-08, December 2008, in Czech
- [ 19 ] Pecinka L., Stulik P., Zeman V.: “Pressure pulsations generated by main circulation pumps”  
PVP2009-77304, Proceedings of 2009 ASME Pressure Vessels and Piping Division Conference, July 26-30, 2009, Prague, Czech Republic
- [ 20 ] Pecinka L., Stulik P. : Pulsations of coolant flow through reactor V1000/320 generated by the slightly different revolutions of main circulation pumps Colloquium Dynamics of Machines, Prague, February 7 – 8, 2012
- [ 21 ] Stulik P.  
WWER 1000/320 reactor fuel dynamic behaviour in joint time frequency domain Reactor Noise Knowledge Transfer Meeting, UJV Rez, Chalmers University Göteborg, Prague, Czech Republic, October 16-19, 2012.
- [ 22 ] Pecinka L., Svrcek M. : Parametric oscillations of the coolant in PWR primary circuit Computational Mechanics, 31st Conference, Špičák, Czech Republic, November 9-11, 2015
- [ 23 ] Stulik P.  
Noise analysis in NPP diagnostic data processing  
Presentation in CORTEX workshop, Rez, February 22, 2019
- [ 24 ] Pantera, L. and Traore, O.I.  
Reproducible Data Processing Research for the CABRI R.I.A experiments Acoustic Emission signal analysis  
ANIMMA Conference (Lisbon), 2015
- [ 25 ] Traore, O.I. and Favretto-Cristini, N. and Pantera, L. and Cristini P. and Viguiet-Pla, S. and Vieu, P.  
Which Methods and Strategies to Cope with Noise Complexity for an Effective Interpretation of Acoustic Emission Signals in Noisy Nuclear Environment,  
Acta Acustica United with Acustica Vol. 103 (2017) 903-916
- [ 26 ] Traore, O.I. and Pantera, L. and Favretto-Cristini, N. and Viguiet-Pla, S.  
Emission acoustique et traitement du bruit : cas de signaux expérimentaux en contexte nucléaire,  
CFA 2016, 13e Congrès Français d'Acoustique, Le Mans, France,  
<https://hal.archives-ouvertes.fr/hal-01308134>

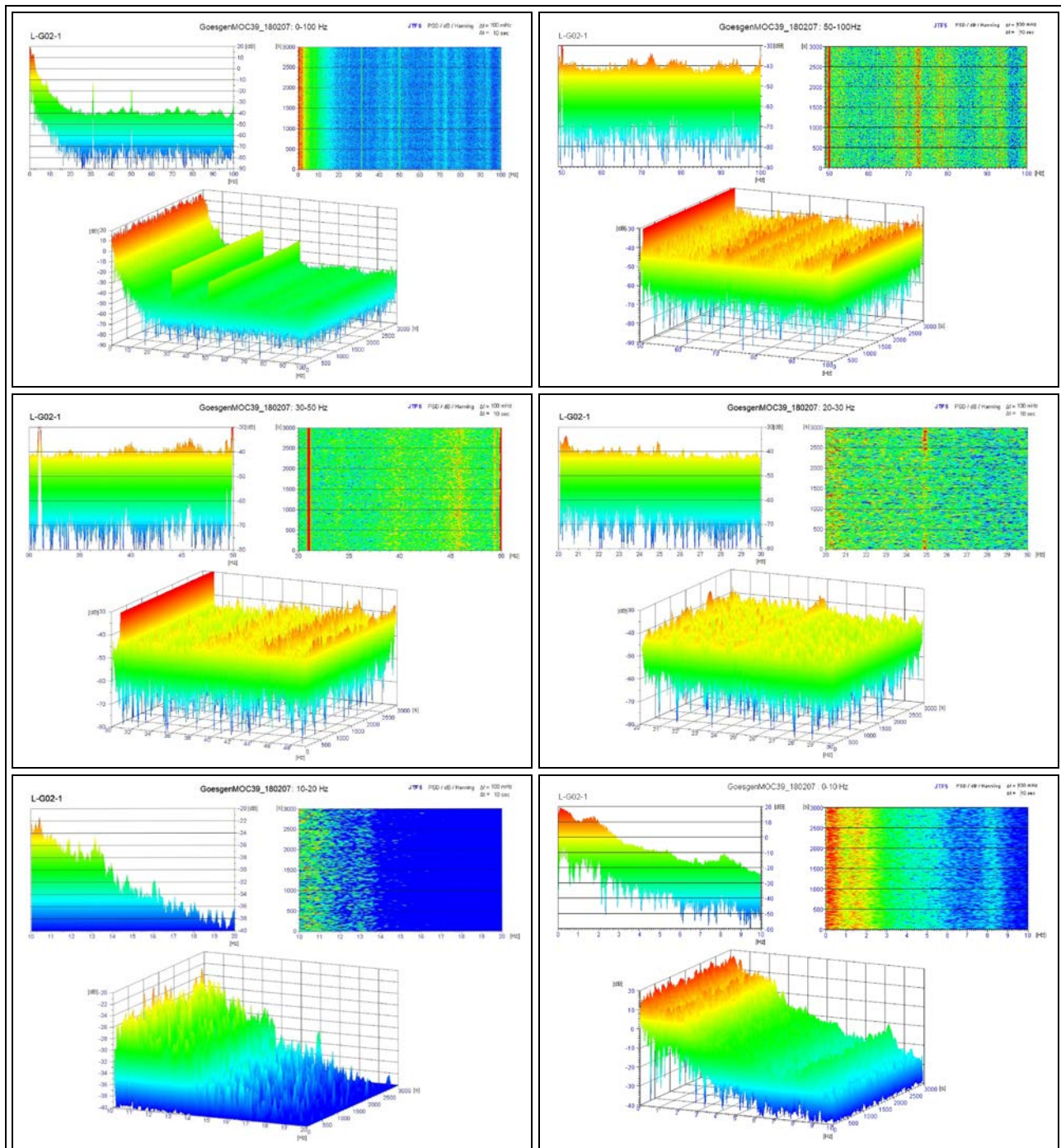
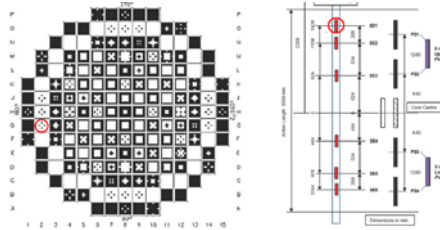


### *D3.3 Development of advanced signal processing techniques and evaluation results*

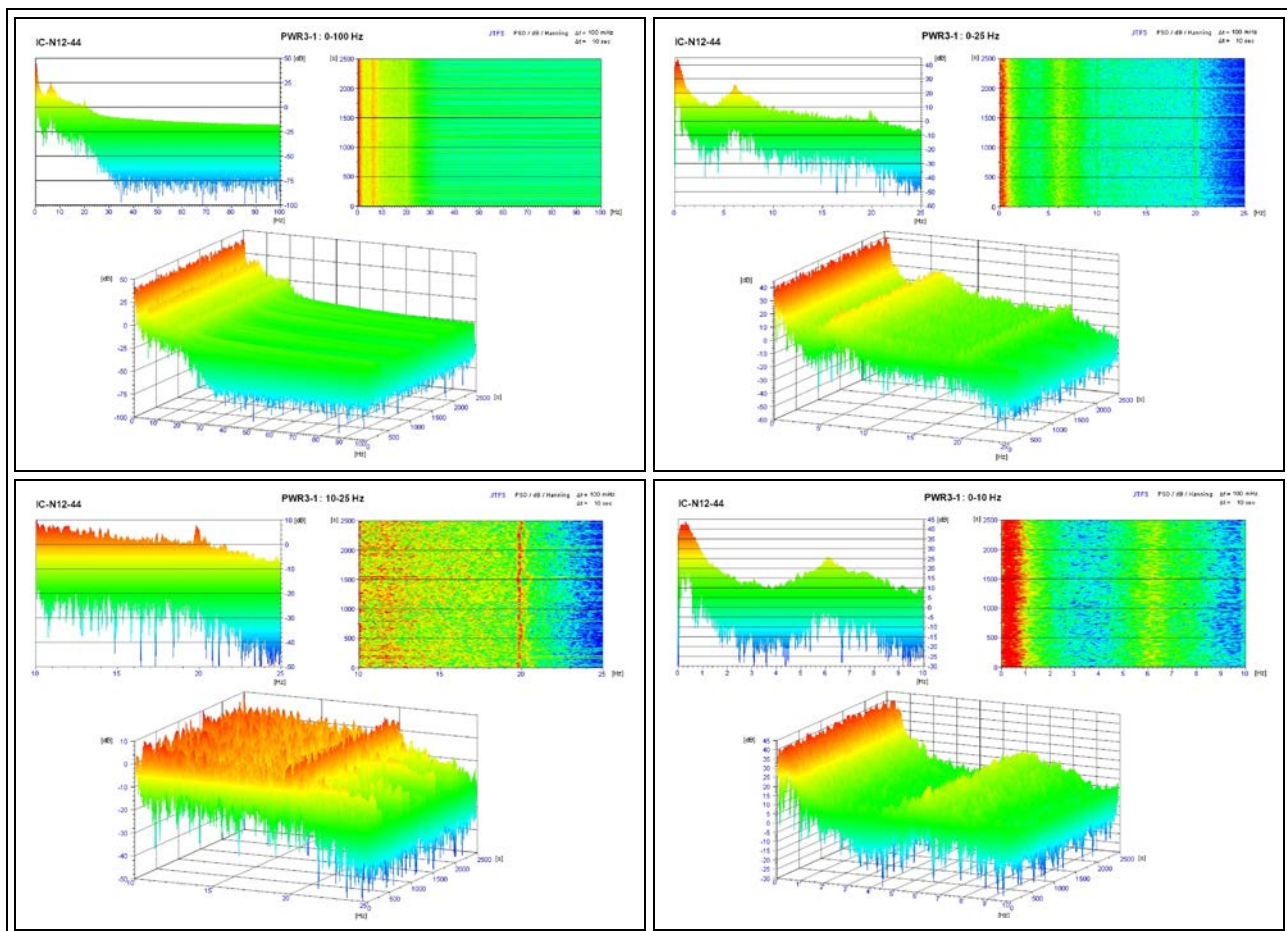
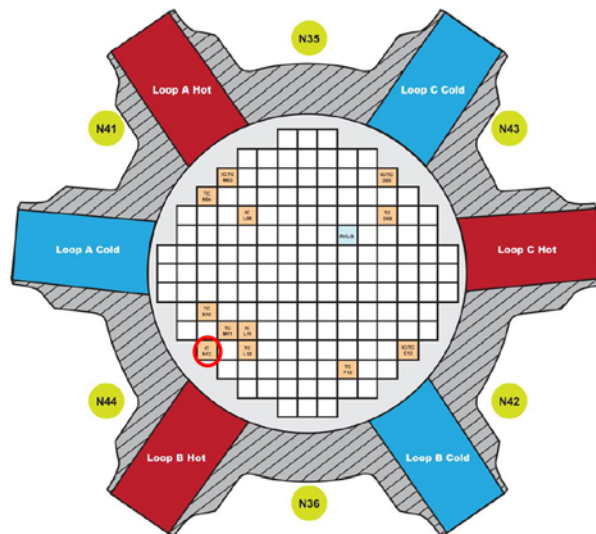
- [ 27 ] Traore, O.I. and Pantera, L. and Favretto-Cristini, N. and Cristini, P. and Viguiere-Pla, S. and Vieu, P.  
Structure analysis and denoising using Singular Spectrum Analysis Application to Acoustic Measurement, vol. 104, pp. 78–88, Jul. 2017
- [ 28 ] Machek J.  
Validation on in-core measurements  
Proceedings of the 22nd International Conference on Nuclear Engineering (ICONE 2014), Prague, Czech Republic, July 7-11, 2014
- [ 29 ] Machek J  
Reconstruction of ex- and in-core neutron signals  
Presentation in CORTEX workshop, Rez, February 22, 2019
- [ 30 ] Leontidis G.  
Deep learning: 3D convolutional and recurrent neural networks in reactor perturbations unfolding and anomaly detection  
Presentation in CORTEX workshop, Rez, February 22, 2019
- [ 31 ] Tambouratzis T.  
General Regression Neural Networks for the Concurrent, Timely and Reliable Identification of Detector Malfunctions and / or Nuclear Reactor Deviations from Steady-State Operation  
IEEE Symposium Series on Computational Intelligence (SSCI 2018), Bangalore, November 2018
- [ 32 ] Herb J.  
WP4 – Application and demonstration of the developed modelling tools and signal processing techniques against plant data WP4 objectives  
Presentation in CORTEX annual meeting, Garching, October 22-25, 2018
- [ 33 ] Lipcsei S., Pohlus J., Paquee U., Giradin G., Riggsbee E.  
Document describing all validation data  
Cortex, D4.3, November 2018
- [ 34 ] Pohlus J., Paquee U., Giradin G.  
Report about the measurement results of Gösgen  
Cortex, D4.1, November 2018
- [ 35 ] Antonios Mylonakis (CHALMERS), Dionysios Chionis (PSI)  
Early generation of simulated data, Cortex, Subtask 3.1.2

## 8 Annexes

### 8.1 Annex A1 – JTFS spectrograms of upper L-G02-1 SPND in Goesgen EOC of U1C39 in the frequency ranges up to 100Hz

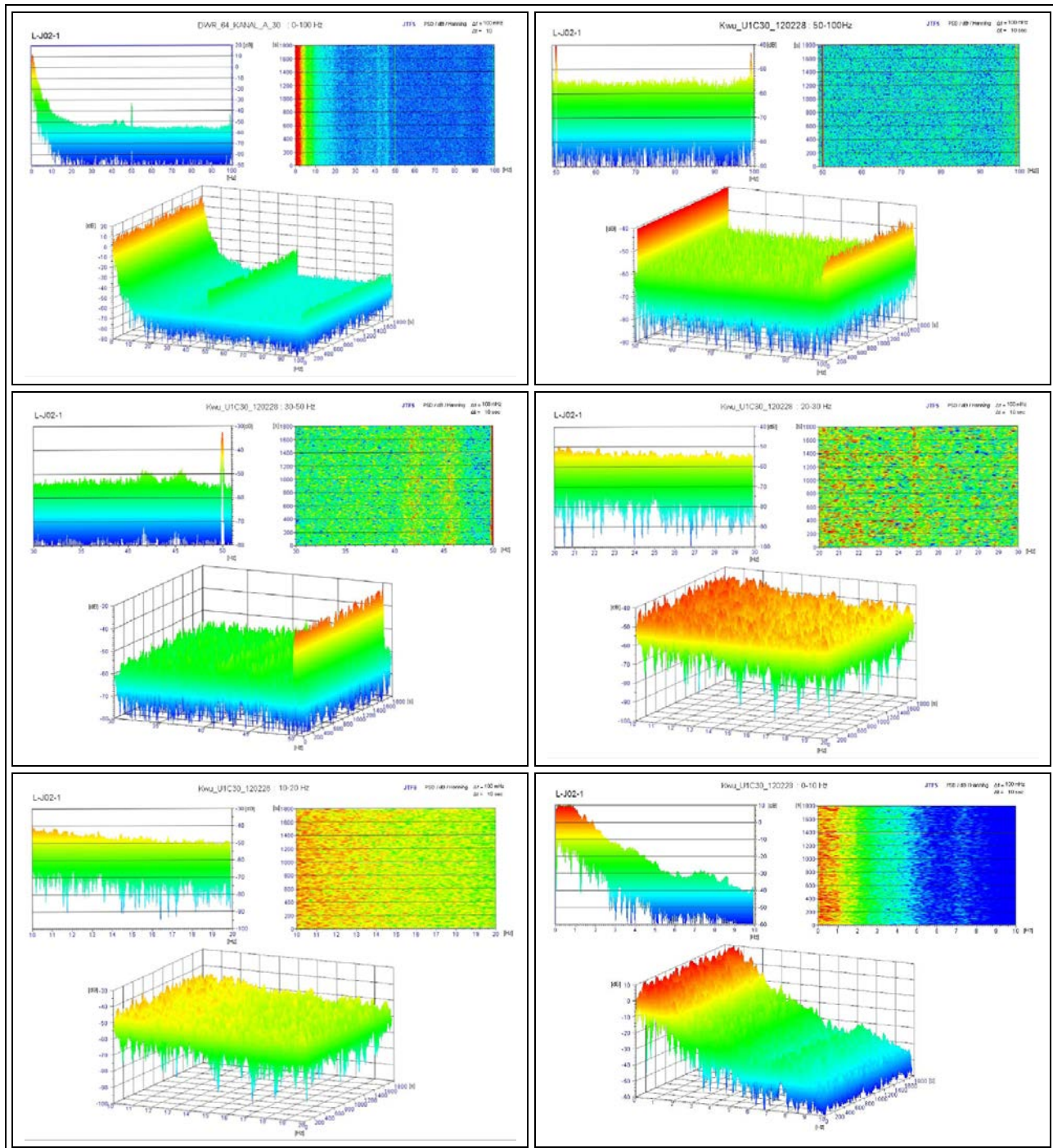
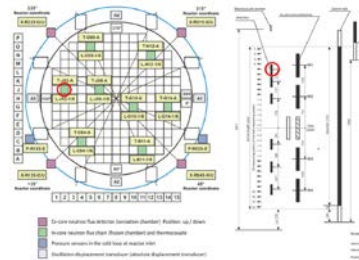


## 8.2 Annex A2 – JTFS spectrograms of lower fission chamber IC-N12-44 in WEC PWR3 in the frequency ranges up to 100Hz

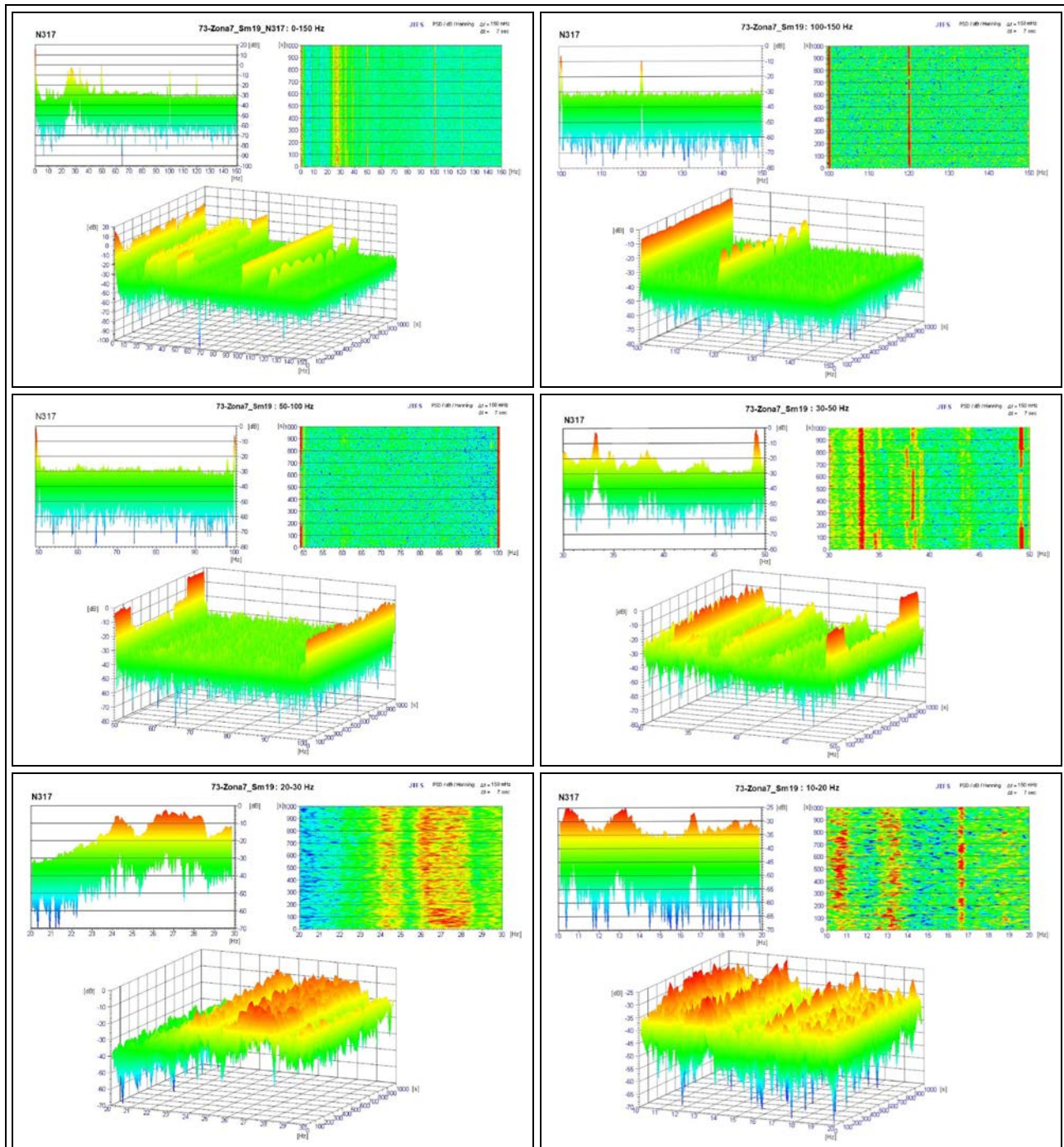
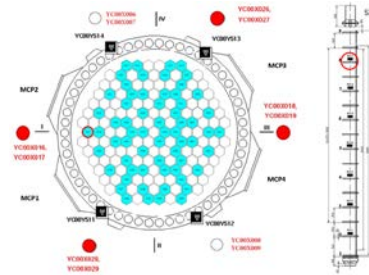




### 8.3 Annex A3 – JTFS spectrograms of upper LJ02-1 SPND of German 4-loop pre-KONVOI reactor in EOC U1C30 in the frequency ranges up to 100Hz

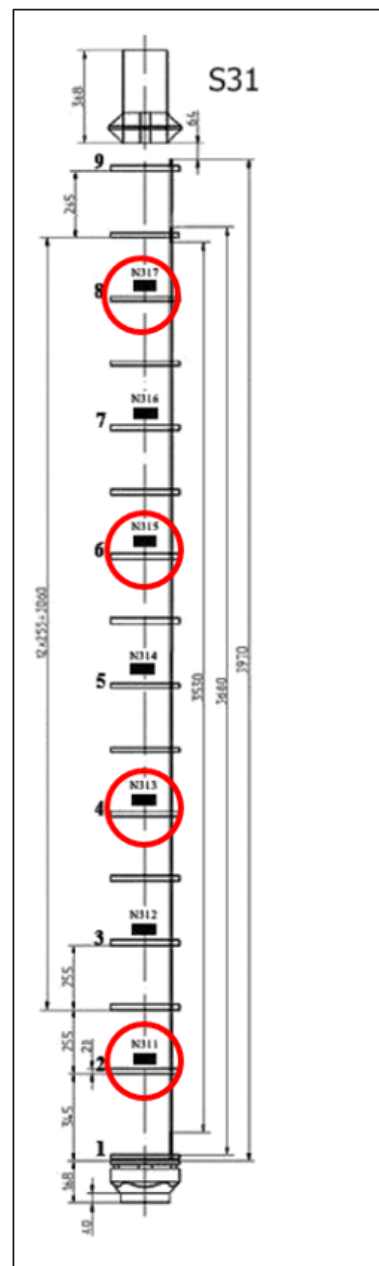
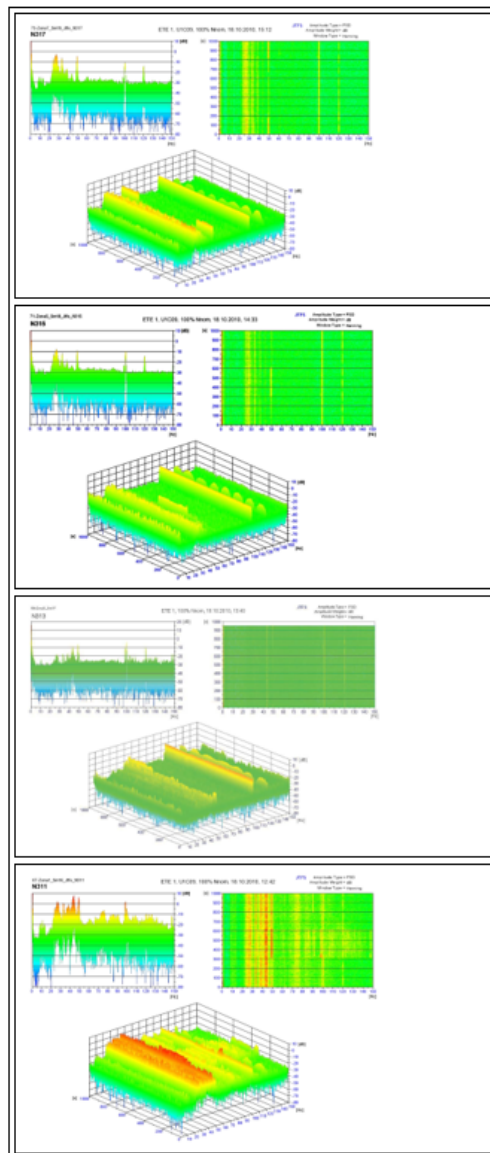
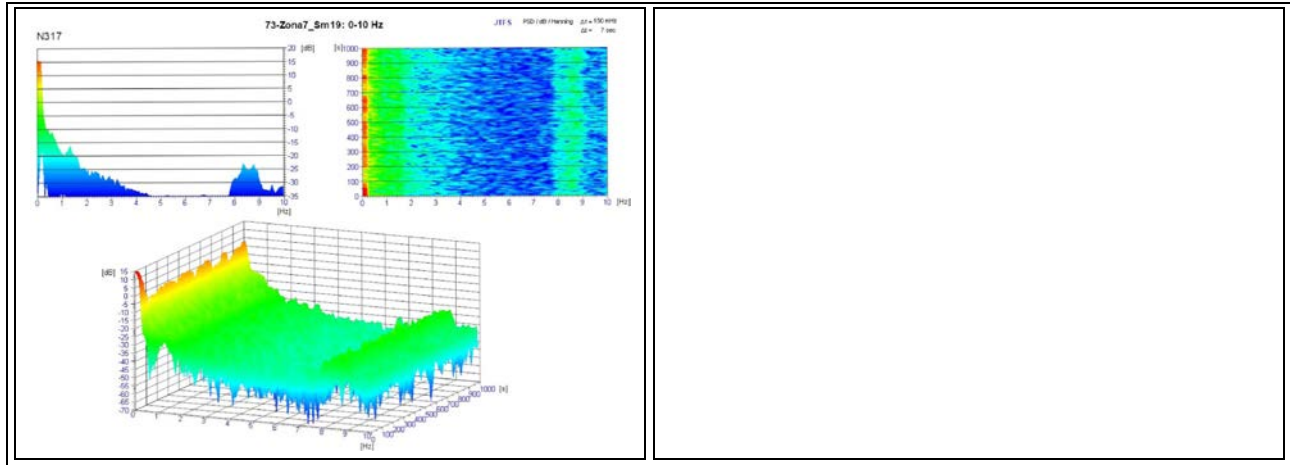


## 8.4 Annex A4 – JTFS spectrograms of upper N317 SPND in the Czech 4 loop VVER 1000 Temelin of BOC U1C09 in the frequency ranges up to 150Hz





### D3.3 Development of advanced signal processing techniques and evaluation results





## 8.5 Annex A5 – Reconstruction of in-core Gösgen EOC39 results - summary

Sensor ID	Mean	StDev	RMS	MaxDev	Signal/Noise	Correl	Comment
L-C08-1	0,038824	0,043210	0,010430	0,049589	4,14	0,9708	
L-C08-2	0,001334	0,049021	0,009918	0,045603	4,94	0,9793	
L-C08-3	-0,006837	0,055553	0,009904	0,042356	5,61	0,9840	
L-C08-4	-0,000096	0,000082	0,000083	-0,000305	0,99	-0,0033	Invalid measurement
L-C08-5	-0,017503	0,073120	0,012589	0,052665	5,81	0,9851	
L-C08-6	0,031639	0,054089	0,010369	0,047884	5,22	0,9815	
L-G02-1	0,011003	0,033570	0,002505	0,015400	13,40	0,9972	
L-G02-2	-0,001716	0,036654	0,002346	0,019221	15,62	0,9979	
L-G02-3	0,013243	0,040908	0,003817	0,018868	10,72	0,9956	
L-G02-4	-0,001321	0,046019	0,005596	0,034667	8,22	0,9926	
L-G02-5	-0,015384	0,042760	0,007011	0,043653	6,10	0,9865	
L-G02-6	-0,001155	0,000252	0,000211	-0,001732	1,20	0,5710	Invalid measurement
L-G10-1	0,030412	0,035158	0,007457	0,039397	4,71	0,9775	
L-G10-2	-0,024682	0,037395	0,008185	0,046040	4,57	0,9761	
L-G10-3	0,000249	0,041947	0,002573	0,014427	16,30	0,9981	
L-G10-4	-0,008605	0,051826	0,004239	0,022027	12,23	0,9966	
L-G10-5	-0,010013	0,041777	0,004512	0,044861	9,26	0,9942	
L-G10-6	-0,015440	0,037082	0,007451	0,084898	4,98	0,9796	
L-J06-1	0,022880	0,049972	0,009941	0,041713	5,03	0,9802	
L-J06-2	0,022391	0,184669	0,176428	2,177315	1,05	0,2957	Partially invalid meas.
L-J06-3	0,038555	0,064139	0,006970	0,034634	9,20	0,9942	
L-J06-4	0,003528	0,075926	0,004127	0,021924	18,40	0,9985	
L-J06-5	-0,005246	0,070841	0,004720	0,024212	15,01	0,9978	
L-J06-6	0,040500	0,056931	0,018556	0,081154	3,07	0,9458	
L-J14-1	0,106445	0,000000	0,009844	0,052912	0,00	0,0000	Constant value!!!
L-J14-2	-0,009104	0,080918	0,010724	0,051971	7,55	0,9912	
L-J14-3	0,060541	0,082520	0,007349	0,036403	11,23	0,9960	
L-J14-4	-0,010087	0,095186	0,008557	0,038794	11,12	0,9960	
L-J14-5	-0,046087	0,110982	0,009496	0,047511	11,69	0,9963	
L-J14-6	0,028233	0,092727	0,013095	0,069341	7,08	0,9900	
L-N08-1	-0,023290	0,039147	0,014197	0,148019	2,76	0,9319	
L-N08-2	0,000300	0,001331	0,001312	-0,014632	1,01	0,1715	Invalid measurement
L-N08-3	-0,021200	0,039458	0,010167	0,092202	3,88	0,9662	
L-N08-4	-0,515178	0,254468	0,279942	3,779640	0,91	0,0385	Invalid measurement
L-N08-5	-0,025816	0,056510	0,020775	0,136239	2,72	0,9305	
L-N08-6	0,039940	0,050442	0,028954	0,356042	1,74	0,8299	

## **8.6 Annex A6 – Reconstruction of ex-core Gösgen EOC39 results – summary**

Explanations to the table heading:

Mean – mean value of the original signal

StDev – standard deviation of the original signal

RMS – residual standard deviation (standard deviation of differences between signal and its reconstruction)

MaxDev – biggest deviation between signal and its reconstruction

Signal/Noise – standard deviation of the signal divided by residual standard deviation

Correl – correlation between signal and its reconstruction

Sensor ID	Mean	StDev	RMS	MaxDev	Signal/Noise	Correl
X-0225-O	0,025165	0,066081	0,012955	0,064461	5,10	0,9806
X-0225-U	-0,045646	0,070577	0,014674	-0,068865	4,81	0,9782
X-1125-O	0,011072	0,054619	0,010384	0,049511	5,26	0,9818
X-1125-U	-0,020701	0,057262	0,011416	-0,051508	5,02	0,9799
X-2025-O	-0,017142	0,057074	0,009922	0,050807	5,75	0,9848
X-2025-U	0,035525	0,058472	0,010499	-0,049280	5,57	0,9838
X-2925-O	-0,030000	0,066364	0,011142	-0,052458	5,96	0,9858
X-2925-U	0,004350	0,069515	0,012384	-0,055331	5,61	0,9840

## 8.7 Annex A7 – Reconstruction of in-core Gösgen BOC40 results – summary

Sensor ID	Mean	StDev	RMS	MaxDev	Signal/Noise	Correl	Comment
L-C08-1	0,002243	0,017214	0,001963	0,010474	8,77	0,9935	
L-C08-2	0,021198	0,022696	0,001967	0,010903	11,54	0,9962	
L-C08-3	-0,004252	0,029027	0,004027	0,021271	7,21	0,9903	
L-C08-4	0,001092	0,000093	0,000109	-0,000623	0,85	0,0395	Invalid measurement
L-C08-5	0,018295	0,040298	0,006553	0,038545	6,15	0,9867	
L-C08-6	-0,007992	0,023651	0,004759	0,024342	4,97	0,9795	
L-G02-1	0,008538	0,014914	0,001416	0,006463	10,53	0,9955	
L-G02-2	0,008337	0,018881	0,001312	0,006187	14,39	0,9976	
L-G02-3	0,013089	0,022408	0,002197	0,010706	10,20	0,9952	
L-G02-4	0,003641	0,024131	0,003357	0,018787	7,19	0,9903	
L-G02-5	-0,014975	0,022427	0,005788	0,029473	3,87	0,9672	
L-G02-6	-0,000206	0,000165	0,000160	0,000765	1,03	0,2689	Invalid measurement
L-G10-1	0,003859	0,017535	0,001293	0,006040	13,56	0,9973	
L-G10-2	0,008132	0,019531	0,001407	0,006478	13,88	0,9974	
L-G10-3	-0,010442	0,020008	0,007445	0,036888	2,69	0,9299	
L-G10-4	0,012702	0,020839	0,003727	0,022983	5,59	0,9839	
L-G10-5	0,004231	0,015580	0,003174	0,025596	4,91	0,9790	
L-G10-6	-0,001629	0,012891	0,008311	0,053294	1,55	0,7644	Problem measurement
L-J06-1	-0,007364	0,025920	0,002293	0,014394	11,30	0,9961	
L-J06-2	0,027294	0,030420	0,003173	0,020411	9,59	0,9946	
L-J06-3	-0,012725	0,032791	0,003610	0,018106	9,08	0,9939	
L-J06-4	0,026379	0,028739	0,001810	0,008982	15,88	0,9980	
L-J06-5	0,012086	0,022778	0,001698	0,009034	13,41	0,9972	
L-J06-6	-0,010769	0,015810	0,003111	0,019895	5,08	0,9805	
L-J14-1	0,019683	0,038691	0,002296	0,011454	16,85	0,9982	
L-J14-2	0,026052	0,055628	0,002198	0,011559	25,31	0,9992	
L-J14-3	-0,010229	0,065516	0,004381	0,024920	14,95	0,9978	
L-J14-4	-0,034411	0,065004	0,004507	0,025651	14,42	0,9976	
L-J14-5	0,004526	0,064612	0,002743	0,015157	23,56	0,9991	
L-J14-6	0,013871	0,049466	0,003491	0,017859	14,17	0,9975	
L-N08-1	-0,010605	0,027566	0,020956	0,110670	1,32	0,6499	Problem measurement
L-N08-2	0,000385	0,001345	0,001338	0,014668	1,01	0,1180	Invalid measurement
L-N08-3	-0,066967	0,088859	0,082654	0,363113	1,08	0,3671	Invalid measurement
L-N08-4	-0,515178	0,254468	0,279942	3,779640	0,91	0,0385	Invalid measurement
L-N08-5	-0,042918	0,039671	0,029138	0,135963	1,36	0,7072	Invalid measurement
L-N08-6	-0,010554	0,021660	0,012345	0,069010	1,75	0,8222	Problem measurement

Measurements L-C08-4, L-G02-6 are not valid measurements.

The whole string L-N08 is very problematic.

## **8.8 Annex A8 – Reconstruction of ex-core Gösgen BOC40 results – summary**

Sensor ID	Mean	StDev	RMS	MaxDev	Signal/Noise	Correl
X-0225-O	-4,025904	0,036855	0,006278	-0,034085	5,87	0,9854
X-0225-U	-4,219134	0,038546	0,006884	0,041199	5,60	0,9841
X-1125-O	-4,091402	0,024704	0,006467	-0,032049	3,82	0,9728
X-1125-U	-4,248989	0,026621	0,007270	-0,033119	3,66	0,9620
X-2025-O	-4,083104	0,028927	0,005757	0,030584	5,02	0,9800
X-2025-U	-4,261501	0,028005	0,005903	-0,029826	4,74	0,9777
X-2925-O	-4,084329	0,041763	0,013535	-0,066113	3,09	0,9496
X-2925-U	-4,239033	0,043013	0,008052	-0,040255	5,34	0,9824

All ex-core measurements are OK.

## 8.9 Annex A9 – Reconstruction of in-core Gösgen MOC40 results – summary

Sensor ID	Mean	StDev	RMS	MaxDev	Signal/Noise	Correl	Comment
L-C08-1	-0,004172	0,020415	0,004419	-0,021382	4,62	0,9763	
L-C08-2	0,002409	0,025990	0,004546	0,026142	5,72	0,9846	
L-C08-3	0,002439	0,031296	0,005494	-0,027138	5,70	0,9845	
L-C08-4	0,000555	0,000069	0,000130	-0,000567	0,53	0,0125	Invalid measurement
L-C08-5	-0,012549	0,037983	0,018021	0,082679	2,11	0,8808	
L-C08-6	0,029368	0,029781	0,015431	-0,081499	1,93	0,8750	
L-G02-1	0,000973	0,016045	0,002550	0,017348	6,29	0,9873	
L-G02-2	-0,001716	0,036654	0,002346	0,019221	15,62	0,9979	
L-G02-3	0,000468	0,022841	0,001717	0,011773	13,30	0,9972	
L-G02-4	0,019369	0,025933	0,002053	-0,018575	12,63	0,9969	
L-G02-5	0,008173	0,024534	0,002787	0,025446	8,80	0,9935	
L-G02-6	-0,000025	0,000188	0,000188	-0,000511	1,00	0,0207	Invalid measurement
L-G10-1	-0,001394	0,017497	0,003963	-0,038662	4,42	0,9740	
L-G10-2	0,019224	0,019310	0,002555	0,025378	7,56	0,9761	
L-G10-3	0,004778	0,021320	0,001512	-0,007239	14,10	0,9975	
L-G10-4	-0,007094	0,024859	0,002529	0,017879	9,83	0,9948	
L-G10-5	-0,001362	0,019528	0,001934	-0,026358	10,10	0,9951	
L-G10-6	-0,011276	0,017541	0,003014	0,045199	5,82	0,9851	
L-J06-1	0,031847	0,034732	0,003973	0,042380	8,74	0,9935	
L-J06-2	-0,002940	0,040031	0,002250	-0,024049	17,79	0,9984	
L-J06-3	-0,020153	0,031292	0,002178	0,023351	14,36	0,9976	
L-J06-4	0,003807	0,033001	0,001864	-0,012818	17,71	0,9984	
L-J06-5	0,006840	0,033056	0,002166	0,012803	15,26	0,9979	
L-J06-6	0,007667	0,026255	0,004128	-0,026993	6,36	0,9876	
L-J14-1	0,009193	0,023630	0,001195	0,006144	19,78	0,9987	
L-J14-2	0,013427	0,032008	0,001107	-0,006070	28,92	0,9994	
L-J14-3	0,003821	0,036725	0,002456	-0,012264	14,95	0,9978	
L-J14-4	-0,004472	0,041291	0,005023	-0,027647	8,22	0,9926	
L-J14-5	-0,000814	0,045878	0,006891	0,033464	6,66	0,9887	
L-J14-6	0,024741	0,037592	0,007904	-0,048770	4,76	0,9780	
L-N08-1	0,000746	0,008311	0,006790	0,136453	1,22	0,7139	Invalid measurement
L-N08-2	-0,000320	0,001454	0,001445	-0,014729	1,01	0,1115	Invalid measurement
L-N08-3	-0,013071	0,010651	0,004918	-0,129445	2,17	0,8870	
L-N08-4	0,036317	0,038605	0,01883	0,419941	2,05	0,8730	
L-N08-5	0,002527	0,010175	0,002670	-0,042959	3,81	0,9650	Invalid measurement
L-N08-6	-0,002430	0,002547	0,001413	-0,015971	1,80	0,8319	Invalid measurement



## **8.10 Annex A10 – Reconstruction of ex-core Gösgen MOC40 results – summary**

Sensor ID	Mean	StDev	RMS	MaxDev	Signal/Noise	Correl
X-0225-O-DC	-3,989482	0,050270	0,008407	-0,048457	5,98	0,9859
X-0225-U-DC	-4,298804	0,055981	0,009952	0,059437	5,63	0,9842
X-1125-O-DC	-4,033873	0,040014	0,008492	-0,043889	4,71	0,9790
X-1125-U-DC	-4,318563	0,043483	0,009541	0,046960	4,56	0,9757
X-2025-O-DC	-4,026101	0,042128	0,007052	-0,035417	5,97	0,9859
X-2025-U-DC	-4,340588	0,044095	0,007868	0,038703	5,60	0,9841
X-2925-O-DC	-4,043029	0,052272	0,009203	-0,044194	5,68	0,9844
X-2925-U-DC	-4,317838	0,056729	0,010759	0,052358	5,27	0,9820

All ex-core measurements are OK.